

The Role of Size Effects on the Thermal Conductivity of Thin Film Alloys and Superlattices

A dissertation

presented to

the faculty of the School of Engineering and Applied Science
University of Virginia

in partial fulfillment

of the requirements for the degree of

Doctor of Philosophy in Mechanical Engineering

by

Ramez Cheaito

© Copyright by Ramez Cheaito 2015
All Rights Reserved

August 2015

Approval Sheet:

The dissertation is submitted in partial fulfillment of the requirements for the degree of Doctor of Philosophy in Mechanical Engineering.

Ramez Cheaito, *Author*

The dissertation has been read and approved by the examining committee:

Prof. Pamela M. Norris, *Chair*

Prof. Patrick E. Hopkins, *Advisor*

Prof. Archie L. Holmes

Prof. Joseph Poon

Prof. Ganesh Balakrishnan

Dr. Bryan Kaehr

Accepted for the School of Engineering and Applied Science

Dean, School of Engineering and Applied Science
August 2015

The Role of Size Effects on the Thermal Conductivity of Thin Film Alloys and Superlattices

by

Ramez Cheaito

Presented to the Faculty of the School of Engineering and Applied Science, University of Virginia, August 2015, in partial fulfillment of the requirements for the degree of Doctor of Philosophy in Mechanical Engineering

Abstract

Advancements in modern technologies have relied primarily on the miniaturization of electronic devices. As the dimensions of these devices are reduced to hundreds of nanometers, thermal management becomes a challenge. Performances are now dependent on the amount of power a device can dissipate before surpassing the temperature set by reliability requirements. Understanding thermal transport in thin film nanostructures is a key element in manufacturing devices with long lifetimes and better energy efficiencies.

The role of size effects on the behavior of heat carriers in thin film structures and across interfaces have been the focus of numerous studies over the past few decades. However, discrepancies among studies on phonon behavior obstruct the understanding of the fundamental processes governing phonon transport. On the other hand, the lack of data on electron thermal transport across interfaces and in periodic structures motivates more research in this direction. This dissertation presents thermal conductivity measurement results on four different material systems of sample thicknesses spanning three orders of magnitude to provide a deep understanding into the processes of phonon and electron thermal transport in thin film alloys and superlattices. Measurements were performed using time-domain thermoreflectance, a non-contact, optical method for the thermal characterization of bulk and thin film materials.

The effect of boundary scattering of long mean free path phonons on the thermal conductivity of thin film SiGe alloys and AlAs-GaAs superlattices is thoroughly discussed in light of the spectral contribution of these phonons to thermal transport. The interplay between short and long range boundary scattering in AlAs-GaAs superlattices is studied by systematically varying the period and film thicknesses. Phonon coherence in epitaxially grown SrTiO₃-CaTiO₃ superlattices is demonstrated by showing a minimum in the thermal conductivity as a function of period thickness. For electrons, the interplay between electron characteristic length and the materials' intrinsic properties is studied via measurements of the thermal interface conductance in Cu-Nb multilayers.

A major result of this dissertation is demonstrating the possibility of achieving a desired thermal conductivity by prescribing both the period and sample thickness of a superlattice, a result that has important implications on thermal management and thermal engineering applications.

Acknowledgements

This dissertation would not have been possible without the help, guidance, and support of a great group of friends, colleagues, and family.

First, I want to express my deepest appreciation to my advisor, Prof. Patrick E. Hopkins. Patrick was not just an advisor, but a friend and a big brother. Without his guidance, none of the work in this dissertation would have been of an impact. Patrick, thank you for making the past four years much easier, more enjoyable, and more productive than I ever imagined. You are my role model and I am proud to be your student.

I am also thankful to the committee members for their guidance and time, Prof. Pamela Norris, Prof. Archie Holmes, Prof. Joseph Poon, Prof. Ganesh Balakrishnan, and Dr. Bryan Kaehr.

I am indebted to Prof. Aaron J. Schmidt, Boston University. Before coming to UVA, Aaron taught me all about TDTR, from basic optics alignment to intricate system troubleshooting. His teaching style contributed to the meticulous experimentalist I am now.

I would also like to thank Dr. John C. Duda, Seagate Technology. John was my first colleague at UVA. He was the first one to teach me about phonons, the diffuse mismatch model, and the principle of detailed balance. Without him, my achievements throughout the past four years would not have been the same.

It might be a stretch but I believe, based upon what I experienced, that a material characterization technique without interesting materials to study might be a useless piece of equipment! Therefore, I am indebted to several colleagues that supplied me with interesting materials to study: samples they spent days and nights fabricating

then trusting that I am the one to measure and study these samples. Without your efforts, I would have had nothing to present in this dissertation. I am grateful to Ajay Kumar Yadav, University of California, Berkeley, and Jayakanth Ravichandran, University of Southern California, for the unprecedented high quality oxide samples they made. I am also thankful to Prof. Ganesh Balakrishnan and his team at the University of New Mexico for the tremendous amount of samples they provided. In particular, I would like to thank Sadhvikas Addamane from the same group for all the superlattices he grew and his prompt replies to my endless questions and emails.

Special thanks goes to Dr. John Gaskins from UVA. John was very patient with me and tolerated all my picky aluminum evaporation and thickness checking requests.

I would also like to thank my colleague Brian Foley. Although I have never mentioned this to him, the small little talks we used to have every now and then on research and science used to give me a relief and made my life easier throughout the first two years at UVA.

A big thank you goes to all the members of the ExSiTE lab. It was a pleasure working with you all.

I would also like to thank my friend and former house mate, Seth Swingle. Seth is the only person I met in the US that knows a big deal about the Middle East. Our discussions were extremely enjoyable and I was in need to such a friend here.

Lastly my family: as much as I want to thank them all, I want to apologize for not being in touch as much as I should have been over the past four years. Mama Najah, Baba Ali, my brother and childhood hero, Bilal, and my two lovely sisters, Jihan and Faten, I love you all and I am eternally indebted to you for making me who I am. I will not miss this chance to acknowledge and welcome my nephew Mohammad (or Hammoudi) to the Cheaito family. One day he will grow up and read these words, he might be inspired to become an engineer, or might be inspired to become something else. Either way, all the luck to you Hammoudi!

Table of Contents

1	Introduction and Background	11
1.1	Size Effects	12
1.2	Applications	15
1.3	Statement of Objectives and Scope of Dissertation	16
2	Theory and Concepts	18
2.1	Phonons	18
2.2	Phonon Dispersion	19
2.2.1	Debye Approximation	20
2.2.2	Density of States	21
2.2.3	Mini-band Formation in Superlattices	21
2.3	Phonon Coherence	23
2.3.1	Definition	23
2.3.2	Minimum in Thermal Conductivity Approach	24
2.3.3	Ballistic Transport Approach	25
2.3.4	Phonon Coherence Length Calculation	26
2.3.5	Effects of Anharmonic Scattering on Phonon Coherence	27
2.3.6	Nature versus Behavior	28
2.4	Phonon Thermal Conductivity	29
2.4.1	Scattering Processes	30
2.5	Thermal Boundary Conductance	33
3	Time-Domain Thermoreflectance (TDTR)	34
3.1	Background	34
3.2	Optical Setup: Double Color and Two-Tint	37
3.3	Heat Transfer Analysis and Lock-in Amplifier Response	40
3.3.1	Thermal Response	41
3.3.2	Photodetector Response	48
3.3.3	Lock-in Amplifier Response	49
3.4	Post Processing	53
3.5	Sensitivity Analysis	54
3.6	Calibration Results and Comparison	54
3.7	Sources of Error	57
3.8	Summary	58

4	Size Effects in Thin Film SiGe Alloys	59
4.1	Background	59
4.2	SiGe Alloy Thin Film Samples	61
4.3	Thermal Conductivity Measurement Results on SiGe Films	62
4.4	Analysis	65
4.4.1	Thermal Model	65
4.4.2	Role of Alloy Composition	66
4.4.3	Spectral Contribution to Thermal Conductivity	67
4.4.4	Temperature Dependence	69
4.5	The Thin Film Alloy Limit	71
4.6	More Recent Studies on SiGe	71
4.7	Summary	72
5	Phonon Coherence in SrTiO₃-CaTiO₃ Superlattices	73
5.1	Background	73
5.2	STO-CTO SLs Samples: Growth and Characterization	75
5.3	Thermal Conductivity Measurements and Sensitivity Analysis	77
5.4	Minimum in Thermal Conductivity	79
5.5	More Recent Studies on Phonon Coherence	83
5.6	Summary	83
6	Size Effects in AlAs-GaAs Superlattices	85
6.1	Background	85
6.2	Sample Growth	88
6.3	Thermal Conductivity Results and Phonon Coherence	90
6.4	Thermal Model: Series Resistor	93
6.5	Spectral Contribution to Thermal Conductivity	95
6.6	Thermal Conductivity Engineering	99
6.7	Disagreement between Model and Data	100
6.8	Summary	101
7	Electron Transport across Metallic Interfaces	103
7.1	Motivation and Background	103
7.2	Copper Niobium Multilayer Samples	105
7.3	Thermal Conductivity and Kapitza Conductance Results	106
7.4	The Electronic Diffuse Mismatch Model (EDMM)	110
7.5	Analysis	111
7.6	Summary	114
8	Summary, Impact, and Future Projects	116
8.1	Summary	117
8.2	Impact	118
8.3	Future Projects	119
	Appendices	120

A Proof of Equation 3.28	121
B Thermal Conductivity of AlAs-GaAs Superlattices	122
B.1 Dispersion Curves for AlAs-GaAs SLs	122
B.2 Thermal Conductivity Calculations	123

List of Figures

1.1	A schematic and TEM image of a superlattice	13
2.1	Dispersion curve for infinite one-dimensional atomic chain	19
2.2	Mini-band formation in superlattice dispersion curves	22
2.3	Phonon coherence, κ_{\min} and κ_{ball} - approaches	25
2.4	Thermal conductivity of materials	29
2.5	Umklapp scattering	31
3.1	TDTR schematic	39
3.2	The pump and the probe pulses	51
3.3	TDTR data and best fit curves on calibration samples	55
4.1	TEM images on SiGe samples	62
4.2	Thermal conductivity of Si-Ge systems versus period and film thicknesses	63
4.3	Thermal conductivity of SiGe alloy thin films versus Ge composition	67
4.4	Spectral thermal conductivity and scattering times for SiGe thin films	68
4.5	Thermal conductivity of Si-Ge systems versus temperature	70
5.1	TEM image of $(\text{SrTiO}_3)_2$ - $(\text{CaTiO}_3)_2$	76
5.2	Sensitivity analysis for SrTiO_3 - CaTiO_3 TDTR measurements	78
5.3	Thermal conductivity of $(\text{SrTiO}_3)_n$ - $(\text{CaTiO}_3)_n$ versus period thickness	80
5.4	Thermal conductivity of $(\text{SrTiO}_3)_n$ - $(\text{CaTiO}_3)_n$ SLs versus temperature	82
6.1	Thermal conductivity of AlAs-GaAs superlattices from literature	87
6.2	AlAs-GaAs superlattices structure	88
6.3	Thermal conductivity of AlAs-GaAs SLs versus film thickness	91
6.4	Kapitza conductance in AlAs-GaAs versus period thickness	94
6.5	Spectral contribution to thermal conductivity of AlAs-GaAs SLs	96
6.6	Thermal conductivity contour plot of AlAs-GaAs SLs	99
7.1	HAADF STEM images of Cu-Nb multilayers	107
7.2	Thermal conductivity versus period thickness of Cu-Nb multilayers	108
7.3	Kapitza conductance versus temperature of metallic interfaces	109
7.4	Electron thermal flux and effective electron mean free path in metals	112
B.1	AlAs-GaAs dispersion curves	123
B.2	First principle calculations of thermal conductivity of AlAs and GaAs	124

List of Tables

2.1	Phonon coherence length of bulk materials	26
3.1	Thermal conductivity of TDTR calibration samples	56
4.1	Thickness and alloy composition of SiGe alloy thin film samples.	61
6.1	Thermal conductivity and structural details of AlAs-GaAs samples	89
6.2	Spectral contribution to thermal conductivity of AlAs-GaAs SL	98
7.1	Structural details of Cu-Nb samples	106
7.2	Parameters used in the calculation of the EDMM	111
7.3	Electron flux and transmission coefficient of metal-metal interfaces	111
B.1	Relaxation time parameters for bulk AlAs and GaAs	125

Chapter 1

Introduction and Background

“What could we do with layered structures with just the right layers? What would the properties of materials be if we could really arrange the atoms the way we want them? They would be very interesting to investigate theoretically. I can’t see exactly what would happen, but I can hardly doubt that when we have some control of the arrangement of things on a small scale we will get an enormously greater range of possible properties that substances can have, and of different things that we can do.”

–Richard Feynman, *Plenty of Room at the Bottom*, 1959

Despite the fact that heat conduction in solids has been the topic of numerous studies in various disciplines, the physics of heat carriers is not completely understood. Fictitious particles, the quanta of heat, and quantized lattice vibrations, all are different phrases that have been used to define phonons: the wave-like quasi-particles responsible for lattice heat conduction in a wide variety of materials. Over the past century, research on phonon properties has dealt with increasingly complex phenomena from long wavelength acoustic excitations [1] to the vibrational spectra in harmonic and anharmonic crystals [2, 3]. Along the way, new characterization methods including neutron [4, 5] and Raman spectroscopy [6], laser thermal excitation techniques [7, 8], and several more were developed to widen our understanding of the underlying physics as well as provoke our curiosity to synthesize and study more intricate structures. With the ongoing advancements in nanostructure fabrication techniques, new

material structures are introduced on a daily basis. In addition to the wide applications of these structures, they provide a means to explore fundamental physics of phonons and electrons and their behavior at interfaces and in different material geometries.

1.1 Size Effects

When the dimensions of a material become comparable to the heat carriers characteristic length, thermal properties become dependent on the dimension in what is usually referred to as *size effects*. Size effects affecting phonon transport in solids were first observed by de Haas and Biermasz in 1935 [9]. They found that at very low temperatures, the thermal conductivities of bulk quartz [9], KCl, and KBr [10] reach a maximum (now referred to as the Umklapp peak) around 10 K to decrease back with the decrease in temperature, contrary to the theories present at that time. Three years later, Casimir [11] demonstrated that this result¹ was due to elastic waves reflecting from the sample boundaries where their free path compares to the sample dimensions at very low temperatures. The term Casimir limit was then used to describe size effects in nanostructures and bulk materials. In nanostructures, size effects can be observed at room temperature and lead to a significant deviation from bulk thermal conductivity values [12].

The idea of boundary scattering at the material boundary or a solid-solid interface has been employed in nanofabrication to study the behavior of heat carriers at interfaces and engineer materials with specific physical properties. One such nanoscale heterostructure that relies on large volumetric density of material interfaces is a superlattice. Superlattices (SLs) are periodic structures of two or more alternating

¹In fact, de Haas and Biermasz mentioned in their 1937 paper [10] on thermal conductivity of KBr and KCl that Rudolf Peierls, a German physicist, explained in a letter to them that the observed trend in thermal resistance is a result of elastic waves reflecting from the sample boundaries. Casimir [11] used this explanation a year later to quantify the results.

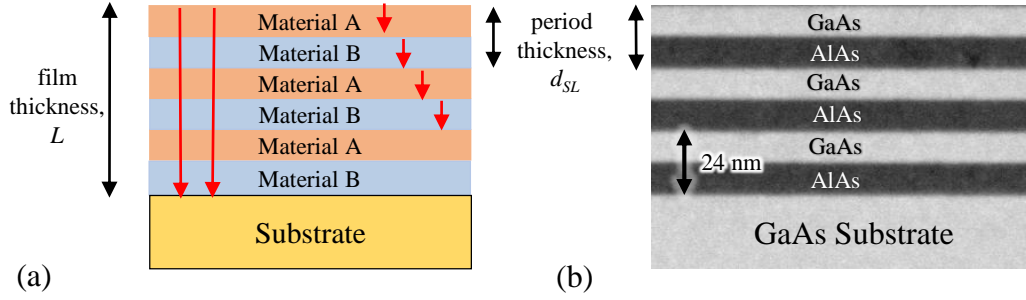


Figure 1.1: (a) A schematic representation of a superlattice showing the two length scales affecting phonon transport. (b) TEM image of AlAs-GaAs superlattice of 24 nm period thickness.

materials. They represent a group of metamaterials that has attracted considerable attention over the past few decades due to their promise as material solutions in thermoelectric devices [13–16] and applications in quantum cascade [17], vertical cavity surface emitting lasers [18], and phase change memory devices [19]. The large interface density in these structures adds an additional source for scattering of heat carriers and results in a reduction in thermal conductivity compared to that of the constituent materials. Figure 1.1 shows a schematic representation of the two length scales dominating phonon scattering in SLs along with a TEM image on AlAs-GaAs SL.

In the simple formulation of the Kinetic Theory of Gases, the thermal conductivity can be written as:

$$\kappa = \frac{1}{3}Cv\ell = \frac{1}{3}Cv^2\tau, \quad (1.1)$$

where C is the specific heat at constant volume, v is the phonon group velocity, ℓ is the mean free path, and τ is the phonon relaxation time. In superlattices with period spacing less than typical intrinsic phonon-phonon mean free paths, two length scales dictate the thermal conductivity: long range boundary scattering where phonons with mean free paths of the order of the superlattice thickness, L , scatter at the sample boundary and short range boundary scattering where phonons with mean free paths

of the order of the superlattice period thickness, d_{SL} , scatter within the superlattice internal interfaces. The interplay between these two scattering mechanisms is not fully understood [20]. However, phonons can also act as waves and traverse a SL without “*feeling*” the interfaces [21, 22]. The spectral nature of phonons and the complexity governing their properties in superlattices require systematic studies on various material systems that can isolate the different contributions to the thermal conductivity in order to better understand the behavior of phonons at interfaces.

In addition to SLs, bulk alloys of materials also exhibit a reduction in thermal conductivity well below that of their homogeneous counterparts [23, 24]. Even at low alloy concentrations, scattering of phonons at alloy sites can dominate thermal transport. Size effects in thin film alloys have not been well studied in literature [20]. This is mainly due to the assumption that alloy scattering impedes thermal transport more so than any scattering of phonons at interfaces.

Where the above-discussed physics of phonon transport typically applies to non-metals, electrons are known to be the dominant heat carriers in metallic systems. While phonons are characterized by a spectrum of mean free paths, electrons are usually treated as non-spectral with a single mean free path at the Fermi energy being sufficient to describe the entire electron population that participates in thermal transport. With this fundamental difference, one would expect that thermal transport of electrons at interfaces significantly differs from phonons. However, the behavior of electrons at interfaces has not received as much of an attention as compared to phonons. Metallic multilayers, analogous to semiconductor superlattices, represent an ideal system to study the role of size effects on electron transport in nanostructures.

This dissertation is focused on thermal transport in thin film alloys, superlattices, and metallic multilayers. The main concern is the effect of materials’ dimensions on the thermal properties of these structures. The thermal properties of the considered materials are crucial for a wide array of technologies. The following section will

address two of the applications in which understanding nanoscale thermal transport plays a vital role in manufacturing devices with high performances.

1.2 Applications

Phase Change Memory Devices

Phase change memory (PCM) devices are considered as the next generation of non-volatile memory with promising higher memory capacity and integration density than dynamic random-access memory (DRAM) [25, 26]. One of the obstacles for PCM is to reduce the programming current to improve various features of the device [19]. Thin film alloys and superlattices have been introduced into the design of different types of phase change memories [19, 27]. The low thermal conductivities of these structures reduce the power consumption in the device leading to higher switching speeds and improved stability. Superlattices of GeTe-Sb₂Te integrated into the recording layer of phase change random access memory have demonstrated superior performance as compared to single layer materials [19]. The ability to engineer the thermal properties of SLs by varying the interface density or by changing the alloy compositions allows for maintaining the device features necessary for non-volatile data storage mechanisms as the device is scaled.

Quantum Cascade Lasers (QCL)

Quantum cascade lasers are semiconductor laser cavities in which electrons transition within and tunnel between cascades of quantum wells, emitting radiation in the mid-to far-infrared spectrum. The active region of a QCL is usually several micrometers in thickness with thousands of very thin semiconductor superlattice layers comprised of various alloys (e.g., GaAs-AlGaAs, GaInAs-AlGaAsSb) [28]. Power densities in the active region can reach extremely high values [17]. Such high power densities along

with the thermal boundary resistances from the thousands of interfaces comprising the active region make heat dissipation a challenge [29, 30]. Knowledge of the thermal properties of materials comprising the active region is a key element to improve performance and extend lifetimes of these devices.

1.3 Statement of Objectives and Scope of Dissertation

The major objective of this work is to develop a fundamental understanding of the mechanisms governing phonon and electron transport at materials' boundaries and across interfaces. The dissertation shall rectify some of the concepts in literature and provide the field with conclusive studies that touch on several aspects of the topic of size effects for nanoscale heat transfer. Although this work is limited to two material structures (thin film alloys and superlattices or multilayers), the results of are a characteristic of the heat carriers that exist in any material system. This being said, these results can explain and aid in understanding heat transfer phenomena in other material systems and geometries (nanowires [31], nanograins [32], etc.). The remainder of this dissertation is organized as follows:

- *Chapter 2* The basic concepts used throughout the dissertation are defined. Definitions of phonons and their behavior as particles or waves are briefly reviewed. The thermal conductivity model used to explain results in parts of this dissertation is also presented. A major part of this chapter is devoted to the topic of phonon coherence and the two main approaches for demonstrating phonon coherence in literature.
- *Chapter 3* All the thermal measurements in this work were performed using time-domain thermoreflectance (TDTR), an optical method well suited for thermal measurements on thin films and nanostructures. The main components of the double color and two-tint TDTR apparatuses are discussed. A detailed

derivation of the thermal model used in analyzing TDTR data and the lock-in amplifier response are given.

- *Chapter 4* In this chapter, size effects in SiGe thin film alloys are discussed. Results introduced in this chapter demonstrate that long range boundary scattering dictates the thermal conductivity in thin film alloy structures and should be accounted for in superlattices as well.
- *Chapter 5* Phonon coherence in strontium titanate-calcium titanate (STO-CTO) superlattices is demonstrated. The role of periodicity in superlattices is discussed in the light of the observed cross over between the particle-like and wave-like behaviors of phonons.
- *Chapter 6* The interplay between periodicity and film thickness is studied using thermal conductivity measurements on AlAs-GaAs superlattices. The results will lead to the reinterpretation of the concept of phonon coherence. In this chapter, a method to tailor the thermal conductivity using a combination of period and film thickness is presented.
- *Chapter 7* Size effects in metallic multilayers are studied. Results from thermal measurements on Cu-Nb multilayers are compared to other metallic systems to understand the effect of material properties and electron mean free path on electronic thermal transport across interfaces.
- *Chapter 8* The major points of this dissertation are summarized and the impact of these original findings is discussed in the context of the fundamental physics of heat carriers and application areas given above. Several potential projects and extensions are proposed.

Chapter 2

Theory and Concepts

“The existing scientific concepts cover always only a very limited part of reality, and the other part that has not yet been understood is infinite. Whenever we proceed from the known into the unknown we may hope to understand, but we may have to learn at the same time a new meaning of the word “understanding”.”

–Werner Heisenberg

In this chapter, I outline some of the theories and concepts used in the analysis of the thermal transport results obtained throughout this dissertation.

2.1 Phonons

In periodic crystals, the oscillations of atoms around their equilibrium positions at a certain frequency give rise to elastic waves that propagate across the material. In the classical description, phonons are the normal modes of these atomic oscillations, where they exist as wavepackets or superpositions of different vibrational frequencies that carry energy across the lattice.

In the quantum mechanical description, phonons represent excited states of the quantized lattice vibrations with a minimum energy of $\hbar\omega$, where ω is the phonon frequency and \hbar is Plank’s constant. In other words, they are particles that carry the

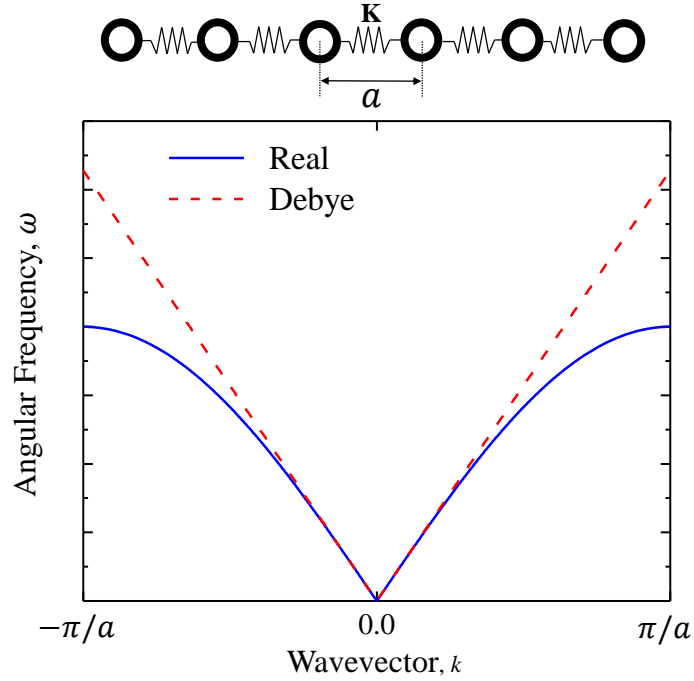


Figure 2.1: (solid line): the real dispersion curve for an infinite one-dimensional atomic chain given by Eq. 2.2. (dashed line): the Debye approximation of the phonon dispersion for infinite one-dimensional atomic chain given by Eq. 2.3. These calculations were obtained using $m = 1$, $K = 1$, and $a = 1$.

vibrational energy of oscillating atoms.

Given these two descriptions, phonons are often denoted as the quanta of lattice vibrations or quasi-particles that display particle and wave behaviors.

2.2 Phonon Dispersion

The phonon dispersion curve relates the phonon frequency to the phonon wavevector.

The slope of the dispersion curve gives the phonon group velocity:

$$v_j = \frac{\partial \omega_j}{\partial k} \quad (2.1)$$

where $k = 2\pi/\lambda$ is the wavevector, λ is the phonon wavelength, and j is the phonon branch. The group velocity represents the speed at which a wavepacket of phonons

propagate. In a certain material, different phonon branches may exist. These branches are often denoted according to their nature and frequencies (acoustic and optical), and the direction of atomic oscillations relative to the direction of propagation of elastic waves (longitudinal and transverse).

A straightforward example that can illustrate the phonon dispersion curve is the infinite one-dimensional atomic chain problem, a problem well detailed in any solid-state physics textbook [33]. In this example, atoms in the lattice are modeled as a spring-mass system where the interaction between nearest neighbors is governed by Hooke's Law ($F = -Kx$). This is depicted schematically in Fig. 2.1. The displacement of the atoms is obtained by solving the equations of motion. The solution is a wave-like ($\exp[kax - \omega t]$) that leads to a dispersion relation relating k and ω :

$$\omega = 2\sqrt{\frac{K}{m}} \sin\left(\frac{kx}{a}\right) \quad (2.2)$$

where x is the atomic displacement, a is the lattice constant, K is the spring constant,¹ and m is the atomic mass. Equation 2.2 is plotted in Fig. 2.1 over the 1st Brillouin zone.

2.2.1 Debye Approximation

In many thermal transport studies, a Debye approximation is made to simplify the analysis. This approximation assumes the phonon modes to be non-dispersive. In this case, the phonon dispersion relation for the one-dimensional monatomic chain becomes:

$$v = \frac{\omega_c}{k_c} = \frac{\omega_c}{(\pi/a)} \quad (2.3)$$

¹Don't confuse κ , the thermal conductivity, with K , the spring constant, and k , the phonon wavevector.

where k_c is the maximum phonon wavevector and ω_c is the phonon cutoff frequency. The Debye dispersion for the one-dimensional atomic chain is plotted in Fig. 2.1. Clearly, the Debye dispersion agrees well with the real dispersion in the zone center and is hence suitable in situations where heat transport is dominated by low frequency phonons.

2.2.2 Density of States

The density of states is defined as the number of energy states per unit space per unit energy interval. It represents the number of energy states ready for occupation inside a solid. From the theory of solids [33], we shall use the following form of the density of states for an isotropic solid:

$$D_j(\omega) = \frac{\omega^2}{2\pi^2 v_j^3(\omega)} \quad (2.4)$$

2.2.3 Mini-band Formation in Superlattices

The infinite atomic chain example can also be used to express dispersion curves in SLs. The mass difference between the atoms of the two different materials forming a SL prohibits some of the vibration modes. This leads to the formation of bandgaps that appear in the phonon dispersion curve. The infinite one dimensional diatomic chain [33] can hence simulate a SL formed of two materials with one atom of each material in the SL unit cell (1×1 SL). The increase in the number of atoms in a SL unit cell increases the number of mini-bands of prohibited phonon modes in the dispersion curve. This results in a reduction in the overall phonon group velocity.

To illustrate this phenomenon, I use a toy model following the work by Simkin and Mahan [34] and plot the dispersion curves for 2×2 , 4×4 , 8×8 , and 12×12 infinite atomic chains made up of two materials A and B of different atomic masses. These $n \times n$ atomic chains can capture the change in the vibrational spectra of phonons

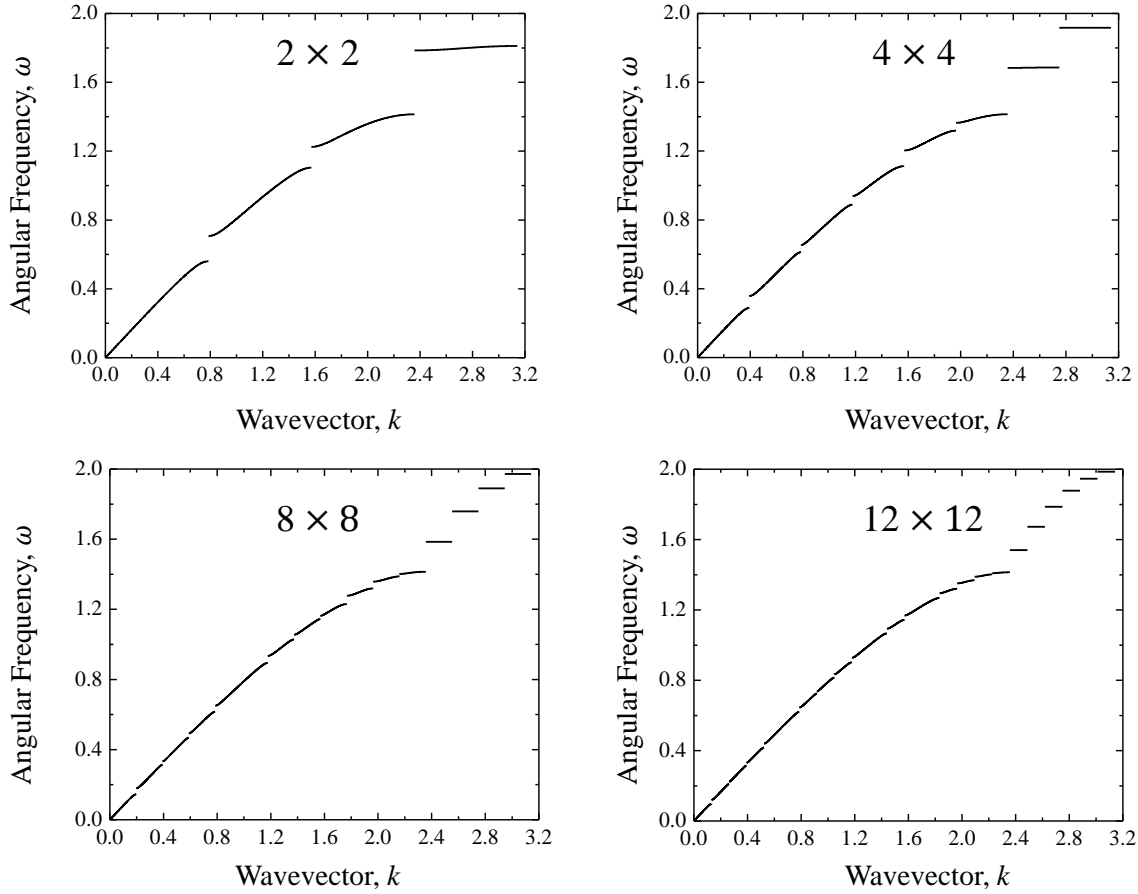


Figure 2.2: The dispersion curves in SLs with different number of atoms in a unit cell. The plots were obtained by lattice dynamics calculations following the work by Simkin and Mahan [34] and are shown in the extended zone scheme. These calculations were obtained using $m_A = 1$, $m_B = 2$, $a = 1$, $K = 1$.

in SLs. In this case, $2n$ is the period thickness. Figure 2.2 shows an increase in the number of mini-bands with the increase in period thickness. The size of the badgaps are appreciable for $n = 2$ and $n = 4$. From $n = 8$ to $n = 12$, the number of minibands continues to increase, however, the sizes of the introduced minibands become infinitesimally small. As a result, we expect the reduction in the phonon group velocity to be more prominent at short period thicknesses.

2.3 Phonon Coherence

A major part of this dissertation (Chapters 5 and 6) is devoted to the topic of phonon coherence. Thermal transport studies on SLs have shown the existence of coherent wave effects. The behavior of phonons was interpreted in the light of the observed coherent or incoherent transport phenomena. Two *different* methods for demonstrating phonon coherence, supported by experimental measurements, have recently been reported in the literature [21, 22]. These approaches are schematically depicted in Fig. 2.3(b) and c. In this section we shall define phonon coherence and describe how each approach demonstrates the existence of phonon coherence through thermal measurements on SLs.

2.3.1 Definition

The word coherent or coherence is usually used to describe waves with a constant phase difference. The wave nature of phonons exhibits itself as wavepackets that spatially extend in a material where atoms within this wavepacket vibrate in phase with each other. The distance over which these waves extend is called the coherence length, l_c (see Fig. 2.3(a)). These wavepackets propagate a certain distance before they scatter, losing their phase somewhere within the material or at the boundaries in case of a diffuse interface. The average distance covered by these phonons before scattering is the mean free path, ℓ . The average time between successive scattering events is the relaxation time, τ . The mean free path and relaxation time are related via the phonon group velocity, where for a phonon with angular frequency ω in a branch j , $\ell_j(\omega) = v_j(\omega) \tau_j(\omega)$.

When the phonon coherence length is larger than one of the material's characteristic lengths, phonons will behave as waves over that characteristic length. In this case, phonon wavepackets are described by the phonon dispersion curve. If the phonon

coherence length is small compared to the dimensions of the material, phonons can be treated as point-wise particles and wave effects can be neglected when modeling thermal transport [35].

2.3.2 Minimum in Thermal Conductivity Approach

For SLs, if the phonon coherence length is larger than the period thickness, coherent phonons will traverse the SL without scattering at the internal interfaces. They “see” the SL as a new homogeneous material. The coherence length is often of the order of a few nanometers [21] (see Section 2.3.4). It is generally not easy to detect these coherent phonons in thermal measurements [21].

If phonons are acting like coherent waves, (i.e., described by the dispersion curve) we would expect a reduction in the thermal conductivity of a SL with the increase in the period thickness caused by the reduction in the overall phonon group velocity due to mini-band formation (recall: $\kappa = Cv\ell/3$).

On the other hand, when phonons act as particles or if the phonon coherence length is smaller than the SL period thickness, phonons will scatter at the SL interfaces, and the thermal conductivity will increase with the increase in period thickness (decrease in the number of interfaces). The increase in thermal conductivity is a result of the increase in the relaxation time as phonons encounter less interfaces and scatter less frequently from boundaries inside the superlattice.

A minimum in thermal conductivity of SLs as a function of period thickness has been theoretically proposed as indicative of a crossover from coherent (wave-like) behavior of phonons at short period thicknesses to incoherent (particle-like) behavior at larger period thicknesses [21, 34, 36–43]. This minimum is schematically represented in Fig. 2.3(b). I denote this approach with the minimum in thermal conductivity approach (κ_{\min} -approach).

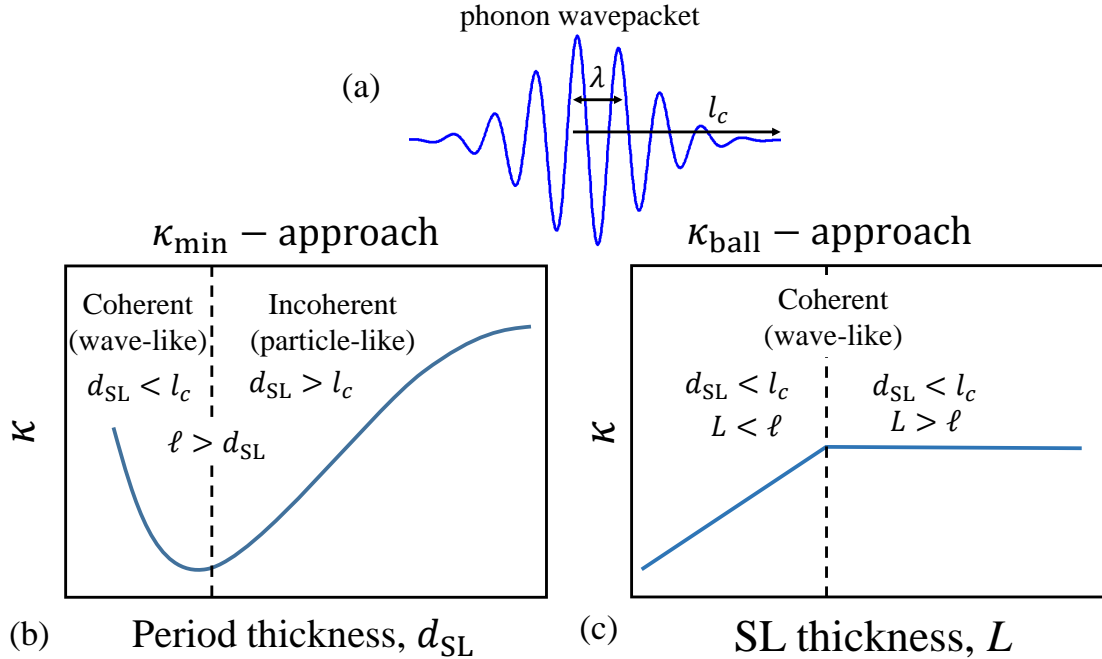


Figure 2.3: Schematic representations of (a) phonon wavepacket, (b) minimum in thermal conductivity approach (κ_{\min} -approach), and (c) ballistic transport approach (κ_{ball} -approach) for demonstrating phonon coherence.

2.3.3 Ballistic Transport Approach

In a recent *Science* paper, Luckyanova *et al.* [22] showed a linear dependence of the thermal conductivity of AlAs-GaAs SLs on the SL thickness where samples had the same period thickness. The linear trend was explained in terms of phonon waves ballistically propagating through the SL film without “feeling” the internal interfaces. They preserve their phase information at the internal interfaces and scatter at the film-substrate interface demonstrating phonon coherence. I denote this approach with the “ballistic thermal conductivity approach” (κ_{ball} -approach). Latour *et al.* [42] predicted that in this approach, the thermal conductivity would plateau once L exceeds ℓ and phonon waves scatter within the SL film instead of the film-substrate interface. This approach is schematically represented in Fig. 2.3(c).

Table 2.1: Phonon coherence length for bulk Si, GaAs, and SrTiO₃ in the longitudinal and transverse acoustic branches (LA and TA).

	Si	Ge	GaAs	AlAs	SrTiO ₃
$v_{\text{LA}} (\times 10^3 \text{ m s}^{-1})$	8.19	5.34	4.81	5.18	7.87
$v_{\text{TA}} (\times 10^3 \text{ m s}^{-1})$	5.51	4.16	3.59	3.15	4.91
$\Delta\nu_{\text{LA}} (\text{THz})$	11.9	6.9	6.7	6.15	4.29
$\Delta\nu_{\text{TA}} (\text{THz})$	4.61	2.5	2.34	3.99	3.39
$l_{c,\text{LA}} (\text{nm})$	0.69	0.77	0.72	0.84	1.83
$l_{c,\text{TA}} (\text{nm})$	1.20	1.66	1.53	0.79	1.45

2.3.4 Phonon Coherence Length Calculation

The phonon coherence length can be estimated similar to that of photons. In this case, $l_c \sim v/\Delta\nu$ where $\Delta\nu$ is the bandwidth of phonon frequencies taken from the dispersion curve. Table 2.1 lists the phonon coherence length for five materials that will be studied in the next chapters. The numbers were calculated using the zone center longitudinal and transverse acoustic group velocity and the corresponding phonon bandwidth of each branch. Values show that SrTiO₃ has a higher coherence length than that of other materials typically used for SLs. As a result, it is more likely to detect coherent wave effects in SL structures where SrTiO₃ is one of the components than it is for SLs with materials like Si, Ge, GaAs, or AlAs.

Note that the numbers given in Table 2.1 are rough estimates to show how the coherence length compares for different materials. A more rigorous formulation to estimate the phonon coherence length was derived by Chen [44] where he extended the work by Mehta [45] for the coherence time of a blackbody radiation to phonons. Since phonons and photons obey the same statistics, the phonon coherence length can be derived similar to photons. The coherence length of a phonon with frequency ω in branch j at a temperature T is given by [44]:

$$l_{c,j}(\omega, T) = v_j(\omega) \tau_{c,j}(T) \quad (2.5)$$

where $\tau_{c,j}$ is the phonon coherence time given by [44]:

$$\tau_{c,j}(T) = \int_0^{\omega_{c,j}} |g_j(\omega, T)|^2 d\omega \quad (2.6)$$

where $g_j(\omega, T)$ is the phonon spectral density defined for $0 < \omega < \omega_{c,j}$ and is proportional to $\hbar\omega D_j(\omega) f(\omega, T)$, where D_j is the phonon density of states and f is the Bose-Einstein distribution. Using Eq. 2.4 for D_j and the expression for Bose-Einstein distribution we get:

$$g_j(\omega, T) = N_j \frac{\omega^3}{v_j^3(\omega) \left[\exp\left(\frac{\hbar\omega}{\kappa_B T}\right) - 1 \right]} \quad (2.7)$$

where the constants were absorbed into the normalization constant N_j which is given by:

$$N_j = \int_0^{\omega_{c,j}} g_j(\omega, T) d\omega = 1 \quad (2.8)$$

Chen [44] used this formulation and found that the phonon coherence length in GaAs is 1 - 2 nm. Given this short coherence length, he demonstrated that a particle treatment using Boltzmann Transport Equation is suitable for modeling thermal transport in AlAs-GaAs SLs.

2.3.5 Effects of Anharmonic Scattering on Phonon Coherence

When a phonon scatters anharmonically it loses its phase information. Therefore, anharmonic scattering of phonons can lead to decoherence effects. The less dominant such processes are, the more likely it is to detect coherent wave effects through thermal measurements. In thermal transport, the maximum in thermal conductivity over temperature, often termed as the ‘‘Umklapp peak’’, occurs when anharmonic scattering becomes a dominant scattering process (Umklapp processes (see Section 2.4.1)). The higher the temperature at which this maximum occurs, the less dominant the

anharmonic effects are and the more favorable the material is for studying coherent wave effects. Figure 2.4 shows the thermal conductivity versus temperature for Si, Ge, GaAs, and SrTiO₃. The Umklapp peak for SrTiO₃ happens at ~ 100 K whereas that for Si, Ge, and GaAs takes place at temperatures less than 30 K. This result, along with larger coherence length of SrTiO₃ demonstrates that SrTiO₃ based SLs exhibit a higher potential in showing coherent wave effects.

In Chapter 5, I experimentally demonstrate phonon coherence according to the κ_{\min} -approach in epitaxially grown SrTiO₃-CaTiO₃ SLs. In Chapter 6, I show that the two approaches (κ_{\min} and κ_{ball}) are describing two fundamentally different physical phenomena and transport in AlAs-GaAs SLS is incoherent, contrary to the findings by Luckyanova *et al.* [22].

2.3.6 Nature versus Behavior

It is important to note that the two discussed approaches describe the behavior and not the nature of phonons. The nature of phonons was discussed in Section 2.1 and is not altered by the behavior of phonons observed via thermal measurements. For example, the wave-like behavior of phonons in the coherent regime of the κ_{\min} -approach does not imply that phonons no longer carry discrete energies as per the particle description. Similarly, the particle-like behavior of phonons in the incoherent regime of the κ_{\min} -approach does not imply that phonons no longer possess a wave nature; they are still defined as atomic vibrations that give rise to elastic waves that carry energy across the lattice. The term “behavior” describes the relation of phonons among themselves (vibrating in- or out-of-phase within a wavepacket) and their relation with the geometry of the material they exist in (the spatial extent of wavepackets given by the coherence length and how it compares to the period thickness).

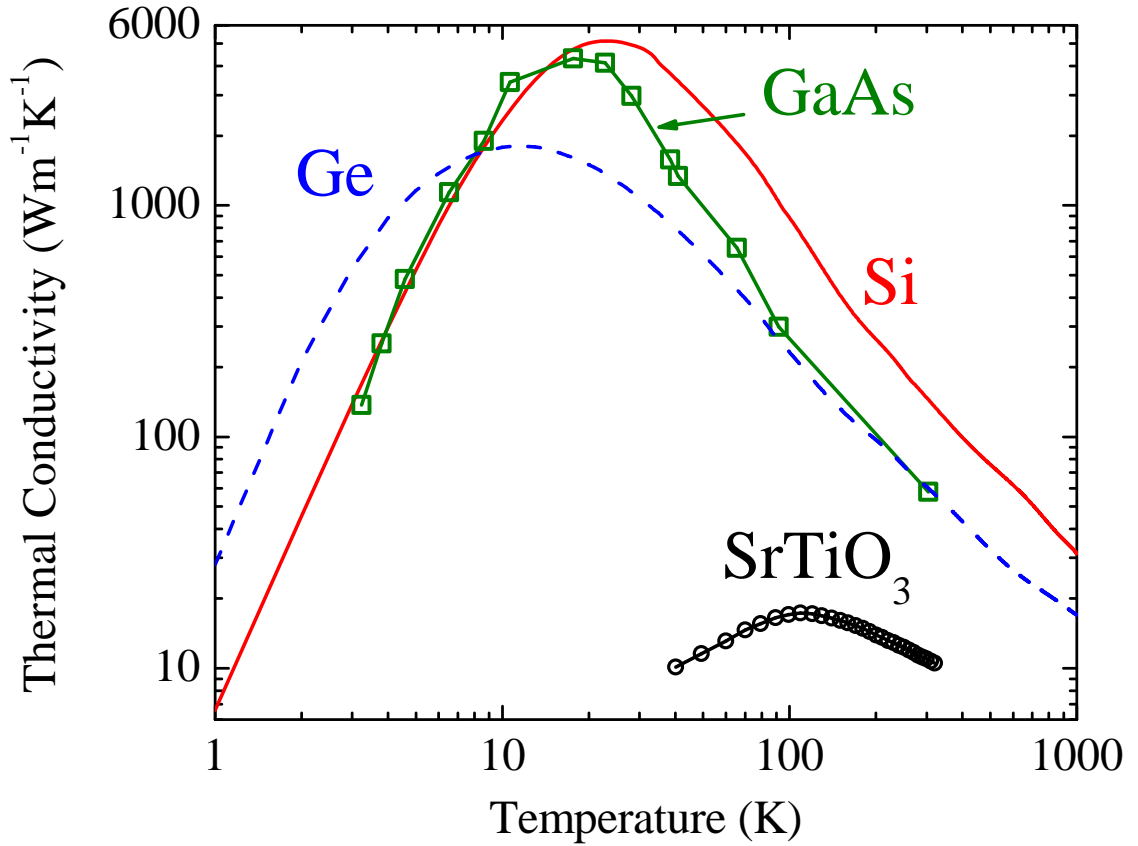


Figure 2.4: Thermal conductivity of Si [46], Ge [46], GaAs [47], SrTiO₃ [48] plotted as a function of temperature.

2.4 Phonon Thermal Conductivity

In a crystalline material, heat carriers (phonons or electrons) can be treated as gases given the fact that their volume is much smaller than the volume of the container (material) they exist in. The thermal conductivity can then be described via the Kinetic Theory of Gases (Eq 1.1). A more detailed expression can be obtained by substituting the heat capacity from the theory of solids [33] into Eq. 1.1. For a homogeneous material of thickness L , the phonon thermal conductivity accounting

for contributions from all phonon branches can be written as [31]:

$$\kappa(L, T) = \frac{1}{3} \sum_j \int_0^{\omega_{c,j}} \hbar \omega D_j(\omega) \frac{\partial f}{\partial T} v_j^2(\omega) \tau_j(\omega, L, T) d\omega \quad (2.9)$$

where j is the phonon branch, T is the temperature, ω is the angular frequency, \hbar is Plank's constant, $v_j(\omega)$ is the phonon's group velocity, $D_j(\omega)$ is the density of states, f is the Bose-Einstein distribution, $\omega_{c,j}$ is the cutoff frequency, and τ_j is the total relaxation time and is related to the relaxation times of the individual scattering processes via Matthiessens rule [33]:

$$\tau_j^{-1} = \sum_i \tau_{i,j}^{-1} \quad (2.10)$$

where i is an index representing a specific scattering process in branch j .

2.4.1 Scattering Processes

In this sub section we briefly mention the scattering processes that affect thermal transport and are used in modeling thermal conductivity in Chapters 4 and 6.

Umklapp Scattering

Umklapp scattering is a multiphonon scattering process in which two phonons with wavevectors \vec{k}_1 and \vec{k}_2 and frequencies ω_1 and ω_2 scatter to produce a phonon with wavevector \vec{k}_3 and frequency ω_3 or a phonon with wavevector \vec{k}_3 and frequency ω_3 scatter to form two other phonons of wavevectors \vec{k}_1 and \vec{k}_2 and frequencies ω_1 and ω_2 , where the resultant phonon(s) fall(s) outside the first Brillouin zone. This is schematically represented in Fig. 2.5. The conservation of energy and momentum give:

$$\vec{k}_1 + \vec{k}_2 = \vec{k}_3 + \vec{G} \quad (2.11)$$

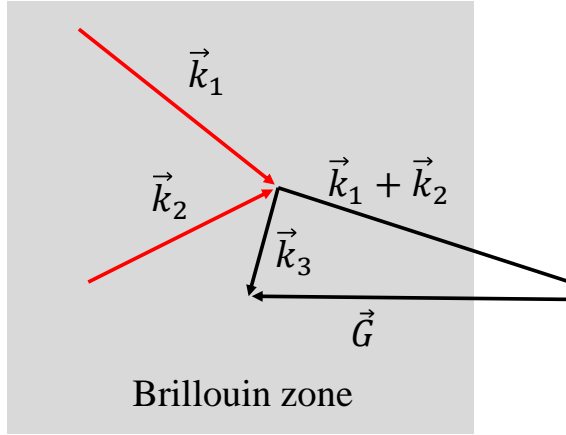


Figure 2.5: A schematic representation to the Umklapp scattering process. In order for the momentum to be conserved, a vector \vec{G} is required to map the resultant phonon back to the Brillouin zone.

and

$$\omega_1 + \omega_2 = \omega_3 \quad (2.12)$$

where \vec{G} is a vector required to map the resultant phonon back into the Brillouin zone. Therefore, the resultant phonon travels in the opposite direction. This last result explains how Umklapp scattering contributes to the thermal resistance. The rate at which Umklapp scattering takes place is dependent on the phonon frequency distribution, which also depends on temperature. Several theoretical and experimental studies reached to the following representation of Umklapp relaxation time [31, 49–52]:

$$\tau_U^{-1} = B\omega^2 T \exp(-C/T) \quad (2.13)$$

where B and C are material dependent constants.

Impurity Scattering

Phonons can also scatter from impurities inside the materials like isotope atoms, point defects, or alloy atoms. This scattering is a result of the randomly distributed mass fluctuations within the periodic lattice. Impurity scattering in alloys (alloy sites

being the impurity) results in a significant reduction in thermal conductivity. It is well established in literature that the impurity scattering relaxation time is [49, 53]:

$$\tau_I^{-1} = A\omega^4 \quad (2.14)$$

where A is a material property that depends on the mass difference between impurities and host atoms and the density of these impurities [53]. The impurity scattering is hence independent of temperature. In alloys, where impurity scattering is dominant, high frequency phonons scatter strongly at alloy sites and the majority of heat is carried by low frequency phonons. In Chapter 4, I will demonstrate the weak temperature dependence of bulk and thin film SiGe alloys thermal conductivities as compared to Si and show that a Debye approximation (see Section 2.2.1) is well suited for modeling thermal transport in alloys.

Boundary Scattering

When phonons' mean free paths become comparable to the dimensions of the material, they scatter at the sample boundary as discussed in Chapter 1. Therefore, the boundary scattering relaxation time is dependent on the dimensions and is usually given by [54]:

$$\tau_L^{-1} = \frac{v(\omega)}{L}. \quad (2.15)$$

For bulk materials, Eq. 2.9 still holds with L set to the actual size of the measured crystal (usually a few millimeters). As discussed in Sec 1.1, boundary scattering in bulk crystals only matters at very low temperatures (~ 10 K). Therefore, a precise knowledge of the dimensions of a bulk crystal is only necessary in case of modeling thermal conductivity at such low temperatures. At higher temperatures, any appreciably large value of L is good for using Eq. 2.9 for bulk materials.

The constants A , B , and C in the above representations of the Umklapp and

impurity scattering are often determined by fitting the experimental data of thermal conductivity versus temperature of bulk material to the model given in Eq. 2.9, with L set to a large number and the temperature range starting at a temperature where boundary scattering effects are negligible. Once these constants are determined, Eq. 2.9 can be applied to a thin film of thickness L , and the influence of size effects on thermal conductivity can be analyzed in terms of the reduction in thermal conductivity as compared to bulk.

2.5 Thermal Boundary Conductance

The thermal boundary conductance, thermal interface conductance, or Kapitza conductance, h_K , is defined as the proportionality constant between the heat flux, q , crossing an interface and the temperature drop near the interface:

$$q = h_K(T_2 - T_1) \quad (2.16)$$

It is hence a measure of how good is a certain interface at conducting/resisting heat flow. In various nanosystems, the Kapitza conductance can dominate thermal transport and it is important to understand the mechanisms governing the scattering at interfaces to better model and measure this quantity [55–59].

In SLs, and in the incoherent regime of the κ_{\min} -approach, thermal conductivity can be modeled by a series thermal resistors model in which the thermal resistance from the interfaces, $1/h_K$, adds in series to the thermal resistance of the SL layers. This idea will be implemented in modeling thermal transport across AlAs-GaAs SLs and Cu-Nb multilayers in Chapters 6 and 7, respectively.

Chapter 3

Time-Domain Thermorefectance (TDTR)

“Heat, like gravity, penetrates every substance of the universe, its rays occupy all parts of space... The theory of heat will hereafter form one of the most important branches of general physics.”

–Joseph Fourier, *Théorie analytique de la chaleur*, 1822

3.1 Background

The idea of a pump-probe thermorefectance technique to measure thermal properties of materials is based on creating a modulated heating event on a metal coated sample with an energetic pump beam. The metal acts as a temperature transducer and allows for monitoring the surface temperature change due to the pump modulation. For small temperature excursions, the change in the reflectance of the metal due to the heating event can be assumed linearly proportional to the surface temperature change. This can be expressed as¹:

¹in some textbooks, the thermorefectance coefficient is defined as: $\beta = \frac{1}{R_o} \frac{\partial R}{\partial T}$ where R_o is the reflectance at ambient temperature

$$\Delta R = \frac{\partial R}{\partial T} \Delta T = \beta \Delta T \quad (3.1)$$

where $\beta = \partial R / \partial T$ is the thermorefectance coefficient and ΔT is the change in temperature due to the heating event. The change in surface temperature is monitored by the change in reflectance of the probe beam, which essentially acts as a thermometer. Surface temperature changes are directly related to the sample thermal properties by solving an appropriate energy transport equation (e.g., the heat diffusion equation) in a multilayered structure.

TDTR has been used for the past three decades to study thermal properties in bulk and thin film structures and across interfaces. The credit in introducing time-domain pump-probe thermorefectance as a thermal measurement technique is often given to Paddock and Eesley [60, 61] who, in 1986, used two pulsed lasers with ≈ 4 ps pulse widths to measure the thermal diffusivity of several metal films and metallic alloys. However, an experimental setup similar to nowadays continuous wave (CW) frequency domain thermorefectance techniques (FDTR) [62–64] was utilized three years earlier by Opsal, Rosencewaig, and co-workers [65] to measure the thickness of thin SiO₂ films grown on Si substrates. In their experiment, the sample thermoelastic response to the modulated CW pump beam caused a deflection in the reflected probe beam that was detected by a position sensitive photodetector. Two years later, i.e., in 1985, they used the same apparatus, samples, and thermal model to achieve the same thickness measurements looking at the intensity variation in the reflected probe beam due to the thermorefectance response. Several Improvements and variations of the pump-probe thermorefectance measurements followed by several groups later [62, 64, 66–70].

Two of the main variations in current TDTR systems are the double color [70] and the two-tint arrangements [69]. For the double color pump-probe, as the name suggests, the two beams are of different colors (“blue” at 400 nm and “red” at 800

nm wavelengths, in our case) whereas for the two-tint arrangement sharp edged filters are used to separate the pump and probe beams off the laser output spectrum. The two variations use the same electronic detection method and thermal model solution and differ only in the optical arrangement. Therefore, one would expect that both variations should yield the same output and either one is enough to conduct thermal measurements. However, over the course of this PhD, I improved measurement uncertainties and additional potential errors due to systematic experimental variations by superimposing the double color and two-tint variations on the same optical table. In this chapter, I briefly describe the two variations and the gain from having both of them available for thermal measurements. I also provide the solution for the heat equation in a multilayered structure and the response of the lock-in amplifier used for fitting the data and model to extract thermal properties.

Before we start, it is important to note that this chapter does not provide the most thorough description of TDTR systems but is rather structured to focus on areas that were either ignored or not given in detail in the literature. For instance, the large number of parameters involved in the thermal analysis and the use of Fourier and Hankel transforms and their inverses to obtain the electronics response can make the presented equations extremely confusing. One can easily lose track of whether the given equation is in time, frequency, or Hankel space over the course of the solution. For these reasons, the solution of the heat transfer problem and the lock-in amplifier response given in this chapter are presented in a “step-by-step” manner to facilitate the understanding to the reader. The choice of this rather lengthy mathematical derivations is a direct result of the struggles I personally experienced when I started studying TDTR several years ago.

3.2 Optical Setup: Double Color and Two-Tint

Figure 3.1 shows the main components of the TDTR system present in room 037 of the Physical and Life Sciences Building at the University of Virginia. The components for the two-tint setup and their corresponding laser beams are shown with dashed boundaries; note, we have built a clone of the two-tint set up in room 117 of the Mechanical Engineering Building at the University of Virginia. In this setup, a Ti:Sapphire laser emits a train of sub-picosecond, 80 MHz light pulses at a central wavelength of 800 nm. A polarizing beam splitter separates the laser output into two paths, a pump and a probe. The pump beam is modulated by an electro-optic modulator (EOM) at a frequency typically in the range 1 - 10 MHz. For measurements in this dissertation, the modulation frequency was ~ 10 MHz. The probe is directed along a mechanical delay stage that controls the relative optical path difference between the two beams. Both the pump and the probe are coaxially focused on the sample by an objective lens. The samples are usually coated with a metal film of thickness $\sim 50 - 100$ nm that converts the optical energy from the laser pulses into thermal energy and acts as a temperature transducer. The pump modulation creates an oscillatory temperature rise at the modulation frequency. The probe beam is backreflected into a photodetector carrying a frequency component at the pump modulation frequency. The change in the thermoreflectance signal due to the pump heating is of the order of 10^{-4} K^{-1} (Ref. [71]) and requires the use of a lock-in amplifier. The same modulation signal driving the EOM is supplied to a lock-in amplifier as a reference signal. The cooling of the sample after the created heating event is recorded by monitoring the change in the ratio of the in-phase to out-of-phase components of the lock-in amplifier signal while incrementally varying the time delay between the pump and probe. The time delay is controlled by a mechanical delay stage, which can move in steps that create a pump-probe time delays of a few femtoseconds giving

a temporal resolution that is only limited by the laser pulse width (on the order of ~ 200 fs). The power absorbed by the sample is on the order of few milliwatts and can cause a temperature rise of few Kelvin [68].

For the double color arrangement, the 800 nm pump light is converted into 400 nm light using BiBO (Bismuth Triborate BiB_3O_6) crystal which is a non-linear optical crystal that applies a second harmonic generation to the incident light [72]. This conversion better filters and isolates the pump from the photodetector through the use of long-pass colored optical filter. In this case, a dichroic mirror reflects the “blue” pump light into the sample and transmits the “red” probe light through.

For the two-tint arrangement, a flip mirror is used to reflect the pump beam after the EOM into a different path. In this path, a long pass sharp edged filter is inserted to spectrally isolate the pump wavelength from the laser bandwidth. The pump then gets reflected from a polarizing beam splitter into the sample. Another narrow bandpass filter is inserted in the probe path centered at 785 nm. The laser output wavelength is adjusted to get a maximum signal. The same filter inserted in the probe path is used at the photodetector to isolate the pump from leaking into detection. The laser spectrum and the transmission of the used filters are shown in the left corner of Fig. 3.1.

A sample data set from a TDTR scan is shown in the right corner of Fig. 3.1 and is divided into three time regimes. In the first few picoseconds, electrons in the metal transducer absorb the energy in the pump pulse. Hot electrons thermalize quickly and transfer their energy to the cold lattice. This time regime is suitable to study the physics of nonequilibrium electrons and the dynamics of electron-phonon coupling [67, 74–76]. The rapid, near surface-localized heating of the metal transducer creates a strain wave originating from the pulse-induced thermal expansion that propagates through the transducer at the speed of sound. Due to the acoustic mismatch between the transducer and the film, a portion of the wave gets reflected

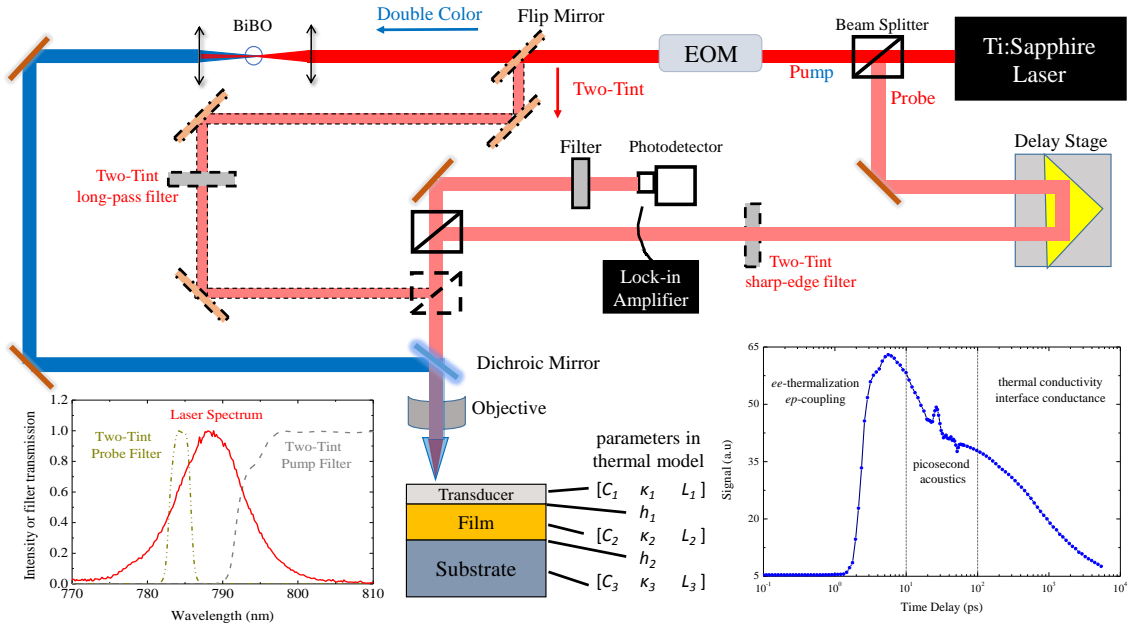


Figure 3.1: A schematic of the main components of the TDTR system [73]. The two-tint components are shown in dashed boundaries. The flip mirror after the EOM directs the pump beam into the two-tint optics. The figure also shows a plot of a typical TDTR measurement on the lower right corner. The plot was shifted by +7 ps to allow for logarithmic scale plot. The laser spectrum and the two-tint optical filters transmission profiles are shown in the lower left corner.

back to the surface and records as an acoustic echo in the thermoreflectance signal. The shape and time at which the echoes occur can be used to determine the thickness of the transducer [7, 8], assess information regarding the atomic bonding and disorder at the interface [77–79], and study the generation, attenuation, and transmission of phonons across interfaces [7, 8, 80–83].

The third time regime corresponds to the diffusion of heat from the transducer to the film via phonon-phonon, electron-electron, or electron-phonon interactions. In a typical TDTR measurement, the data collected in this regime is compared to the solution of the heat diffusion equation in cylindrical coordinates in a multilayer structure. In this solution, each layer has five corresponding parameters. The specific heat capacity, c_p , the mass density, ρ , the layer thickness, L , and the in-plane and cross-plane thermal conductivities, κ_r and κ_z , respectively. The thermal interface conductance,

h , between layers adds an additional unknown to the thermal model. At most, two parameters can be fitted from a single TDTR measurement. The other parameters are often taken from literature or estimated. Data collection is automated by linking and syncing all the components through a Labview code. The sample plot shown in Fig. 3.1 takes ~ 3 minutes to generate. In general, 4-5 measurements are performed on each sample totaling a time of less than 15 minutes. Given the small laser spot sizes used in TDTR (2-100 μm), a typical sample area can be as small as 0.25 cm^2 . This area is mainly for the ease of sample handling. In theory, we can characterize areas as small as the laser spot sizes and TDTR has been utilized to perform thermal conductivity maps with micrometer scale resolutions [84, 85]. The thicknesses of the samples that can be tested using TDTR are only limited by the thermal penetration depth, given by $l = \sqrt{\kappa/(\pi\rho c_p f)}$, where f is the pump modulation frequency. For typical TDTR modulation frequencies (1 MHz - 20 MHz), this depth is on the order of a few ten's of nanometers to a few micrometers, depending on the thermal conductivity and heat capacity of the sample. By changing the pump modulation frequency, we vary the thermal penetration depth and change the measurement sensitivity to the different layers or interfaces at a different depth from the sample surface.

3.3 Heat Transfer Analysis and Lock-in Amplifier Response

In TDTR, the reflected probe measures the change in the sample surface temperature due to the heat input from the modulated pump beam. The goal in this section is to relate the variation in the sample surface temperature to the properties of the materials and interfaces underneath by solving the heat diffusion equation in a multilayer structure. In doing so and using Eq. 3.1, a mathematical expression for the reflected probe is derived. I aim to provide a general solution that can be implemented and easily modified for different TDTR configurations. Then, I derive the lock-in amplifier response corresponding to the specific details of our TDTR system. In literature,

a major part of the solution is overlooked and some key assumptions are not clearly stated. In this section, I provide a step-by-step derivation to the key equations used in TDTR experiments. This derivation should make it easy to any student with reasonable background on Fourier/Hankel transforms and heat transfer to understand the analysis and reproduce the solution results.

3.3.1 Thermal Response

Knowing that the output of our laser contains only the fundamental transverse mode (TEM₀₀), the laser intensity profile can be modeled with a Gaussian function². The heat input due to a time varying pump beam can be mathematically represented by:

$$q_{\text{top}}(r, t) = \frac{2}{\pi r_0^2} \exp\left(\frac{-2r^2}{r_0^2}\right) g_0(t) \quad (3.2)$$

where r_0 is the $1/e^2$ Gaussian beam radius and $g_0(t)$ is a function of time that includes the power absorbed by the sample at the pump wavelength. In this case, $g_0(t)$ has units of Watts [W] and q_{top} has units of [Wm⁻²]. We first consider heat flow in a single layer of thickness L and then generalize the solution for any number of layers. The analysis in this section corresponds to the third time regime shown in Fig. 3.1 starting ~ 100 ps after the pump pulse is absorbed by the sample. Modeling of thermal transport for times less than this requires the consideration of non-equilibrium electron phenomena and electron-phonon coupling [67] which is beyond the scope of this dissertation.

For multi-layered structures and Gaussian beam geometries it is more convenient to solve the heat diffusion equation in cylindrical coordinates. In the time domain,

²For the case of higher order transverse modes denoted TEM _{lp} , the laser intensity profile is given by: $I_{pl}(r, \theta) = P_0 \psi^l (L_p^l(\psi))^2 \cos^2(l\theta) \exp(-\psi)$ where r and θ are the polar coordinates, $\psi = 2r^2/R^2$ where R is the $1/e^2$ Gaussian beam radius, and L_p^l is the associated Laguerre polynomials of order p and index l . For $l, p = 0$ the intensity profile reduces to a Gaussian $P_0 \exp(-\psi)$.

the cylindrical heat equation with radial symmetry³ is given by:

$$\kappa_r \left[\frac{1}{r} \frac{\partial T(r, z, t)}{\partial r} + \frac{\partial^2 T(r, z, t)}{\partial r^2} \right] + \kappa_z \frac{\partial^2 T(r, z, t)}{\partial z^2} = \rho c_p \frac{\partial T(r, z, t)}{\partial t} \quad (3.3)$$

where κ_r and κ_z are the in-plane (parallel to the layer plane) and cross plane (perpendicular to the layer plane) thermal conductivities, ρ is the mass density, and c is the specific heat capacity. The heat source was not included in the heat equation; instead the source is treated as a boundary condition which considerably simplifies the solution. The boundary and initial conditions are:

$$T(0, r, t) = T_{\text{top}}(r, t) = T_{\text{top}}; \quad \left. \frac{\partial T(z, r, t)}{\partial z} \right|_{z=0} = \frac{-1}{\kappa_z} q_{\text{top}}(0, r, t) = \frac{-1}{\kappa_z} q_{\text{top}} \quad (3.4)$$

$$T(L, r, t) = T_{\text{bot}}(r, t) = T_{\text{bot}}; \quad \left. \frac{\partial T(z, r, t)}{\partial z} \right|_{z=L} = \frac{-1}{\kappa_z} q_{\text{bot}}(L, r, t) = \frac{-1}{\kappa_z} q_{\text{bot}} \quad (3.5)$$

$$\text{at } t = 0 \quad T(z, r, 0) = 0 \quad (3.6)$$

where T_{top} and T_{bot} are the temperatures at the top and bottom surfaces and q_{top} and q_{bot} are the heat fluxes across the top and bottom surfaces. We note that the initial temperature is set to zero since we are interested in the *change* in surface temperature due to the pump heating. If we were to solve for the absolute surface temperature, $T(z, r, 0)$ can be set to the temperature at which the TDTR measurement was performed.

First, we apply a zeroth order Hankel transform⁴, \mathcal{H}_0 , with respect to the r coordinate. The Hankel transform method is particularly suitable for heat transfer

³This form of the heat equation assumes that we are dealing with an orthotropic material. In other words, the off diagonal terms of the thermal conductivity tensor are all zeros which is a valid assumption for all the material systems studied in this work.

⁴Hankel transform is given by: $\tilde{y}(\chi) = \mathcal{H}_0\{y(r)\} = \int_0^\infty y(r) J_0(\chi r) r dr$ where J_0 is the Bessel function of first kind and order 0 and χ is the Hankel transform domain variable.

problems with cylindrical symmetry. Second, we apply Fourier transform⁵, \mathcal{F} , with respect to time to find the solution in the frequency domain. If needed, the time domain solution can be obtained by applying an inverse Fourier transform to the frequency domain solution.

The first term of Eq. 3.3 is κ_r multiplied by the Bessel differential operator of zeroth order given by: $\Delta_r = \frac{1}{r} \frac{\partial}{\partial r} + \frac{\partial^2}{\partial r^2}$. Using the Hankel transform property: $\mathcal{H}_0\{\Delta_r y(r)\} = -\chi^2 \tilde{y}(\chi)$, where $\tilde{y}(\chi) = \mathcal{H}_0\{y(r)\}$ and χ is the Hankel transform domain variable, the heat equation becomes:

$$-\kappa_r \chi^2 \tilde{\mathcal{T}}(z, \chi, \omega) + \kappa_z \frac{\partial^2 \tilde{\mathcal{T}}(z, \chi, \omega)}{\partial z^2} = \rho c i \omega \tilde{\mathcal{T}}(z, \chi, \omega) \quad (3.7)$$

where $\tilde{\mathcal{T}}(z, \chi, \omega) = \mathcal{F}\{\tilde{T}(z, \chi, t)\}$ with $\tilde{T}(z, \chi, t) = \mathcal{H}_0\{T(z, r, t)\}$ and $\omega = 2\pi f$ is the angular frequency in rad s⁻¹. For the rest of this chapter, the calligraphic representation and the use of the tilde symbol “ ~ ” on top of a certain variable is to emphasize that we are in the Fourier or Hankel transform domains, respectively. We also use subscripts ₀ and ₁ for variables or functions representing the pump and probe beams, respectively. Now we define:

$$\mu^2 = \frac{\kappa_r \chi^2 + i \rho c \omega}{\kappa_z} \quad (3.8)$$

and rearrange the heat equation:

$$\frac{\partial^2 \tilde{\mathcal{T}}(z, \chi, \omega)}{\partial z^2} - \mu^2 \tilde{\mathcal{T}}(z, \chi, \omega) = 0 \quad (3.9)$$

which has the solution form:

$$\tilde{\mathcal{T}}(z, \chi, \omega) = a \cosh(\mu z) + b \sinh(\mu z) \quad (3.10)$$

⁵the Fourier transform is defined by: $\mathcal{Y}(\omega) = \mathcal{F}\{y(t)\} = \int_{-\infty}^{\infty} e^{-i\omega t} y(t) dt$ where ω is the angular frequency in rad s⁻¹.

with \cosh and \sinh being the hyperbolic cosine and sine, respectively, and a and b are constants. The new boundary conditions are:

$$\tilde{\mathcal{T}}(0, \chi, \omega) = \tilde{\mathcal{T}}_{\text{top}}(\chi, \omega) = \tilde{\mathcal{T}}_{\text{top}}; \quad \left. \frac{\partial \tilde{\mathcal{T}}(z, \chi, \omega)}{\partial z} \right|_{z=0} = \frac{-1}{\kappa_z} \tilde{\mathbf{q}}_{\text{top}}(0, \chi, \omega) = \frac{-1}{\kappa_z} \tilde{\mathbf{q}}_{\text{top}} \quad (3.11)$$

$$\tilde{\mathcal{T}}(L, \chi, \omega) = \tilde{\mathcal{T}}_{\text{bot}}(\chi, \omega) = \tilde{\mathcal{T}}_{\text{bot}}; \quad \left. \frac{\partial \tilde{\mathcal{T}}(z, \chi, \omega)}{\partial z} \right|_{z=L} = \frac{-1}{\kappa_z} \tilde{\mathbf{q}}_{\text{bot}}(L, \chi, \omega) = \frac{-1}{\kappa_z} \tilde{\mathbf{q}}_{\text{bot}} \quad (3.12)$$

Applying the boundary conditions to Eq. 3.10 we reach:

$$\tilde{\mathcal{T}}(z, \chi, \omega) = \cosh(\mu z) \tilde{\mathcal{T}}_{\text{top}} - \frac{1}{\kappa_z \mu} \sinh(\mu z) \tilde{\mathbf{q}}_{\text{top}} \quad (3.13)$$

$$\tilde{\mathbf{q}}(z, \chi, \omega) = -\kappa_z \mu \sinh(\mu z) \tilde{\mathcal{T}}_{\text{top}} + \cosh(\mu z) \tilde{\mathbf{q}}_{\text{top}} \quad (3.14)$$

The above two equations allow for the construction of a transfer matrix $\tilde{\mathcal{M}}$ that relates the heat flux and temperature at any point $z \leq L$ beneath the layer surface to the temperature and heat flux at the surface. For $z = L$, we have: $\tilde{\mathcal{T}}(L, \chi, \omega) = \tilde{\mathcal{T}}_{\text{bot}}$ and $\tilde{\mathbf{q}}(L, \chi, \omega) = \tilde{\mathbf{q}}_{\text{bot}}$ and we can then write [86]:

$$\begin{bmatrix} \tilde{\mathcal{T}}_{\text{bot}} \\ \tilde{\mathbf{q}}_{\text{bot}} \end{bmatrix} = \begin{bmatrix} \cosh(\mu L) & \frac{-1}{\kappa_z \mu} \sinh(\mu L) \\ -\kappa_z \mu \sinh(\mu L) & \cosh(\mu L) \end{bmatrix} \begin{bmatrix} \tilde{\mathcal{T}}_{\text{top}} \\ \tilde{\mathbf{q}}_{\text{top}} \end{bmatrix} \quad (3.15)$$

This result can be generalized for multilayers by multiplying the matrices of each individual layer. For n -layers, each with matrix $\tilde{\mathcal{M}}_i$ with $i = 1, 2, \dots, n$, we can relate the temperature at the top and bottom surfaces of the stack of layers through:

$$\begin{bmatrix} \tilde{\mathcal{T}}_{\text{bot},n} \\ \tilde{\mathbf{q}}_{\text{bot},n} \end{bmatrix} = \tilde{\mathcal{M}}_n \tilde{\mathcal{M}}_{n-1} \dots \tilde{\mathcal{M}}_{i+1} \tilde{\mathcal{M}}_i \dots \tilde{\mathcal{M}}_1 \begin{bmatrix} \tilde{\mathcal{T}}_{\text{top}} \\ \tilde{\mathbf{q}}_{\text{top}} \end{bmatrix} = \prod_{i=1}^n \tilde{\mathcal{M}}_i \begin{bmatrix} \tilde{\mathcal{T}}_{\text{top}} \\ \tilde{\mathbf{q}}_{\text{top}} \end{bmatrix} \quad (3.16)$$

Each matrix $\tilde{\mathcal{M}}_i$ contains the thickness, the mass density, the specific heat capacity, and the cross-plane and in-plane thermal conductivities of the layer i . The thermal interface conductance between two layers a and b (a being closer to the heat source), h_{ab} , can be modeled as a layer with zero thickness and zero heat capacity and is related to the flux across and temperatures on either side of the interface by:

$$\begin{bmatrix} \tilde{\mathcal{T}}_b \\ \tilde{\mathcal{q}}_b \end{bmatrix} = \begin{bmatrix} 1 & -\frac{1}{h_{ab}} \\ 0 & 1 \end{bmatrix} \begin{bmatrix} \tilde{\mathcal{T}}_a \\ \tilde{\mathcal{q}}_a \end{bmatrix}. \quad (3.17)$$

clearly Eq. 3.17 reduces to $\tilde{\mathcal{q}}_a = h_{a,b}(\tilde{\mathcal{T}}_a - \tilde{\mathcal{T}}_b)$ which is the definition of the interface conductance given by Eq. 2.16 in Chapter 2.

All the thin film structures studied in this work were grown on bulk substrates of thicknesses of the order of few hundreds of micrometers. As pointed earlier, the thermal penetration depth in TDTR is of the order of few microns at the lowest modulation frequencies. Therefore, we can apply a semi-adiabatic boundary condition on the bottom surface of the stack. In this case we get:

$$\tilde{\mathcal{q}}_{\text{bot},n} = 0 \quad (3.18)$$

Setting $\prod_{i=n}^{i=1} \tilde{\mathcal{M}}_i = \begin{bmatrix} \tilde{\mathcal{A}} & \tilde{\mathcal{B}} \\ \tilde{\mathcal{C}} & \tilde{\mathcal{D}} \end{bmatrix}$ and applying the above boundary condition to Eq. 3.16 leads to:

$$\tilde{\mathcal{T}}_{\text{top}} = -\frac{\tilde{\mathcal{D}}}{\tilde{\mathcal{C}}} \tilde{\mathcal{q}}_{\text{top}} \quad (3.19)$$

The heat flux at the top surface was given in real space and time domain by Eq. 3.2. Knowing that $\mathcal{H}_0\{e^{-ar^2}\} = \frac{1}{2a^2}e^{-x^2/(4a^2)}$ the heat flux on the top surface in the Fourier

and Hankel transform domains⁶:

$$\tilde{q}_{\text{top}} = \frac{1}{2\pi} \exp\left(\frac{-\chi^2 r_0^2}{8}\right) \mathcal{G}_0(\omega) \quad (3.20)$$

where $\mathcal{G}_0(\omega) = \mathcal{F}\{g_0(t)\}$. Note that $g_0(t)$ is only a function of time (no r -dependence) and hence $\mathcal{G}_0(\omega)$ has no χ dependence and no tilde symbol is used to express this variable. Therefore, the frequency domain solution for the surface temperature in the Hankel transform domain is:

$$\tilde{\mathcal{T}}_{\text{top}} = \tilde{\mathcal{T}}(0, \chi, \omega) = \frac{1}{2\pi} \left(\frac{-\tilde{\mathcal{D}}}{\tilde{\mathcal{C}}}\right) \exp\left(\frac{-\chi^2 r_0^2}{8}\right) \mathcal{G}_0(\omega) \quad (3.21)$$

To retrieve the frequency domain solution in real space (i.e., in the r -space), we apply an inverse Hankel transform:

$$\begin{aligned} \mathcal{T}_{\text{top}} = \mathcal{T}_{\text{top}}(r, \omega) &= \mathcal{H}_0^{-1}\{\tilde{\mathcal{T}}(0, \chi, \omega)\} = \\ &= \left[\frac{1}{2\pi} \int_0^\infty \chi J_0(\chi r) \left(\frac{-\tilde{\mathcal{D}}}{\tilde{\mathcal{C}}}\right) \exp\left(\frac{-\chi^2 r_0^2}{8}\right) d\chi \right] \mathcal{G}_0(\omega) = \mathcal{L}_0(r, \omega) \mathcal{G}_0(\omega) \end{aligned} \quad (3.22)$$

where $\mathcal{L}_0(r, \omega)$ is the term between brackets. The dependence of $\mathcal{L}_0(r, \omega)$ on ω comes from the $\tilde{\mathcal{D}}/\tilde{\mathcal{C}}$ term. The above equation is the surface temperature rise due to a time varying pump beam with Gaussian intensity profile in the frequency domain. Once the top temperature and flux are known, the temperatures and fluxes at the top and bottom of each layer can be calculated in the same way using Eq. 3.16 and values for intermediate points within each layer can be found using Eqs. 3.13 and 3.14 (Ref. [86]).

⁶Note that: $\tilde{q}_{\text{top}} = \tilde{q}_{\text{top}}(\chi, \omega) = \mathcal{F}\{\tilde{q}_{\text{top}}(\chi, t)\}$ and $\tilde{q}_{\text{top}}(\chi, t) = \mathcal{H}_0\{q(r, t)\}$

The time domain solution can be obtained by applying an Inverse Fourier transform:

$$T_{\text{top}} = T(0, r, t) = \mathcal{F}^{-1}\{\mathcal{T}_{\text{top}}(0, r, \omega)\} = \int_{-\infty}^{+\infty} \mathcal{T}_{\text{top}}(0, r, \omega) e^{-i\omega t} d\omega \quad (3.23)$$

The generality of the obtained time and frequency solutions allows for the calculation of the surface temperature rise in any multilayer structure by simply substituting the Fourier transform of the time dependent part of a Gaussian heat source.

The probe beam is reflected off this temperature rise which causes a change in its intensity. In the time domain, the reflected probe beam, p_r , can be expressed in terms of the incident probe beam, p_i , and surface temperature rise T_{top} by:

$$p_r(r, t) = \Delta R \times p_i(r, t) = [\beta T_{\text{top}}(r, t)] \times p_i(r, t) \quad (3.24)$$

where once again β is the thermorefectance coefficient. Similar to Eq. 3.2, p_i is given by:

$$p_i(r, t) = \frac{2}{\pi r_1^2} \exp\left(\frac{-2r^2}{r_1^2}\right) g_1(t) \quad (3.25)$$

where r_1 is the $1/e^2$ Gaussian beam radius and $g_1(t)$ is a function of time that includes the power in the probe beam. In the frequency-domain, the multiplication given in Eq. 3.24 becomes a convolution:

$$\begin{aligned} \mathbf{p}_r(r, \omega) &= \mathcal{F}\{p_r(r, t)\} = \beta \mathcal{F}\{T_{\text{top}}(r, t) \times p_i(r, t)\} = \\ &= \beta \mathcal{T}_{\text{top}}(r, \omega) * \mathbf{p}_i(r, \omega) = \beta \int_{-\infty}^{+\infty} \mathcal{T}_{\text{top}}(r, \omega') \mathbf{p}_i(r, \omega - \omega') d\omega' \\ &= \beta \int_{-\infty}^{+\infty} \mathcal{L}_0(r, \omega') \mathcal{G}_0(\omega') L_1(r) \mathcal{G}_1(\omega - \omega') d\omega' \quad (3.26) \end{aligned}$$

where $L_1(r) = \frac{2}{\pi r_1^2} \exp\left(\frac{-2r^2}{r_1^2}\right)$ and $\mathbf{p}_i(r, \omega) = \mathcal{F}\{p_i(r, t)\} = L_1(r) \mathcal{G}_1(\omega)$. The above two representations of the reflected probe are independent of the detection method and they can be explicitly determined by simply specifying $g_0(t)$, $g_1(t)$, and their transforms for the corresponding pump-probe system. One might use the same equations for a CW-CW, CW-pulsed, or pulsed-CW pump-probe experiments. In some pump-probe experiments, an optical chopper is used to modulate the probe beam at sub kHz frequencies to minimize the effect of pump light backscattering into the photodetector. In the given representation, this can be easily included by substituting the corresponding $g_1(t)$ for the modulated probe beam.

3.3.2 Photodetector Response

The first detection component encountered by the reflected probe is the photodetector. The photodetector returns an electric signal that represents the sum of the collective excitations on the active area due to the reflected probe. Hence, we integrate Eq. 3.24 over the probe area to obtain the photodetector response:

$$\mathcal{V}_{\text{PD}}(\omega) = \int_0^{\infty} \mathbf{p}_r(r, \omega) 2\pi r dr = \beta \int_0^{\infty} \int_{-\infty}^{+\infty} \mathcal{L}_0(r, \omega') \mathcal{G}_0(\omega') L_1(r) \mathcal{G}_1(\omega - \omega') d\omega' 2\pi r dr \quad (3.27)$$

where the subscript PD stands for photodetector signal. A simplification can be applied to the above equation that reduces it into a single integral and eliminates the r dependence. This is given in Appendix A. For now we note that:

$$\int_0^{\infty} \mathcal{L}_0(r, \omega) L_1(r) 2\pi r dr = \frac{1}{2\pi} \int_0^{\infty} \chi \left(\frac{-\tilde{\mathcal{D}}}{\tilde{\mathcal{C}}} \right) \exp\left(\frac{-\chi^2 (r_0^2 + r_1^2)}{8}\right) d\chi = \mathcal{L}_{01}(\omega) \quad (3.28)$$

and Eq. 3.27 reads:

$$\mathcal{V}_{\text{PD}}(\omega) = \beta \int_{-\infty}^{+\infty} \mathcal{L}_{01}(\omega') \mathcal{G}_0(\omega') \mathcal{G}_1(\omega - \omega') d\omega' \quad (3.29)$$

We can now use this equation and mathematically represent our pump and probe beams to obtain the lock-in amplifier response.

3.3.3 Lock-in Amplifier Response

In our TDTR system, the laser emits a train of 200 fs pulses at a repetition rate, f_s , of 80 MHz leading to a time between pulses, $\Gamma = 1/f_s$, of 12.5 ns. This time is not generally enough⁷ for a system to return to equilibrium after a pump heating event. As a result, we need to account for the accumulation effects from the successive laser pulses [70, 87] and both the pump and probe beams need be represented as trains of pulses. Given that the laser pulse width (~ 100 fs emanating from the laser, and although it is broadened from the various optics in the pump and probe paths, it remains < 1 ps at the sample surface) is small compared to the timescale of the surface temperature variation (> 12.5 ns), we can mathematically represent a laser pulse as a Dirac-delta function of time, $\delta(t)$. For thermal phenomenon taking place in the first 100 ps, a Gaussian pulse of time is often used to study nonequilibrium effects and electron-phonon coupling. As a result, the analysis in this section is valid for time delays larger than ~ 100 ps.

The time varying functions $g_0(t)$ and $g_1(t)$ and their transforms can be represented by:

$$g_0(t) = \alpha E_0 e^{i\omega_0 t} \sum_{n=-\infty}^{+\infty} \delta(t - n\Gamma) \quad (3.30)$$

⁷this depends on the sample thermal diffusivity. For highly conductive materials like diamond, 12.5 ns is actually enough to return to equilibrium.

$$\mathcal{G}_0(\omega) = \alpha E_0 \sum_{n=-\infty}^{+\infty} e^{i(\omega_0 - \omega)n\Gamma} = \frac{2\pi\alpha E_0}{\Gamma} \sum_{n=-\infty}^{+\infty} \delta(\omega - \omega_0 - n\omega_s) \quad (3.31)$$

$$g_1(t) = E_1 \sum_{m=-\infty}^{+\infty} \delta(t - m\Gamma - \tau) \quad (3.32)$$

$$\mathcal{G}_1(\omega) = E_1 \sum_{m=-\infty}^{+\infty} e^{-i\omega(m\Gamma + \tau)} = E_1 e^{-i\omega\tau} \sum_{m=-\infty}^{+\infty} \delta(\omega - m\omega_s) \quad (3.33)$$

where τ is the time delay between the pump and probe pulses, E_0 and E_1 are the energy per pump and probe pulses, respectively, α is the sample absorptivity, and $\omega_s = 2\pi f_s$. To obtain the right hand side of Eqs 3.31 and 3.33 we used the following representation for a train of Dirac-delta functions with period $\Gamma = 2\pi/\omega_s$ [88]:

$$\sum_{m=-\infty}^{+\infty} e^{\pm im\omega\Gamma} = \frac{2\pi}{\Gamma} \sum_{m=-\infty}^{+\infty} \delta\left(\omega - \frac{2\pi m}{\Gamma}\right) = \omega_s \sum_{m=-\infty}^{+\infty} \delta(\omega - m\omega_s) \quad (3.34)$$

We note that we used a complex exponential function to represent the pump modulation (our reference signal) rather than a trigonometric function since it is easier to deal with exponentials in the frequency domain. Once we obtain the final Lock-in response, we shall only consider the real part of the solution. The pump modulation signal form is depicted in Fig. 3.2(a). The time delay between the pump and probe beams along with the surface temperature resulting from the pump modulation are shown in Fig. 3.2(b)

Substituting Eqs 3.31 and 3.33 into Eq. 3.29 and using the Dirac-Delta function

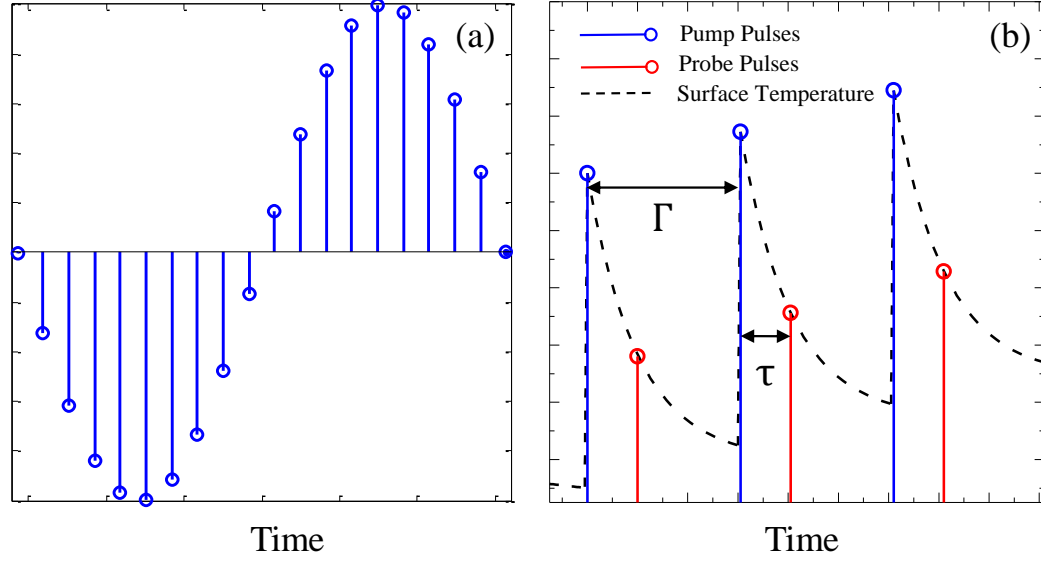


Figure 3.2: (a) Pump beam representation showing a sine wave modulation waveform (b) A representation of the pump and probe pulses along with the surface temperature between pulses. The time between pulses in Γ and the time between the pump and the probe is τ .

properties $\delta(\omega) = \delta(-\omega)$ and $\int_{-\infty}^{+\infty} y(\omega') \delta(\omega' - a) d\omega' = y(a)$ we get:

$$\begin{aligned} \mathcal{V}_{PD}(\omega) &= \frac{2\pi\alpha\beta E_0 E_1}{\Gamma^2} \times \\ &\int_{-\infty}^{+\infty} \sum_{m=-\infty}^{+\infty} \sum_{n=-\infty}^{+\infty} \mathcal{L}_{01}(\omega') \delta(\omega' - \omega_0 - n\omega_s) e^{i(\omega' - \omega)\tau} \delta(\omega' - \omega + m\omega_s) d\omega' = \\ &\frac{2\pi\alpha\beta E_0 E_1}{\Gamma^2} \sum_{m=-\infty}^{+\infty} \sum_{n=-\infty}^{+\infty} \mathcal{L}_{01}(\omega - m\omega_s) \delta(\omega - \omega_0 - (m+n)\omega_s) e^{-im\omega_s\tau} \quad (3.35) \end{aligned}$$

Clearly, the delta functions will evaluate to zero for all values of ω except $\omega = \omega_0 + (m+n)\omega_s$. The lock-in amplifier will filter all frequencies outside a narrow band around ω_0 . This requires $m = -n$ and $\omega = \omega_0$. Therefore, the lock-in amplifier response can be written as:

$$\mathcal{V}_{LA}(\omega) = \frac{2\pi\alpha\beta E_0 E_1 G}{\Gamma^2} \sum_{n=-\infty}^{+\infty} \mathcal{L}_{01}(\omega_0 + n\omega_s) \delta(\omega - \omega_0) e^{in\omega_s\tau} \quad (3.36)$$

Where LA stands for Lock-in Amplifier and G is a multiplicative constant which contains any gain in the electronics (e.g., amplification from the photodetector, filter, pre-amplifier, etc.). To retrieve the response in the time domain, we take the inverse Fourier transform:

$$V_{\text{LA}}(t) = \left[\frac{2\pi\alpha\beta E_0 E_1 G}{\Gamma^2} \sum_{n=-\infty}^{+\infty} \mathcal{L}_{01}(\omega_0 + n\omega_s) e^{in\omega_s\tau} \right] e^{i\omega_0 t} = Z(\omega_0) e^{i\omega_0 t} \quad (3.37)$$

Equation 3.37 expresses the lock-in response as a transfer function $Z(\omega_0)$ acting on the reference signal $e^{i\omega_0 t}$ where $Z(\omega_0)$ represents our system. This system includes the sample thermal properties, the laser geometry and its time dependent profile, and the detection components. Since we started with a complex exponential the actual lock-in amplifier response is the real part of Eq. 3.37. We can write:

$$\begin{aligned} V_{\text{LA}}(t) &= [\text{Re}\{Z(\omega_0)\} + i\text{Im}\{Z(\omega_0)\}] e^{i\omega_0 t} = \\ &= [\text{Re}\{Z(\omega_0)\} \cos(\omega_0 t) - \text{Im}\{Z(\omega_0)\} \sin(\omega_0 t)] + \\ &= i [\text{Re}\{Z(\omega_0)\} \sin(\omega_0 t) + \text{Im}\{Z(\omega_0)\} \cos(\omega_0 t)] \quad (3.38) \end{aligned}$$

Hence the physical signal returned by the lock-in amplifier is the real part of $V_{\text{LA}}(t)$:

$$\text{Re}\{V_{\text{LA}}(t)\} = \text{Re}\{Z(\omega_0)\} \cos(\omega_0 t) - \text{Im}\{Z(\omega_0)\} \sin(\omega_0 t) \quad (3.39)$$

This equation expresses the lock-in amplifier physical signal as an in-phase component, $\text{Re}\{Z(\omega_0)\}$, and out-of-phase component, $\text{Im}\{Z(\omega_0)\}$. These two components are the output display of the Lock-in amplifier.

3.4 Post Processing

A TDTR measurement performed in the lab yields an output text file with three columns listing the time delay between the pump and probe beams, the in-phase ($V_{\text{in}} = \text{Re}\{Z(\omega_0)\}$), and out-of-phase ($V_{\text{out}} = \text{Im}\{Z(\omega_0)\}$) components of the lock-in signal. The magnitude, M , the ratio, $V_{\text{in}}/V_{\text{out}}$ and phase, ϕ , of the signal can be calculated from:

$$M = \sqrt{V_{\text{in}}^2 + V_{\text{out}}^2} \quad (3.40)$$

$$\phi = \tan^{-1} \left(\frac{-V_{\text{out}}}{V_{\text{in}}} \right) \quad (3.41)$$

$$\text{ratio} = \frac{-V_{\text{in}}}{V_{\text{out}}} \quad (3.42)$$

In principle any of these five quantities can be used to fit the data to its corresponding mathematical representation given in Eq. 3.39. The use of V_{in} , V_{out} , or M , requires normalizing the collected data by the multiplicative constant, $\frac{2\pi\alpha\beta E_0 E_1 G}{\Gamma^2}$. While this factor should theoretically be time independent, in practice, it might fluctuate due to electronic and optical noise, and the best fit result could become dependent on the time delay at which the normalization was performed. We can avoid normalization by using the ratio or phase. In addition, using the phase or ratio allows for correcting some of the experiment nonidealities. For instance, V_{in} and V_{out} are changed by the same factor by defocusing of the pump beam and changes in the pump-probe overlap, and therefore $V_{\text{in}}/V_{\text{out}}$ is a more robust measurement than V_{in} and V_{out} alone.

The data from the ratio is fitted to the model in Eq. 3.39 using a least-square minimization routine.

3.5 Sensitivity Analysis

In order for any experimental measurement to confidently return a certain parameter of interest, the measurement should have a high sensitivity to this parameter (e.g., thermal conductivity, thermal boundary conductance) and low sensitivity to other parameters that are either measured independently (e.g., beam spot size, transducer thickness) or taken from literature (e.g., heat capacities). In other words, the sensitivity is a measure of how strongly the thermal model depends on the parameter being measured while hoping for the thermal model to be weakly dependent on other parameters. To quantify the sensitivity we use the approach by Costescu *et al.* [89] where the sensitivity of the ratio to a parameter x is defined by:

$$S_x = \frac{\partial(-V_{\text{in}}/V_{\text{out}})}{\partial \ln(x)} \quad (3.43)$$

A sensitivity analysis was performed prior to considering any of the samples studied in this dissertation for measurements. An example sensitivity analysis is given in Chapter 5, but we emphasize that the same analysis was performed on every material system studied in this work.

3.6 Calibration Results and Comparison

The TDTR measurement data for the ratio of the in-phase to out-of-phase components of the lock-in amplifier and best fit model calculations on three calibration samples are shown in Fig. 3.3(a) as a function of the time delay between the pump and the probe using two-tint and double color arrangements. Figure 3.3(b) shows the best fit values for thermal conductivity for the three tested samples. The three samples were coated with ~ 80 nm of aluminum. The results show a good agreement between two-tint and double color and literature values [46, 90–94]. The results for

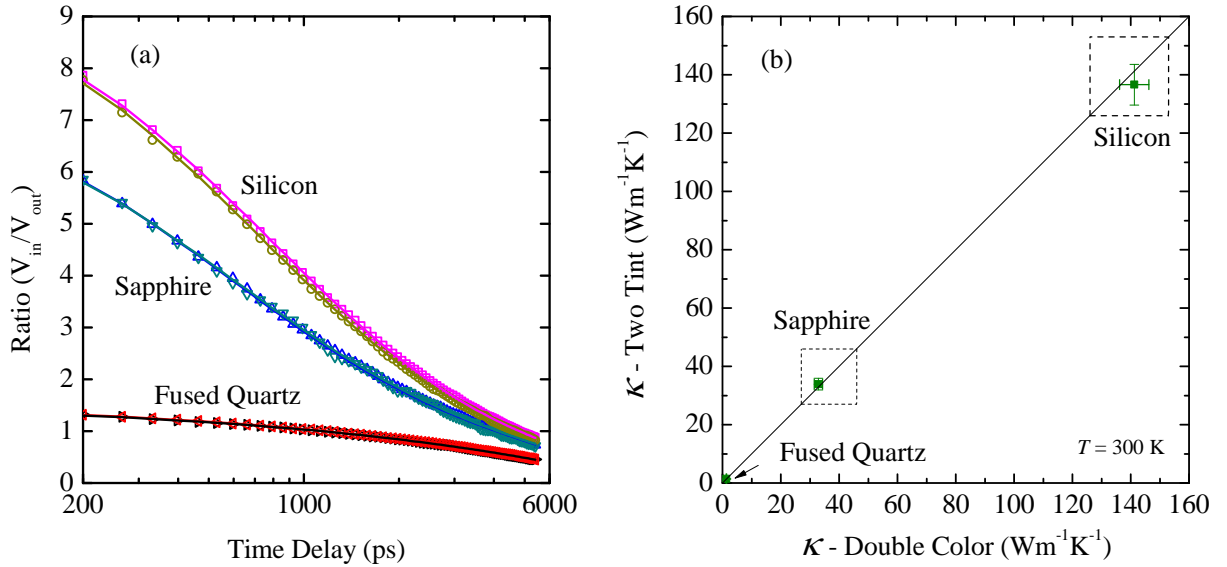


Figure 3.3: (a) Data (symbols) and best fit model calculations (solid lines) for TDTR measurements on silicon, sapphire, and fused quartz using two-tint and double color. (b) The best fit values for the thermal conductivity measurements shown in (a) using two-tint and double color. The solid line represents the first bisector. The dashed squares in (b) represents the spread in the values in literature.

both thermal conductivity, κ , and thermal boundary conductance, h , are also tabulated in Table 3.1. Note that for low thermal conductivity materials, TDTR becomes insensitive to h . For this reason, we do not report a value for the thermal interface conductance between aluminum and fused quartz in Table 3.1.

The choice between two-tint and double-color arrangements depends on the studied samples and the used spot sizes. The BiBO crystal introduces some nonidealities into the pump beam shape that may affect the measurement in the case of using small spot sizes. For electron-phonon coupling measurements, the absorption of the metal coating at the pump beam wavelength affects the electron temperature in the first few picoseconds of the heating event. For instance, gold absorption at 400 nm is an order of magnitude greater than that at 800 nm and the use of double color is favored in the case where the user needs to study electron dynamics at elevated temperatures.

Table 3.1: Thermal conductivity, κ , and thermal boundary conductance, h_K results for calibration sample measured using double color and two-tint arrangements

Sample	κ -two-tint ($\text{Wm}^{-1}\text{K}^{-1}$)	κ -double-color ($\text{Wm}^{-1}\text{K}^{-1}$)	h -two-tint ($\text{MWm}^{-2}\text{K}^{-1}$)	h -double-color ($\text{MWm}^{-2}\text{K}^{-1}$)
Fused Quartz	1.43 ± 0.14	1.41 ± 0.1	-	-
Sapphire	34.5 ± 2	33.7 ± 1.4	310 ± 27.5	302 ± 5.1
Silicon	136.6 ± 7	141.2 ± 4.9	195 ± 7.1	210 ± 4.7

Over the course of this PhD, we ran into problems with the BiBO crystal. Aging, combined with dust accumulation and thermal fluctuations caused some instabilities in the crystal conversion efficiency. The two-tint arrangement was integrated into the double color setup within a week of identifying these BiBO issues and provided a solution for any instabilities that might arise from new BiBO crystals in the future. The two-tint method requires tuning the laser wavelength to 787 nm. Operating the laser at this particular wavelength showed some instabilities at a later point and required laser cavity cleaning and realignment by a laser technologist. Having two-tint and double arrangements fully functional on the same optical table allowed for easily switching between the two in case of any technical difficulties, resulting in reduced experimental down time.

The cost of the optics needed for the double color arrangement (BiBO, dichroic mirror, color filters) can be appreciably cheaper than the sharp edged filters needed for the two-tint. The full width at half maximum of our laser spectrum is only ~ 12 nm and requires expensive filters to allow for splitting such a narrow bandwidth between the two beams. In the case where the laser spectrum is broader (~ 50 nm) cheaper filters can be used and the cost of the two-tint can be lessened to approach that of the double color.

3.7 Sources of Error

The complication in TDTR setup and in the measurement procedure requires careful consideration to the sources of error. A slight beam misalignment across the stage can lead to a significant change in the probe spot size or a lateral shift with respect to the pump while measurements are carried out. In our setup, we use several optical irises to maintain the same beam height across the laser table. The irises allow for easily checking and fixing alignment on a daily basis.

The pump and probe spot sizes are measured using a beam profiler (Thorlabs BP209-VIS) which has a resolution of $\sim 0.5 \mu\text{m}$. We use a spot of $50 \mu\text{m}$ for the pump and $20 \mu\text{m}$ for the probe for all the measurements in this work. These spot sizes are large enough that a 20% error in the spot size measurement results in no more than 1% error in the reported thermal conductivity for measurements done at ~ 10 MHz modulation frequency.

The main source of error in our measurement is the thickness of the metal transducer. A 5% error in the transducer thickness can lead to $\sim 10\%$ error in the reported thermal conductivity. The transducer thicknesses of the samples studied in this PhD were verified by profilometry, picosecond acoustics, or X-ray reflection (XRR), all of which give an accurate thickness measurement better than ± 3 nm for an 80 nm transducer. The aluminum thickness for the calibration samples was determined by profilometry and XRR. The error bars shown in Fig. 3.3 and tabulated in Table 3.1 are the result of the standard deviation in the measurement and the error due to ± 1 nm in the aluminum thickness.

For typical TDTR measurements where the metal transducer is aluminum and the modulation frequency is ~ 10 MHz, the fluctuation in the lock-in amplifier signal when the pump beam is blocked (sample acting as a mirror) is $\sim 0.1 \mu\text{V}$ for V_{in} and $\sim 0.2 \mu\text{V}$ for V_{out} . When the pump beam is hitting the sample, the signal level at

+1 ps time delay is $\sim 25 - 180 \mu\text{V}$ for V_{in} and $\sim 4 - 10 \mu\text{V}$ for V_{out} depending on the sample properties and the typical pump and probe beam powers absorbed by the sample. These numbers are nearly identical for double color and two-tint. Therefore, both arrangements show a signal to noise ratio of better than 25 and 250 for V_{in} and V_{out} , respectively.

3.8 Summary

In this chapter, I presented the main components of the TDTR system and briefly described the measurement procedure and the difference and similarities between the two-tint and double color arrangements. I derived a general equation for the thermal response of the sample that can be used with any pump-probe system with Gaussian beam geometry. The generalized equation is then used to derive the lock-in amplifier response for our specific pulsed TDTR system by plugging in the Fourier transforms of the time dependent functions of the pump and probe beams.

Chapter 4

Size Effects in Thin Film SiGe

Alloys

“The actual state of our knowledge is always provisional and... there must be, beyond what is actually known, immense new regions to discover.”

–Louis de Broglie

4.1 Background

Silicon-germanium structures continue to be the focus of tremendous investment due to their widespread integration in thermoelectric power generation, optoelectronic devices, and high-mobility transistors. For example, bulk $\text{Si}_{1-x}\text{Ge}_x$ is an established high temperature thermoelectric material demonstrating a figure of merit, ZT , approaching unity at ≈ 1100 K [95]. Moreover, there has been much interest in engineering silicon-germanium systems for high ZT thermoelectric devices by the manipulation of thermal properties via interface scattering effects. For these reasons, the thermal properties of $\text{Si}_{1-x}\text{Ge}_x$ systems have been studied extensively in a variety of material forms including superlattices of different period lengths [96–100], alloy based

superlattices [101, 102], superlattice nanowires [103], doped $\text{Si}_{1-x}\text{Ge}_x$ superlattices and bulk alloys [99, 104, 105], and nanostructured undoped bulk alloys [106]. These investigations have been accompanied with theoretical studies that have elucidated the underlying nature of phonon transport in these systems [104, 107–110]. Most of previous works allude to the fact that $\text{Si}_{1-x}\text{Ge}_x$ -based superlattice structures exhibit thermal conductivities lower than the so called alloy limit. These superlattices are often compared to SiGe alloy samples of much larger thicknesses. This neglects the potential size effects associated with the finite sample thicknesses of alloys and total sample thickness of superlattices, a fact that is often overlooked due to the assumption of strong phonon scattering at alloy sites.

This idea is reinforced by recent computational and theoretical investigations into thermal conductivity of nanostructured $\text{Si}_{1-x}\text{Ge}_x$ systems. For example, when implementing non-equilibrium molecular dynamics (NEMD) simulations, Landry and McGaughey [111] found that the calculated values of thermal conductivity of a $\text{Si}_{0.5}\text{Ge}_{0.5}$ alloy were strongly dependent on the size of simulation cell (more so than in a homogeneous Si domain [112]). Also via NEMD, Chen *et al.* [113] found that the thermal conductivities of Stillinger-Weber type $\text{Si}_{1-x}\text{Ge}_x$ nanowires were substantially below those values obtained by Skye and Schelling [114], where the Green-Kubo approach was used to predict the thermal conductivities of bulk $\text{Si}_{1-x}\text{Ge}_x$ alloys. Finally, Garg *et al.* [115] used density functional perturbation theory to study the spectral dependence of thermal conductivity in bulk $\text{Si}_{1-x}\text{Ge}_x$ alloys and found that more than half of the heat-carrying phonons had mean-free-paths greater than $1\ \mu\text{m}$.

Whereas copious effort has been invested in quantifying the thermal conductivity of more complex nanostructured $\text{Si}_{1-x}\text{Ge}_x$ systems (i.e., superlattices, nanowires, etc.), there are far fewer reports that focused on experimentally investigating $\text{Si}_{1-x}\text{Ge}_x$ thin film alloys thermal transport [96, 100, 116, 117]. In this chapter, I present measurements of the thermal conductivity of thin-film $\text{Si}_{1-x}\text{Ge}_x$ alloys with thicknesses

ranging from 39 to 427 nm along with different alloy compositions over a temperature range of 141 to 300 K via time domain thermoreflectance (TDTR).

4.2 SiGe Alloy Thin Film Samples

Two sample sets, as listed in Table 4.1, were prepared: a thickness series with nominal composition $\text{Si}_{0.8}\text{Ge}_{0.2}$ and a composition series of slightly varying thicknesses. The samples were epitaxially grown using metal-organic chemical vapor deposition (MOCVD) on 100 mm diameter (001)-oriented single-crystalline silicon substrates (purchased from Lawrence Semiconductor). Substrate growth temperatures ranged between 650 and 700 °C. Sample thicknesses were verified by X-ray reflectivity and cross sectional transmission electron microscopy (TEM). Film stoichiometry was verified by Rutherford backscattering spectroscopy. Surface roughnesses were characterized by atomic force microscopy. In general, this level of characterization is necessary to minimize the uncertainty in the analysis of TDTR data. We also assessed the defect densities within the films by TEM. These observations were conducted on plan-view specimens back-thinned from the silicon side by mechanical grinding and dimpling, followed by Ar⁺ ion milling. Figure 4.1 shows TEM images from the plan-view specimens collected from the thickness series of $\text{Si}_{1-x}\text{Ge}_x$ films. As seen in the

Table 4.1: Thickness and alloy composition of SiGe alloy thin film samples.

	Thickness (nm)	Ge Content (%)	κ ($\text{W m}^{-1} \text{K}^{-1}$)
Thickness Series	39 ± 0.9	20.0	1.83 ± 0.09
	88 ± 1.8	20.0	2.17 ± 0.10
	202 ± 2.1	20.0	2.69 ± 0.10
	427 ± 2.1	20.0	2.84 ± 0.18
Composition Series	88 ± 1.8	20.0	2.17 ± 0.10
	135 ± 10.4	34.5	1.68 ± 0.30
	126 ± 10.1	45.0	1.79 ± 0.39

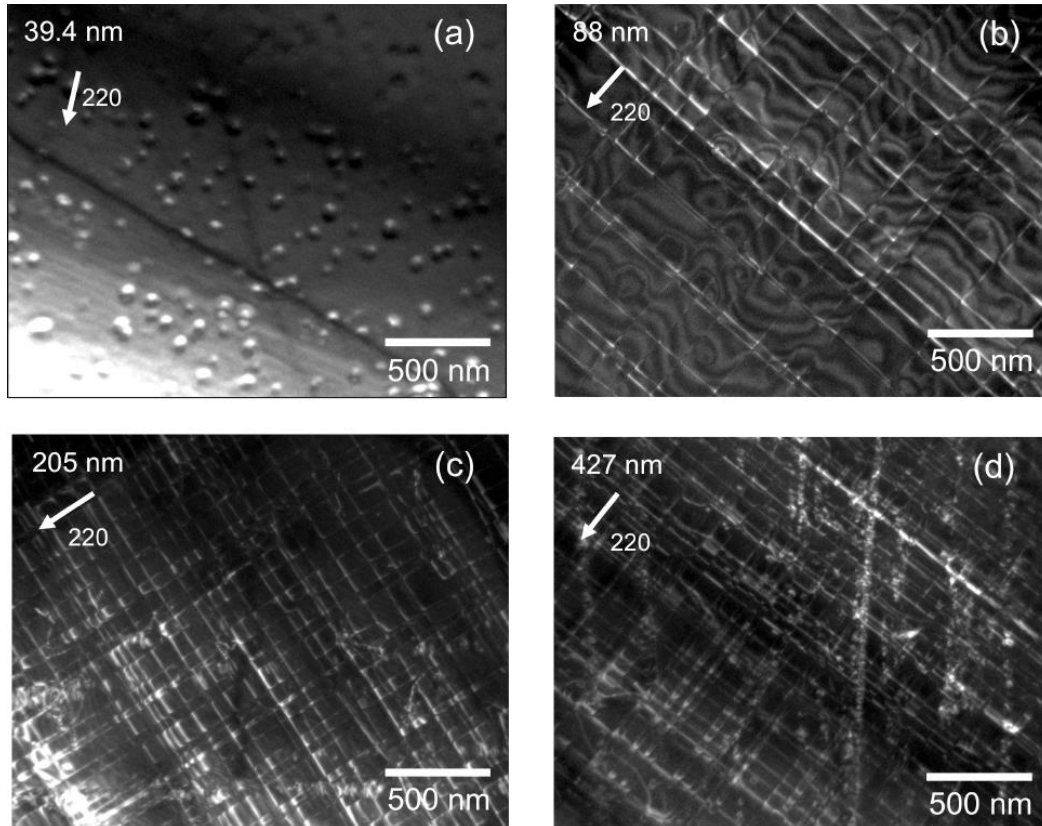


Figure 4.1: Plan view TEM images showing increasing density of dislocations with increasing film thickness. Images were collected under weak-beam dark-field conditions using a $\{220\}$ type diffracting vector.

micrographs, the dislocation density increases with the film thickness. Therefore, if dislocations were to cause a reduction in thermal conductivity, the conductivity of the thickest samples would be the lowest. We will show that this is not the case.

4.3 Thermal Conductivity Measurement Results on SiGe Films

The cross-plane thermal conductivities of the samples is measured by TDTR utilizing the double color pump-probe arrangement. For two selected samples, the temperature dependent thermal conductivities are measured from 141 to 300 K using a liquid nitrogen cryostat with optical access. For TDTR transduction, the $\text{Si}_{1-x}\text{Ge}_x$ samples

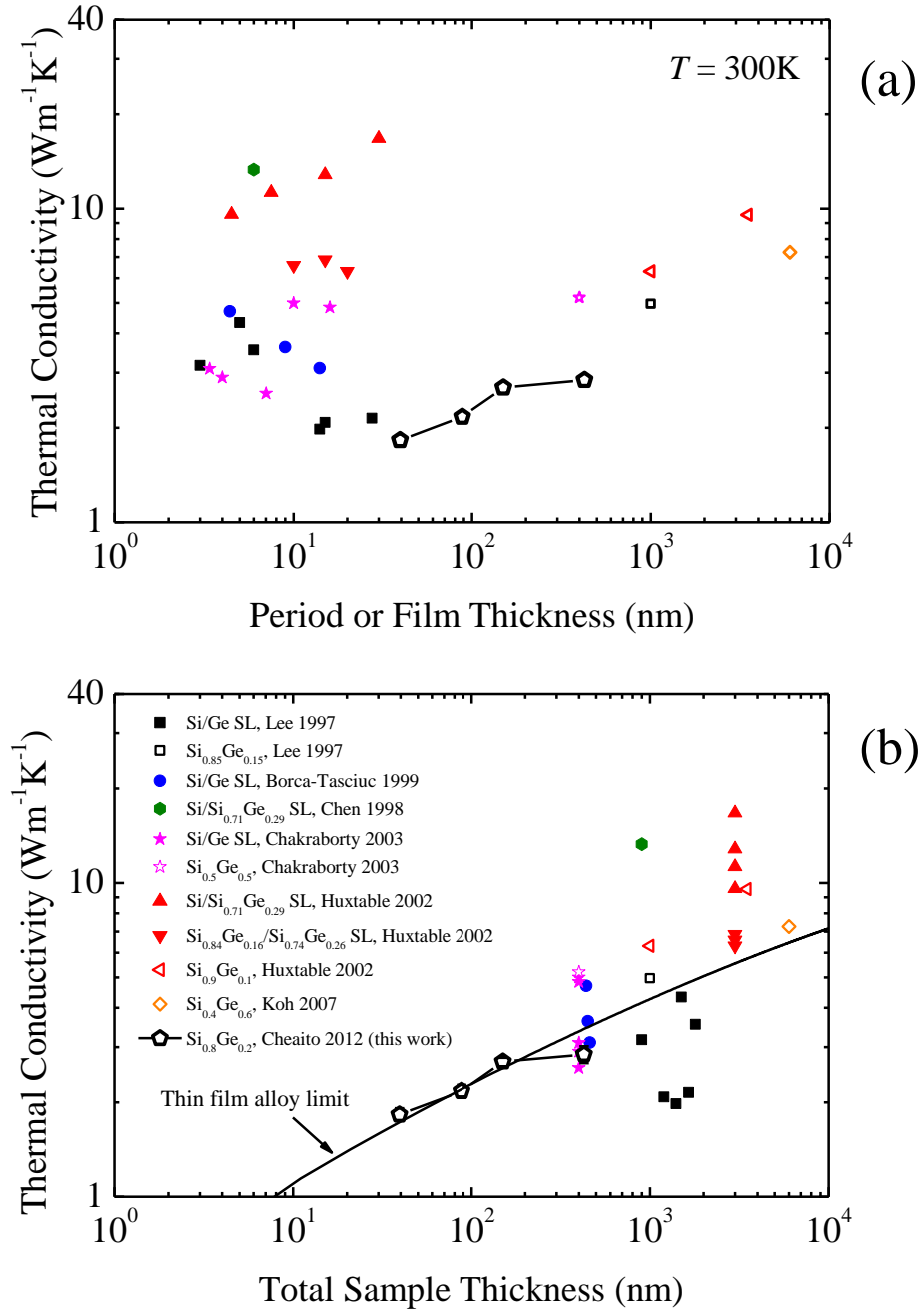


Figure 4.2: Thermal conductivity measurements on $\text{Si}_{0.8}\text{Ge}_{0.2}$ of the thickness series along with previously reported values of different Si/Ge superlattices, alloy based superlattices and alloy films at room temperature. Closed symbols represent superlattices, open symbols represent $\text{Si}_{1-x}\text{Ge}_x$ films. The thermal conductivity is plotted versus (a) period or film thickness, (b) total sample thickness. The solid line represent the model given in Eq. 4.1. Data were taken from Lee *et al.* [96], Borca-Tasciuc *et al.* [99], Chen *et al.* [102], Chakraborty *et al.* [100], Huxtable *et al.* [101], Koh *et al.* [117], and Cheaito *et al.* [21].

were coated with aluminum via e-beam evaporation prior to TDTR testing. The aluminum thickness was locally confirmed by picosecond acoustics [7, 8]. The thermal conductivity of the silicon substrate was measured separately using a reference Si sample from the same lot as the substrate. We assume literature values for Al film and Si substrate heat capacities. Temperature dependent heat capacity values for $\text{Si}_{1-x}\text{Ge}_x$ were taken from Ref. [118]. At least four measurements were taken on each sample at different locations to ensure relative uniformity. Repeats of selected samples were also measured to confirm that the obtained results were not associated with a particular batch of samples. Mean values for the resulting thermal conductivities for each of the films are listed in Table 4.1 and plotted in Figs. 4.2 and 4.3. The uncertainty in thermal conductivity values shown in Table 4.1 accounts for the uncertainty in $\text{Si}_{1-x}\text{Ge}_x$ film thickness, uncertainty in aluminum thickness, and the standard deviation about the mean of the measurements performed on each sample. Figure 4.2(a) compares the measurement results to those acquired on various $\text{Si}_{1-x}\text{Ge}_x$ structures reported previously [96, 98, 100–102, 117]. These values are plotted against either period length, in the case of a superlattice, or thickness in the case of a thin-film alloy. Similarly, in Fig. 4.2(b), the same data is plotted versus the total thickness of the sample for both superlattices and alloy films. A clearer trend in the thermal conductivities is observed when compared against the total sample thickness (Fig. 4.2(b)) as opposed to superlattice period (Fig. 4.2(a)). This suggests that the total film thickness rather than periodicity is inhibiting the thermal transport in both superlattices and alloy films. The measured alloy films show a thermal conductivity three to five times lower than bulk. Since the thermal conductivity increases with thickness, the reduction in the measured thermal conductivity of the sample as compared to bulk can not be attributed to film dislocations. Intriguingly, the thermal conductivities of the alloy thin films measured are among the lowest of any of the previous measurements on SiGe-based thin-film systems. We note that the only previous data that approaches

our lowest measured value is that in which the authors admit that the measured samples have poor crystal quality (black filled squares in Fig. 4.2) [96].

4.4 Analysis

4.4.1 Thermal Model

To quantify size effects from the finite sample thickness, I apply a Debye approximation to the thermal conductivity formula given by Eq. 2.9 where the thermal conductivity is averaged over three phonon branches. The thermal conductivity, κ , is given by:

$$\kappa = \int_0^{\hbar\omega_c/k_B T} \frac{k_B^4 T^3}{2\pi^2 v \hbar^3} \tau(T, y) y^4 \frac{\exp(y)}{[\exp(y) - 1]^2} dy \quad (4.1)$$

where k_B is Boltzmann's constant, \hbar is Planck's constant divided by 2π , T is temperature, and $y = \hbar\omega/k_B T$ is a dimensionless parameter. The average velocity, v , is calculated by $v = ((1-x)v_{\text{Si}}^{-2} + xv_{\text{Ge}}^{-2})^{-1/2}$, where x is the Ge concentration, and v_{Si} and v_{Ge} are the average speeds of sound in Si and Ge, respectively, as calculated by Wang and Mingo [52]. The scattering time for a given frequency, τ , is related to the individual processes via Matthiessen's rule, $\tau = (\tau_U^{-1} + \tau_a^{-1} + \tau_L^{-1})^{-1}$, where τ_U , τ_a , and τ_L are the Umklapp, alloy, and boundary scattering times, respectively. These are given by

$$\tau_U = ((1-x)\tau_{U,\text{Si}}^{-1} + x\tau_{U,\text{Ge}}^{-1})^{-1}, \quad (4.2)$$

$$\tau_a = (x(1-x)A\omega^4)^{-1}, \quad (4.3)$$

and

$$\tau_L = L/v, \quad (4.4)$$

where

$$\tau_{U,\text{Si}(\text{Ge})}^{-1} = B_{\text{Si}(\text{Ge})}\omega^2 T \exp(-C_{\text{Si}(\text{Ge})}/T). \quad (4.5)$$

The constants A , B , and C are taken from Ref. [52], and L is the film thickness.

Our model is thus identical to that in Ref. [52] except for the cutoff frequency, which we define as $\omega_c = 2\pi v/a$, with a being the lattice constant of the $\text{Si}_{1-x}\text{Ge}_x$ film approximated by Vegard's Law: $a = (1-x)a_{\text{Si}} + xa_{\text{Ge}}$, where a_{Si} and a_{Ge} are the lattice constants of silicon and germanium, respectively. Equation 4.1 assumes a dispersionless, Debye system. This is acceptable for $\text{Si}_{1-x}\text{Ge}_x$ systems with non-dilute alloying compositions since the dispersive phonons scatter strongly with the alloy atoms due to their high frequencies. This assertion is substantiated by the reasonable agreement found between this model, our data, and previously reported measurements on thin film alloys in Refs. [96, 101, 117] as shown in Fig. 4.2.

4.4.2 Role of Alloy Composition

To first assess the role of alloy composition, Fig. 4.3 shows the measured thermal conductivity versus Ge concentration and the predictions of the thermal conductivity for bulk and thin film $\text{Si}_{1-x}\text{Ge}_x$ of three different thicknesses at room temperature using Eq. 4.1. For $\text{Si}_{1-x}\text{Ge}_x$ with $0.2 < x < 0.8$ we found that the thermal conductivity is almost flat, and in agreement with our experimental results. This lack of dependence on the Ge concentration is much more pronounced in thin films than in bulk materials, suggesting that size effects more significantly influence the transport in $\text{Si}_{1-x}\text{Ge}_x$ films than does alloying when $0.2 < x < 0.8$. This is further supported in Fig. 4.3 where changes in thickness from 39 to 427 nm are found to have a much greater effect on the thermal conductivity than variations in Ge content. Lastly, this trend is consistent with the previous computational work of Chen *et al.* [113], where the thermal conductivities of Stillinger-Weber type $\text{Si}_{1-x}\text{Ge}_x$ nanowires were relatively insensitive to changes in composition for $0.2 < x < 0.8$.

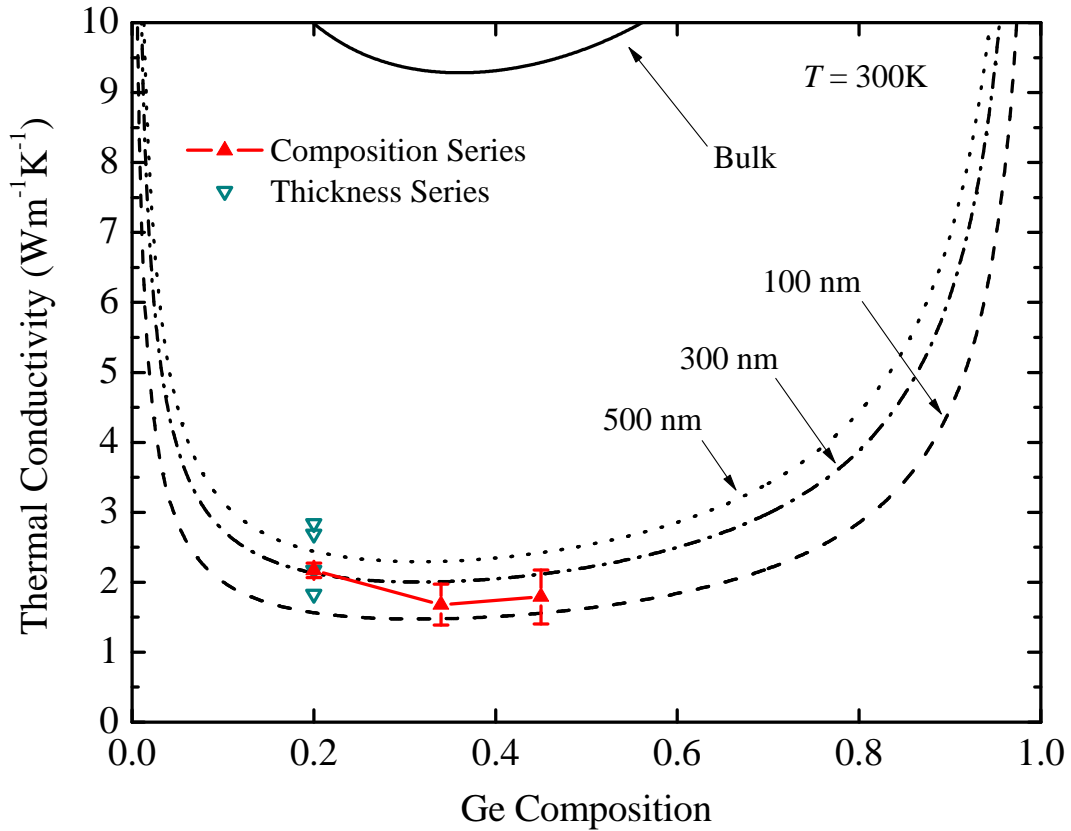


Figure 4.3: Predictions of the thermal conductivity as a function of Ge composition for bulk and thin film $\text{Si}_{1-x}\text{Ge}_x$ of three different thicknesses calculated at room temperature using Eq. 4.1. The symbols correspond to experimental data on thickness series (down open triangles) and composition series (up filled triangles). With decreasing film thickness, alloying induces smaller and smaller changes in the thermal conductivity as size effects begin to dominate.

4.4.3 Spectral Contribution to Thermal Conductivity

To understand the degree to which the different scattering processes affect thermal conductivity, we analyze the spectral contribution to thermal conductivity by calculating the integrand of Eq. 4.1. Figure 4.4(a) shows the spectral thermal conductivity for the 427 nm and 39 nm films having a Ge content of 20%. The spectral curve increases with frequency reaching a peak at around 10 Trad s^{-1} and 18 Trad s^{-1} for the 427 nm and 39 nm films, respectively, and decreases thereafter. This demonstrates

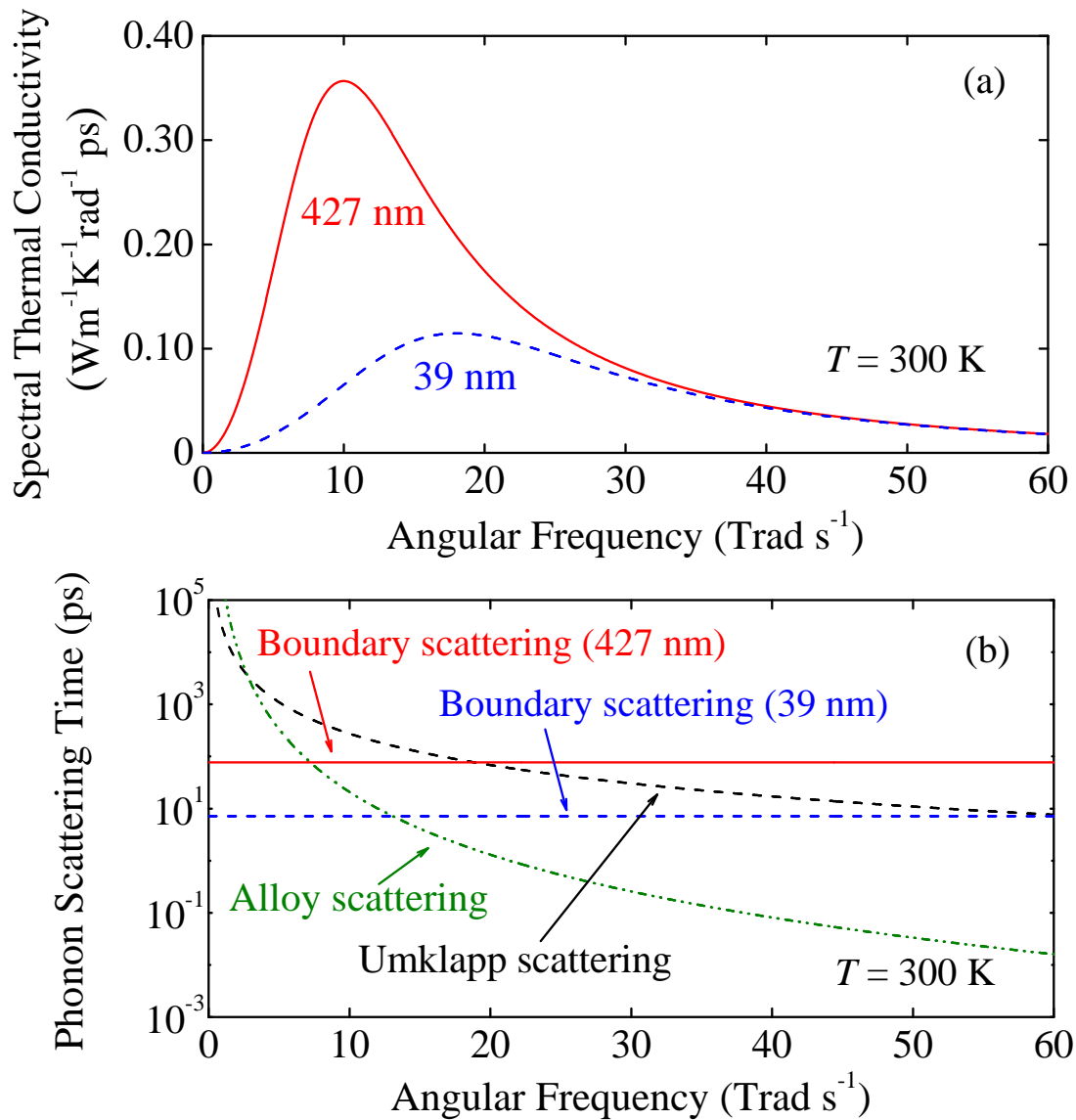


Figure 4.4: (a) Spectral thermal conductivity for the 427 nm and 39 nm $\text{Si}_{0.8}\text{Ge}_{0.2}$ films at room temperature. (b) Alloy, Umklapp, and the boundary scattering times versus angular frequency for the 427 nm and 39 nm films.

that low frequency (long mean free path) phonons more significantly contribute to the transport and thus the treatment of alloys as a dispersionless (i.e., Debye-like) system is valid. Figure 4.4(b) reveals that in this low frequency regime, boundary scattering is the dominant process since the boundary scattering time (τ_L) is shortest for the modes carrying the most heat. It is only at high frequencies that alloy scattering is the limiting mechanism. As a result, we conclude that the low thermal conductivities of $\text{Si}_{1-x}\text{Ge}_x$ alloy thin films arise primarily due to the boundary scattering in the film rather than the effects of the alloying in the material.

4.4.4 Temperature Dependence

The result of the previous section is further demonstrated through an examination of temperature dependence of the thermal conductivity presented in Fig. 4.5. The 427 nm and 202 nm $\text{Si}_{0.8}\text{Ge}_{0.2}$ films exhibit reasonable agreement with our model over a range of 141 to 300 K. We also plot temperature dependent thermal conductivity of a Si/Ge superlattice of 462 nm total thickness from Ref. [98]. Moreover, we plot our model assuming the thickness and average composition of the superlattice in Fig. 4.5. The agreement between the superlattice data, our 427 nm $\text{Si}_{0.8}\text{Ge}_{0.2}$ film, and a $\text{Si}_{0.5}\text{Ge}_{0.5}$ alloy model of the same superlattice total thickness (462 nm) further suggests the existence of similar phonon scattering mechanisms that contribute to the thermal conductivity based on the overall sample size. In addition, we plot the thermal conductivities of amorphous silicon [96], bulk $\text{Si}_{0.8}\text{Ge}_{0.2}$ alloy [96], dilute alloys with 0.13%, 0.25%, and 1.0% Ge compositions [119], and bulk Si [46]. The thermal conductivities of the $\text{Si}_{1-x}\text{Ge}_x$ films and Si/Ge superlattice have similar temperature trends to that of amorphous Si and the bulk $\text{Si}_{1-x}\text{Ge}_x$ alloy, indicating the strong effect of alloy scattering over this temperature range. The reduction of thermal conductivity in the alloy film and superlattice compared to the bulk alloy is attributed to the additional scattering mechanisms of long mean free path phonons with the

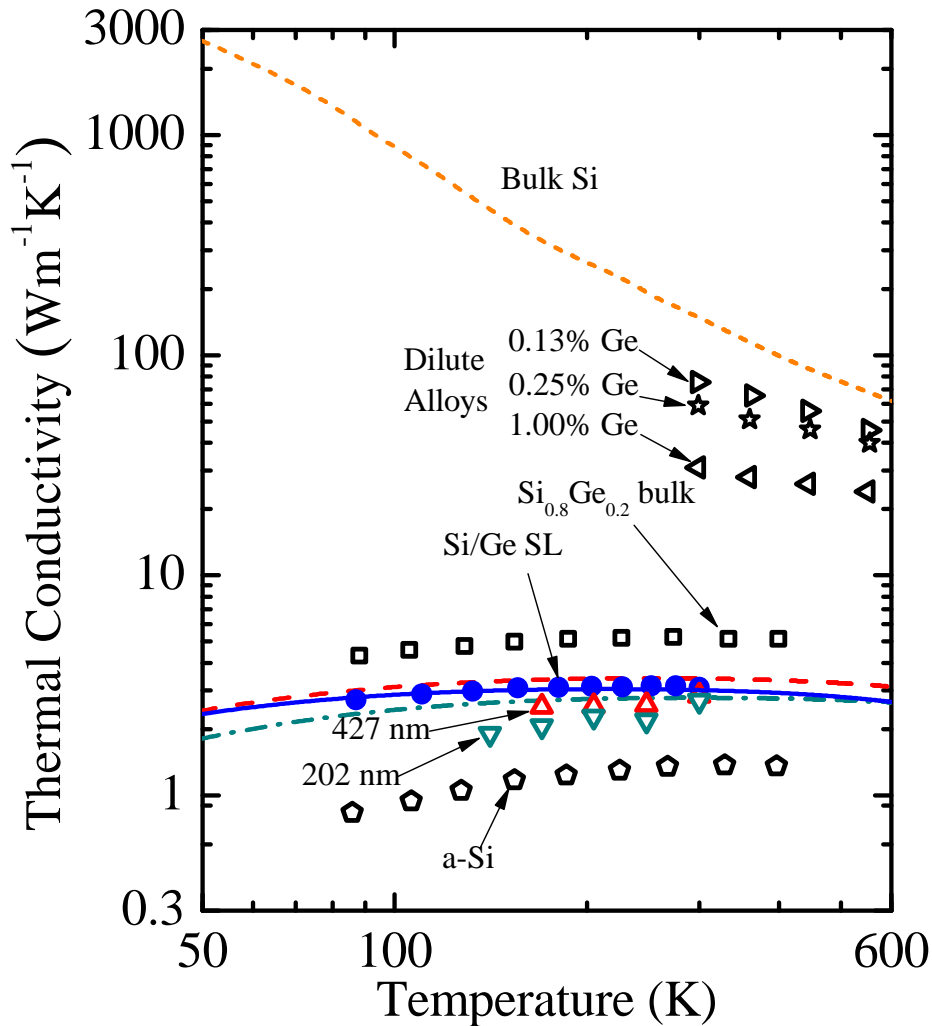


Figure 4.5: Thermal conductivity of various SiGe and Si systems. Symbols represent our data on 427 nm $\text{Si}_{0.8}\text{Ge}_{0.2}$ (up open triangles) and 202 nm $\text{Si}_{0.8}\text{Ge}_{0.2}$ (down open triangles), Si/Ge SL of 14 nm period thickness and 462 nm total thickness (filled circles) from Ref. [98], bulk $\text{Si}_{0.8}\text{Ge}_{0.2}$ (open squares) from Ref. [96], amorphous Si (open pentagons) also from Ref. [96], dilute alloy films of 0.13% (right open triangles), 0.25% (open stars), 1% (left open triangles) Ge concentrations from Ref. [119]. Lines correspond to predictions of the model presented in Eq. 4.1 for 427 nm $\text{Si}_{0.8}\text{Ge}_{0.2}$ film (dashed line), 202 nm $\text{Si}_{0.8}\text{Ge}_{0.2}$ (dash-dot), and 462 nm $\text{Si}_{0.5}\text{Ge}_{0.5}$ (solid line) and bulk Si (dotted line) from Ref. [46].

sample boundaries, as discussed throughout this chapter. In this regime, the thermal conductivities of bulk Si and dilute SiGe alloys show clear trends indicative of Umklapp scattering ($\kappa \propto 1/T$). This Umklapp behavior is absent in non-dilute alloyed systems. This further alludes to the fact that alloy scattering is the dominant high frequency phonon scattering mechanism over this temperature range whereas boundary scattering is affecting the low frequency phonons in these nanosystems. This is further analyzed in our discussion and analysis pertaining to Fig. 4.4.

4.5 The Thin Film Alloy Limit

In the light of the results of this chapter, it is important to define an alloy limit attributed to thin films. As mentioned earlier, the comparison of thermal conductivity of thin film SLs to that of bulk alloys is not an honest comparison because it ignores long range boundary scattering from the finite film thickness. Based on this, several claims of SLs beating the alloy limit found in literature are not sound. Therefore, the model presented in Eq. 4.1 is termed the thin film alloy limit and can be used for comparison of thermal conductivity alloy thin films to other nanostructures.

4.6 More Recent Studies on SiGe

Following the work in this chapter [20], a more recent study by Chen *et al.* [120] reproduced similar results on the thermal conductivity of thin film SiGe alloys. Chen compared Si-Ge SLs to thin film SiGe alloys of the same thickness and showed that the thin film alloy limit can be beaten in non-planar SiGe SLs. Lin and Strachan [40] performed molecular dynamics simulation on Si-Ge SLs and showed a much stronger dependence of the thermal conductivity on the SL sample thickness than on the period thickness, supporting the results in this chapter.

4.7 Summary

In this chapter, I have shown that the reductions of thermal conductivity in silicon-germanium alloy thin films are ascribed to the finite sizes of the samples and the long range boundary scattering. For thin film alloys and superlattices, the boundary conditions of the samples must be considered when comparing the thermal conductivity to the alloy limit. That is, if an honest comparison is to be made between the thermal conductivities of superlattices and alloys, the total sample thickness of each must be considered. The results of this chapter alludes to the importance of a more systematic study to understand the interplay between the effect of period thickness and total sample thickness on the thermal conductivity of superlattices. The thermal conductivity of SLs and the effects of long and short range boundary scatterings are the focus of the next two chapters. The results of this chapter will be reinforced in Chapter 6.

Chapter 5

Phonon Coherence in SrTiO₃-CaTiO₃ Superlattices

“Measure what is measurable, and make measurable what is not so.”

–Galileo Galilei

5.1 Background

The conclusions in Chapter 4 alluded to the importance of a more systematic study to understand the role of short range boundary scattering in thermal transport in SLs. Crystal defects in Si-Ge SLs arising from strain relaxation in relatively thick layers due to the lattice mismatch between Si and Ge ($\sim 4\%$) has plagued the interpretation of most results on Si-Ge SLs (Fig. 4.2). The spread in the literature data on Si-Ge SLs and the variation in the thermal conductivity trend as a function of period thickness elucidate to the need for a better material system to understand the effect of short range boundary scattering on thermal transport in SLs. As pointed out in Chapters 1 and 2, thermal measurements on SLs serve as an unparalleled method to probe the behavior of phonons. Therefore, a high quality material system is a must

to get the most out of any thermal study on SLs.

The analysis given in Chapter 4 treats phonons as a gas of particles with a distribution of energies and mean free paths that can describe the reduction in thermal conductivity upon scattering from sample boundaries. However, phonons can also display wave behavior as discussed in Chapter 2. The localization of phonon waves in SL structures has been the focus of several theoretical studies [34, 37–41]. When phonons behave as waves, they propagate through the SL structure without losing their phase information and “see” the SL as one homogeneous material.

Coherent phonon behavior was first demonstrated experimentally by Venkatasubramanian [36] in 2000, where he showed a minimum in the room temperature lattice thermal conductivity of Bi₂Te₃-Sb₂Te₃ SLs as a function of period thickness. The minimum was explained in terms of coherent backscattering of phonons in short period thickness samples. However, this result remained questionable given that it required subtracting the electron thermal conductivity from the total measured thermal conductivity values, where the electrons contributed up to half the value of total thermal conductivity. Around the same time, Simkin and Mahan [34] demonstrated a minimum in the cross-plane thermal conductivity of SLs by lattice dynamics calculations. Following their work, Daly *et al.* [37] and Imamura *et al.* [38] used molecular dynamics (MD) calculations to show a minimum in the thermal conductivity of AlAs-GaAs SLs, indicative of a cross over from wave-like to particle-like behavior of phonons. Their work emphasized that a small deviation from perfect interfaces can destroy the phonon coherence. Chen *et al.* [39] used MD on solid argon SLs to demonstrate that the minimum in thermal conductivity becomes shallower at higher temperatures due to decoherence effects by increased anharmonic scattering rates at higher temperatures. More recently, Lin and Strachan [40], also used MD to demonstrate phonon coherence in Si-Ge SLs. Their results showed that a minimum in the thermal conductivity of Si-Ge SLs occurs at a period thickness of ~ 9 nm. Garg and Chen [41]

used density-functional perturbation theory to demonstrate the existence of a minimum in thermal conductivity of Si-Ge SLs at a period thickness of ~ 3.3 nm. Their calculations accounted for anharmonicity and interfacial disorder.

Clearly, most of the work in the literature has focused on theoretical or computational studies, and an unambiguous experimental demonstration of phonon coherence is missing. An important realization of previous studies is that a small deviation from perfect interfaces can lead to decoherence effects. In addition, the contribution of electrons to thermal transport can obstruct the possibility of detecting coherent phonon transport in SLs.

In this chapter we study thermal transport in high quality insulating strontium titanate - calcium titanate (SrTiO_3 - CaTiO_3 or STO - CTO) SLs by systematically changing the period thickness while keeping the sample thickness fixed. In doing so, we assess the effect of short range boundary scattering as well as show that phonon behavior might deviate from the classical picture used to explain the results in the previous chapter and demonstrate coherent wave effects.

5.2 STO-CTO SLs Samples: Growth and Characterization

Epitaxial superlattices of $(\text{SrTiO}_3)_m$ - $(\text{CaTiO}_3)_n$ (notation: $m \times n$ where m and n refer to the thickness, in unit cells, of the (001) pc-oriented (pseudo-cubic) STO and CTO perovskite layers, respectively) were grown using reflection high-energy electron diffraction (RHEED)-assisted laser molecular beam epitaxy (MBE) and conventional reactive MBE techniques on (001) pc-oriented single-crystal NdGaO_3 (NGO) substrates. These samples were grown by our collaborators at the University of California, Berkeley in Professor Ramamoorthy Ramesh's laboratory. The thickness of each layer in a period was adjusted to vary the interface density, but keep the volume fraction of the constituents to 50:50 and total thickness of all samples to 200 nm. The superlattice period thicknesses were varied between ~ 0.77 and 67 nm or, equivalently,

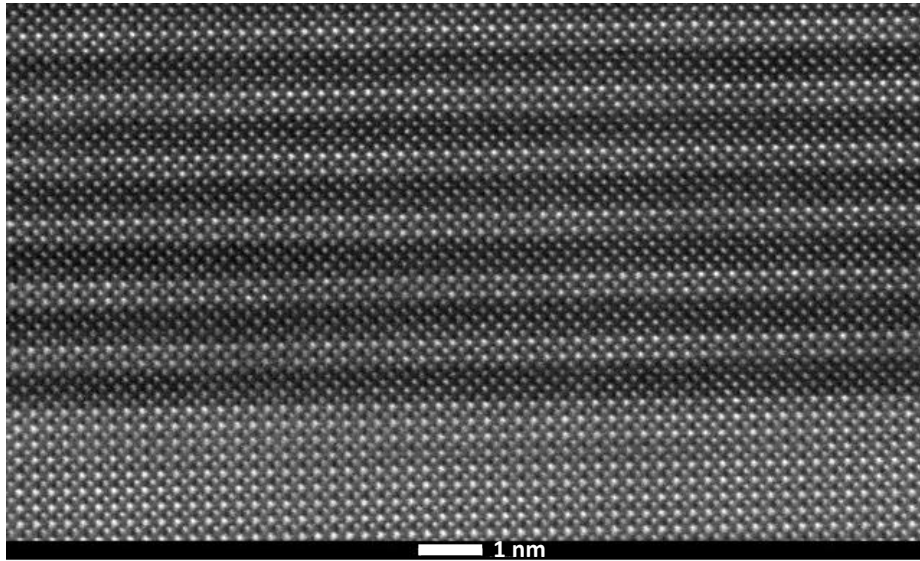


Figure 5.1: TEM image of (SrTiO₃)₂-(CaTiO₃)₂ showing sharp interfaces

to span interface densities from 0.025 to 2.59 nm⁻¹. Therefore, the thinnest period thickness sample corresponds to one unit cell of STO and one unit cell of CTO.

For the laser-MBE technique, the targets used for the growth were single crystalline STO and sintered, polycrystalline CTO. The growth temperature was set to 700°C to ensure stoichiometric transfer of both CTO and STO. The growth pressure employed was 50 mTorr with a laser fluence of 1.5 J cm⁻². After the growth, the samples were cooled to room temperature in 50 Torr of oxygen partial pressure to ensure oxygen stoichiometry of the samples.

The reactive MBE technique enables the growth of superlattice with atomic layer precision through the use of in situ monitoring of RHEED oscillations. Superlattices were fabricated by supplying the substrate with precise single monolayer doses of CaO, SrO, and TiO₂ in the layer order of the desired superlattice at a substrate temperature of 650 °C in a background pressure of 5×10⁻⁷ Torr of molecular oxygen. In terms of the number on unit cells of STO and CTO, m and n , the samples grown by both techniques are namely: 1×1, 2×2, 3×3, 4×4, 6×6, 9×9, 29×28, and 87×87.

All samples were coated with ~ 80 nm of aluminum for TDTR measurements. The thickness of aluminum was confirmed by picosecond acoustics.

An extensive characterization was done on each sample to ensure that any observed trend in thermal conductivity (the minimum in our case) is not a result of poor sample quality. Film quality for both growth techniques was characterized by x-ray diffraction (XRD), atomic force microscopy (AFM), and transmission electron microscopy (TEM). The details of all these characterizations are given in the Supplementary Materials of Ref. [21]. Here we only show the TEM image on the 2×2 sample in Fig. 5.1. Figure 5.1 shows cross-sectional scanning TEM (STEM) analysis of the 2×2 superlattice. The image clearly shows that the interfaces obtained by the laser MBE growth technique are extremely sharp with little or no inter-diffusion of species across the interfaces.

5.3 Thermal Conductivity Measurements and Sensitivity Analysis

Thermal conductivity measurements in the cross-plane direction are shown in Fig 5.3 for sample temperatures of 84, 142, and 307 K plotted versus period thickness, d_{SL} . We perform 4-5 measurements on each sample at different locations. We assume literature values for the heat capacity and thermal conductivity of the Al film [46] and the heat capacity of the NGO substrate [121]. We treat the SL film as one layer of weighted average of the bulk heat capacity values of CTO [122] and STO [123] for the STO-CTO SL. The thermal conductivity of the NGO substrate is measured separately using a reference NGO sample from the same lot as the substrate on which the samples were grown. Hence the only unknowns in our thermal model are the Al/SL Kapitza conductance, h_1 , the thermal conductivity of the SL film, κ , and SL/NGO Kapitza conductance, h_2 . The thermal penetration depth is estimated to

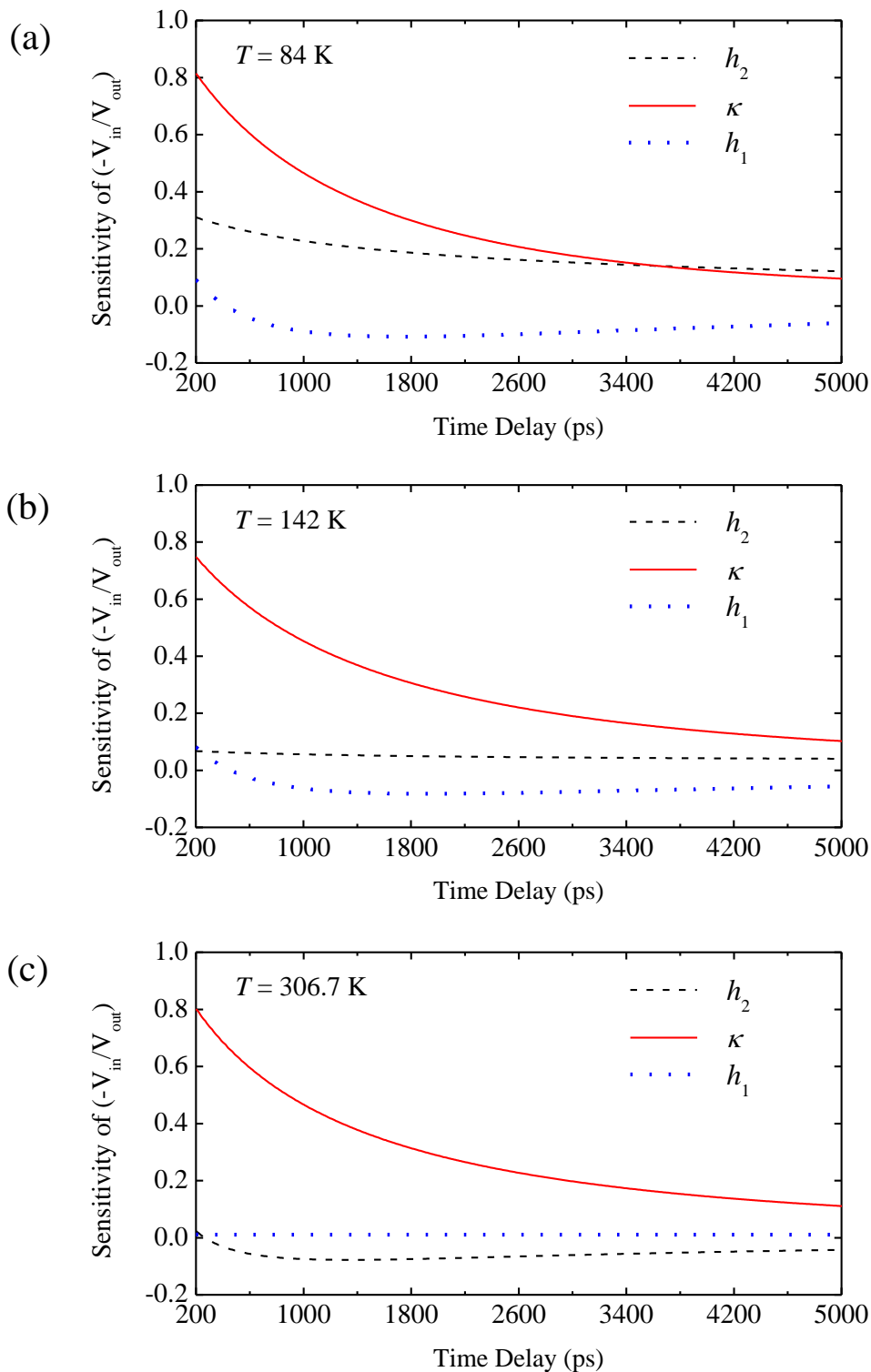


Figure 5.2: TDTR measurement sensitivity of the ratio $(-V_{in}/V_{out})$ to Al/STO-CTO thermal boundary conductance, h_1 , STO-CTO thermal conductivity, κ , and STO-CTO/NGO thermal interface conductance, h_2 at sample temperatures of (a) 84 K, (b) 142 K and (c) 306.7 K.

be between ~ 200 and 630 nm for temperatures in the range $80 - 300$ K. As a result we expect that h_2 will have a great effect at low temperatures given that all samples had a thickness of 200 nm.

Figure 5.2 shows the sensitivity of the ratio to h_1 , κ , and h_2 for the temperatures 84 K, 142 K and 306.7 K. These sensitivities were computed for typical experimental conditions and assuming reasonable values for the layers thermal conductivities and heat capacities and the interface conductances between layers. The figure shows that at 84 K, the sensitivity to h_2 is significant whereas at 142 K the sensitivity to h_1 and h_2 becomes negligible compared to the sensitivity to κ . As a result, for low temperatures, we perform the measurement at two other low frequencies, 1.5 MHz and 3.5 MHz in addition to the 11.4 MHz. Performing the measurement at 3 different frequencies allows us to estimate the value of h_2 . We manually adjust h_2 so that the best fits of the three different measurements yield the same values for h_1 and κ where h_1 and κ are treated as free parameters and are varied to fit the data to the thermal model given in Chapter 3. We found that at 84 K, $h_2 \approx 30 - 40$ MW m⁻² K⁻¹ and at 110 K $h_2 \approx 40 - 50$ MW m⁻² K⁻¹. Values higher than 60 MW m⁻² K⁻¹ at higher temperatures will make the sensitivity to h_2 negligible compared to κ .

5.4 Minimum in Thermal Conductivity

The measurement results plotted in Fig. 5.3 can be clearly divided into two regimes based on whether the thermal conductivity decreases (coherent) or increases (incoherent) with increasing period thickness. The observed minimum in thermal conductivity is interpreted as a crossover from coherent (wave-like) transport at short period thicknesses to incoherent (particle-like) transport at large period thicknesses. In the coherent regime, the phonon coherence length, l_c , is comparable to the SL period thickness [21, 42] and phonon wavepackets spatially extend over multiple SL periods. These wavepackets “see” the SL as a homogeneous material without losing their

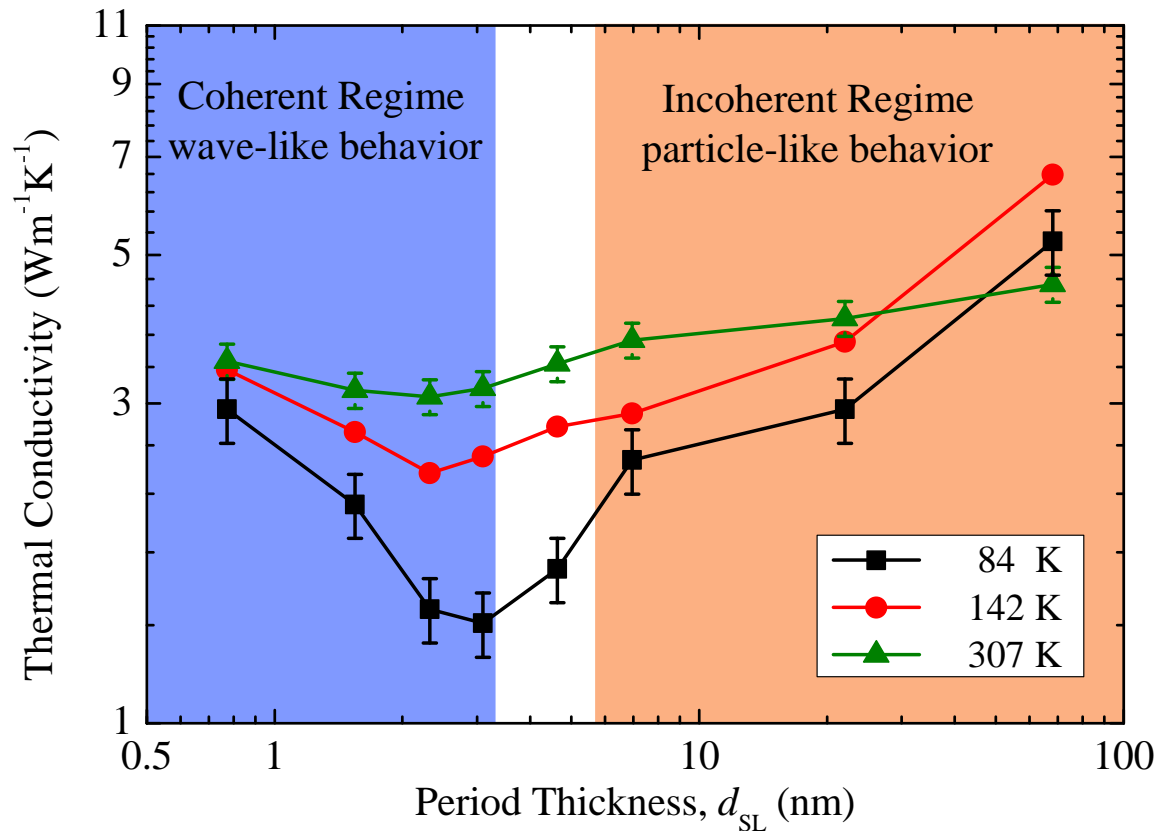


Figure 5.3: Measured thermal conductivity values for $(SrTiO_3)_n-(CaTiO_3)_n$ superlattices as a function of period thickness at different temperatures. The error bars include contributions from the standard deviation in the TDTR measurement and the uncertainty in the Al thickness.

phase information at the superlattice interfaces. In this regime, the increase in period thickness introduces bandgaps into the dispersion curve that cause a reduction in the overall phonon group velocity of high frequency phonons leading to the reduction in the SL thermal conductivity [34], as discussed in Section 2.2.3. The crossover to the incoherent regime occurs when d_{SL} surpasses l_c . In this case, phonons act as particles and experience a finite temperature drop at the SL interfaces leading to the increase in thermal conductivity at longer period thicknesses (lower interface densities). In this regime, phonons act incoherently and are no longer affected by the formation of minibands in the dispersion curve as the period thickness increases. The dominant

mean free path, ℓ , should be larger than d_{SL} in order to observe the monotonic increase in thermal conductivity. This increase is a result of the diminished effect of short range boundary scattering; as the period thickness increases, phonons scatter less frequently at the internal interfaces.

It is important to note that when we talk about a coherent regime, we mean that coherent phonons are the dominant phonons in this regime. Similarly for the incoherent regime. In fact, in both the coherent and incoherent regimes, there exist coherent and incoherent phonons at the same time. The designation is meant to describe the dominant class of phonons in the considered regime.

Two additional observations can be seen in Fig. 5.3. First, the depth of the minimum increases with decreasing temperature, and second, the period thickness at the minimum shifts to higher values at lower temperatures. Both of these trends are consistent with the zone-folded mini-band formation description [34, 39] discussed in Section 2.2.3. The temperature window in which the minimum can be observed is limited. If the temperature is too high, Umklapp processes will dominate and limit the observation of such coherent behavior as discussed in Section 2.3.5; at too low temperatures the high-frequency phonon modes (that are the portion of the spectrum that is mostly affected by the miniband formation in dispersion curve) may not be populated or may carry insufficient heat to show a very pronounced minimum. The observation of a minimum over a temperature range with a clear trend further corroborates our conclusion of the observation of coherent wave transport at short period thicknesses (high interface densities) in these superlattices.

Figure 5.4 shows all the thermal conductivity measurements taken on the eight superlattice samples as a function of temperature. The superlattice with the largest period shows a clear maximum, indicative of 3-phonon processes dominating thermal transport at elevated temperatures. We observe an inflection from decreasing thermal conductivity with decreasing period to increasing thermal conductivity with

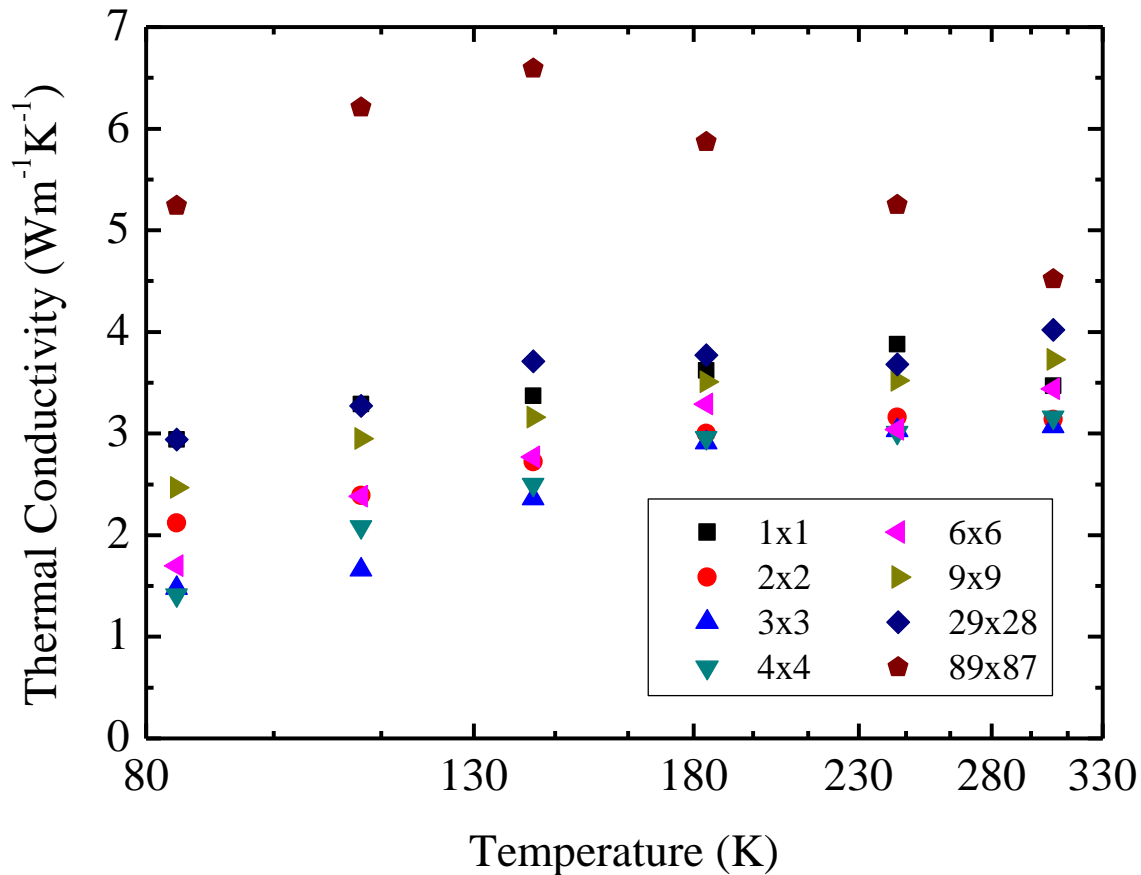


Figure 5.4: Measured thermal conductivity values for $(\text{SrTiO}_3)_n\text{-(CaTiO}_3)_n$ superlattices as a function of temperature. The uncertainty in these measurements (not shown) is similar to that shown in Fig. 5.3.

decreasing period that is observable across the entire temperature range, with the inflection around the 3×3 and 4×4 samples. The increase after this inflection is much more apparent at lower temperatures, which is indicative of the increase in the coherent effect at lower temperatures. Most of the superlattices exhibit an increasing thermal conductivity with increasing temperature (except for the 87×89 sample which exhibits a trend indicative of Umklapp scattering). The 1×1 superlattice, has nearly equivalent thermal conductivities to the 28×29 superlattices. This is because coherent phonon transport was causing the CTO and STO phonons in the 1×1 sample to behave like a new crystal where thermal transport is not limited by short range boundary scattering at a length scale of the lattice constant. This provides

further evidence of our observation of the wave-like behavior of phonon transport in our superlattices.

5.5 More Recent Studies on Phonon Coherence

Following the work in this chapter [21], a few research papers came to support the results. Latour *et al.* [42] demonstrated phonon coherence by equilibrium molecular dynamics in silicon - heavy silicon SLs. They showed that the coherence length depends on the superlattice thickness. Mu *et al.* [43] performed large scale molecular dynamics simulations to show a minimum in thermal conductivity of ^{12}C - ^{13}C superlattices. They also found that the thermal conductivity of these SLs depends on the sample size which indicates that coherent phonon waves propagate ballistically before they scatter at the sample boundary. Zhu and Ertekin [124] also utilized molecular dynamics simulation to demonstrate a minimum in thermal conductivity in two dimensional graphene/boron nitride SLs. They also assessed the effect of interfacial defects and imperfect periodicity on the minimum in thermal conductivity and concluded that defects and randomization can cause the lattice thermal conductivity to appear to increase monotonically masking the minimum.

The fact that more recent studies are all computational illustrates how hard it is to experimentally detect the minimum in thermal conductivity.

5.6 Summary

In this chapter, I showed the first unambiguous experimental evidence for the crossover from coherent to incoherent transport in SLs. This crossover has been studied theoretically and computationally for the past 15 years with no clear experimental evidence of its existence. In STO-CTO SLs, phonons exhibit wave-like behavior at short period thickness and propagate as coherent waves across the SL

interfaces. In this regime, the thermal conductivity decreases due to the mini-band formation in the phonon dispersion curve to reach a minimum around the 3×3 and 4×4 period samples. The thermal conductivity increases thereafter when transport becomes incoherent and phonons experience finite temperature drops at the interfaces. In this regime, the increase in thermal conductivity with period thickness is due to the reduced effects of short range boundary scattering.

Chapter 6

Size Effects in AlAs-GaAs

Superlattices

“There are two possible outcomes: if the result confirms the hypothesis, then you’ve made a measurement. If the result is contrary to the hypothesis, then you’ve made a discovery.”

–Enrico Fermi

6.1 Background

The results of Chapter 5 illustrated how periodicity affects the thermal conductivity of SLs. Given that the STO-CTO samples studied were all of the same thickness (200 nm), these results do not explain the interplay between short and long range boundary scattering in SLs, a question that was posed following the results of Chapter 4. To understand the effect of long range boundary scattering, SLs with large thicknesses should be considered. The small lattice mismatch between AlAs and GaAs ($< 0.2\%$) and the improvements in thin film synthesis techniques allow for the fabrication of high quality SLs with thicknesses spanning 3-4 orders of magnitude.

AlAs-GaAs SLs have been extensively studied due to their applications in opto-

electronic devices [18]. Discrepancies in the thermal conductivity values and trends also exist in thermal studies on AlAs-GaAs SLs (though these discrepancies are not as pronounced as those observed in Si-Ge based material systems, possibly due to lower lattice mismatch and higher overall samples quality). Figure 6.1 summarizes the main thermal conductivity results in the literature plotted versus temperature in (a) and versus film thickness in (b). Values show a great reduction in thermal conductivity of SLs compared to that of bulk GaAs ($51 \text{ Wm}^{-1}\text{K}^{-1}$) and bulk AlAs ($90 \text{ Wm}^{-1}\text{K}^{-1}$), along with varying temperature trends. Contrary to the trend seen by Luckyanova *et al.* [22], Yu *et al.* [125] and Capinski *et al.* [87] report a reduction in thermal conductivity with the increase in temperature. This was explained in terms of Umklapp scattering or interfacial scattering due to roughness at the SL internal interfaces. Moreover, thermal conductivity data in Fig. 6.1(b) show that no conclusive result can be drawn on the interplay between period thickness and sample thickness. In all of the previous studies on thermal conductivity of AlAs-GaAs, sample thicknesses were not constant but spanned three orders of magnitude from 24 nm for the thinnest sample measured by Luckyanova *et al.* [22] up to $10 \mu\text{m}$ for the samples studied by Yao [126] and Yu *et al.* [125]. In addition, samples measured by Capinski *et al.* [87] were of different sample and period thicknesses. These thickness variations complicate the analysis and prevent a unifying understanding of the heat transport mechanisms in superlattices.

In this Chapter, I present thermal conductivity measurements of three sets of AlAs-GaAs SLs of period thicknesses of 2, 12, and 24 nm and sample thicknesses ranging from 21.6 to 2,160 nm. All SL samples had a volume fraction of 50:50. This large set of samples allows to systematically vary d_{SL} and L values to construct a $d_{\text{SL}} - L$ mesh over which the thermal conductivity, κ_{SL} , is measured. This systematic variation of d_{SL} and L is the “*missing ingredient*” for understanding the interplay between short and long range boundary scattering effects on the thermal conductivity. In the

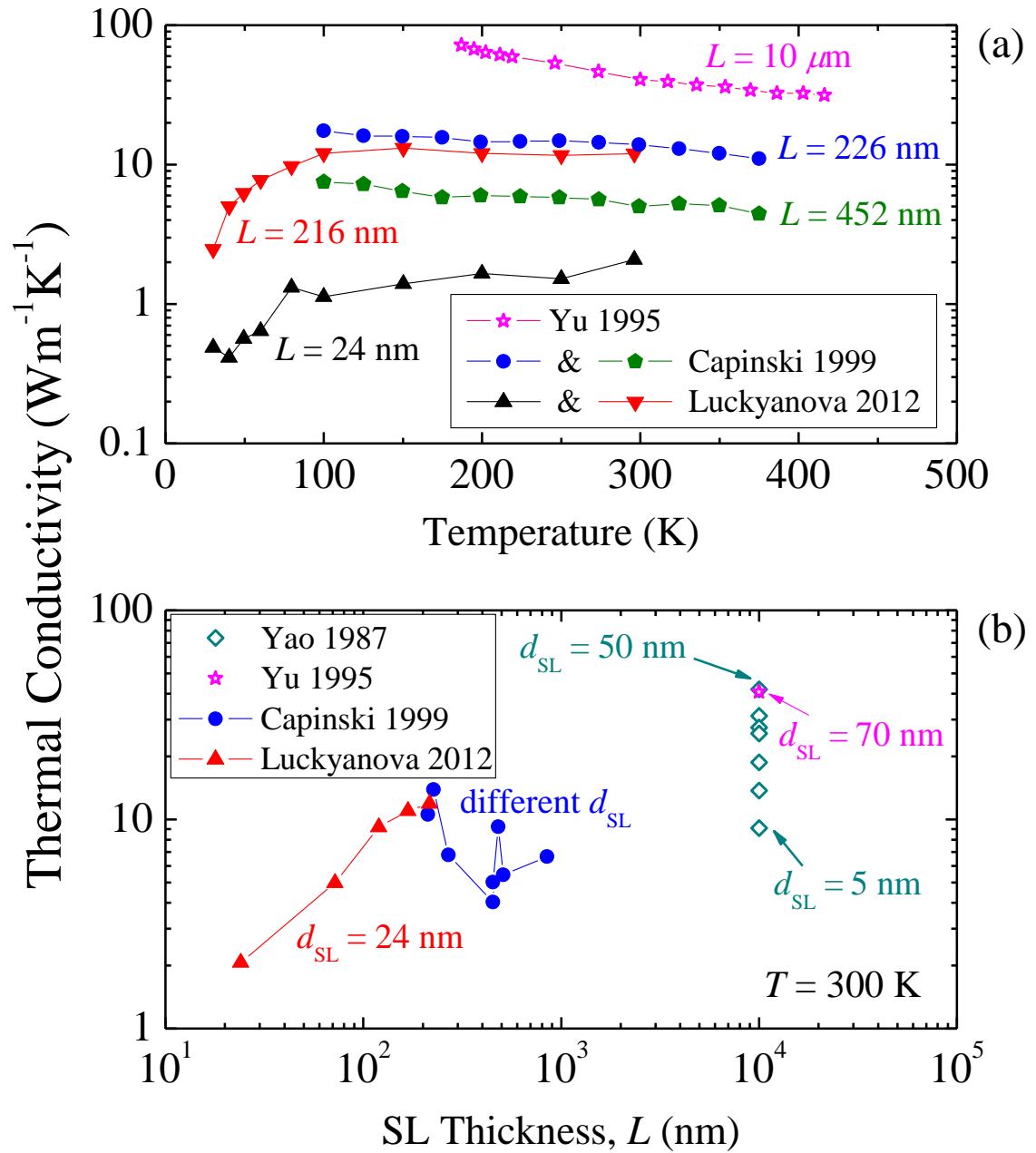


Figure 6.1: Thermal conductivity values for AlAs-GaAs superlattices as a function of (a) sample thickness and (b) temperature. Data were taken from Yao *et al.* [126], Yu [125], Capinski *et al.* [66], and Luckyanova *et al.* [22].

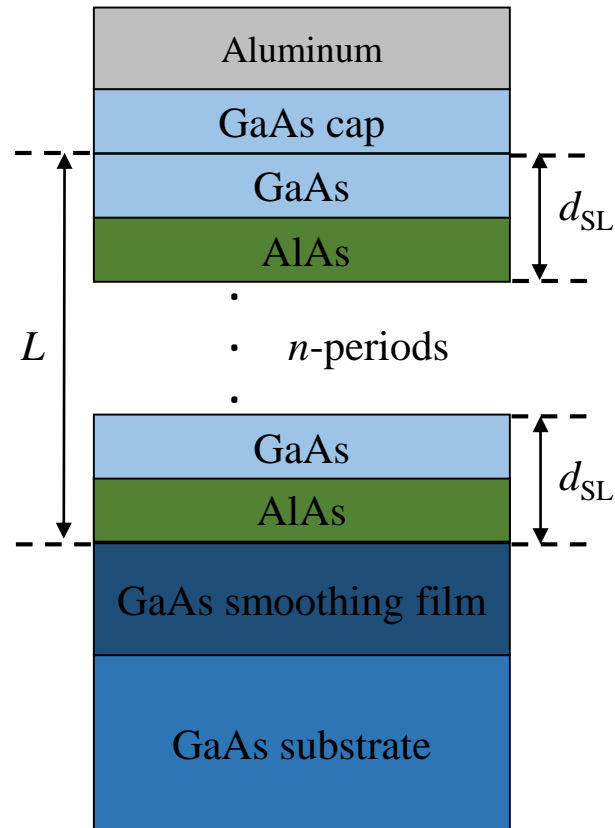


Figure 6.2: A schematic showing the AlAs-GaAs SLs structure. For the 2 nm period thickness set, a 5 nm GaAs cap layer was grown on top to prevent oxidation of Al inside AlAs prior to coating the samples with aluminum.

light of the thermal conductivity measurements, I discuss the two approaches (κ_{\min} and κ_{ball}) for demonstrating phonon coherence and show that they are describing two fundamentally *different* physical phenomena. The concept of phonon coherence is reinterpreted accordingly.

6.2 Sample Growth

Samples were grown on (001) GaAs substrates by molecular beam epitaxy (MBE) by collaborators at the University of New Mexico, Professor Ganesh Balakrishnan's group. Prior to growth, the native oxide on the substrates is desorbed at 630°C for

Table 6.1: period thickness, d_{SL} , thickness, L , smoothing layer thickness, d_{smooth} , cap layer thickness, d_{cap} , and thermal conductivity of AlAs-GaAs superlattice films.

Sample Code	d_{SL} (nm)	L (nm)	d_{smooth} (nm)	d_{cap}	$\kappa_{300\text{K}}$ ($\text{W m}^{-1} \text{K}^{-1}$)
R13-20	2	21.6	250	5	1.65 ± 0.33
R13-25	2	38.4	250	5	1.77 ± 0.25
R13-24	2	68.3	250	5	2.34 ± 0.22
R13-21	2	121.5	250	5	3.00 ± 0.22
R13-27	2	384	250	5	3.47 ± 0.24
R13-22	2	683	250	5	3.14 ± 0.40
R13-23	2	1,215	250	5	3.40 ± 0.36
R13-26	2	2,160	250	5	4.17 ± 0.30
R14-125	12	24	200	-	1.97 ± 0.27
R14-126	12	72	200	-	4.32 ± 0.57
R14-127	12	132	200	-	5.68 ± 0.31
R14-128	12	216	200	-	7.46 ± 0.47
R14-129	12	684	200	-	8.90 ± 0.75
R13-111	12	2,160	30	-	8.54 ± 0.69
R14-121	24	21.6	200	-	2.30 ± 0.48
R14-122	24	68.3	200	-	5.75 ± 0.95
R14-123	24	216	200	-	10.63 ± 0.85
R14-124	24	683	200	-	12.69 ± 0.50
R13-109	24	2,160	30	-	11.8 ± 1.03
R13-112	6.0	2,160	30	-	6.68 ± 0.56
R13-110	18.0	2,160	30	-	11.29 ± 0.95

20 minutes. The substrate temperature is then brought down to 580°C and GaAs smoothing layer of thickness d_{smooth} is grown. Following this, with an As overpressure, the Al and Ga shutters are alternated based on the period thickness for the growth of the superlattice at 580°C . The AlAs and GaAs growth rates are monitored by RHEED oscillations and are kept constant at 0.3ML/sec. A V/III ratio of 13 is maintained between As and Ga across the samples as measured by an ionization gauge. Figure 6.2 shows the structure of the grown films. Table 6.1 lists all the measured samples along with their structural parameters. For the 2 nm set of samples, a 5 nm of GaAs cap layer is grown on top to prevent oxidation of Al inside AlAs prior to evaporating 80

nm of Al coating for TDTR measurements.

Using similar growth conditions, six samples of thin GaAs films of thicknesses between 24 and 2,160 nm were grown on GaAs substrate. These samples are used to compare transport in SLs to that in films without internal interfaces. GaAs samples were also coated with ~ 80 nm of Al for TDTR measurements.

6.3 Thermal Conductivity Results and Phonon Coherence

Thermal conductivity measurements in the cross-plane direction were performed over a period of two years. Both the double-color and two-tint arrangements of TDTR were utilized. The thermal conductivity of the substrate and the smoothing layer were measured separately from an identical GaAs substrate and 200 nm GaAs film grown under the same conditions used for the SL films. The values for these conductivities are substituted into the thermal model used to fit the thermal conductivity of the SL films. Measurements were done at three different modulation frequencies, 3.5 MHz, 8.8 MHz, and 12.2 MHz. Similar to the analysis of the STO-CTO data in Chapter 5, using different frequencies allow for estimating the Kapitza conductance between the SL sample and the smoothing layer. Measurements showed that this value is high enough so we are completely insensitive to it. This result is emphasized in Section 6.4.

For the sake of the discussion in this chapter, and for convenience, the schematic representations of the two approaches for demonstrating phonon coherence from Figs. 2.3(a) and 2.3(b) are replotted in Figs. 6.3(a) and 6.3(b). Thermal conductivities of each of the three period thickness sets, plotted in Fig. 6.3(c) and listed in Table 6.1, show that κ_{SL} increases linearly with L and then plateaus for a thickness higher than $\sim 100 - 200$ nm. This increase is a result of the reduced effects of long range boundary scattering at larger film thicknesses, similar to the trend observed in Chapter 4 on thin film SiGe alloys. The relatively constant thermal conductivity

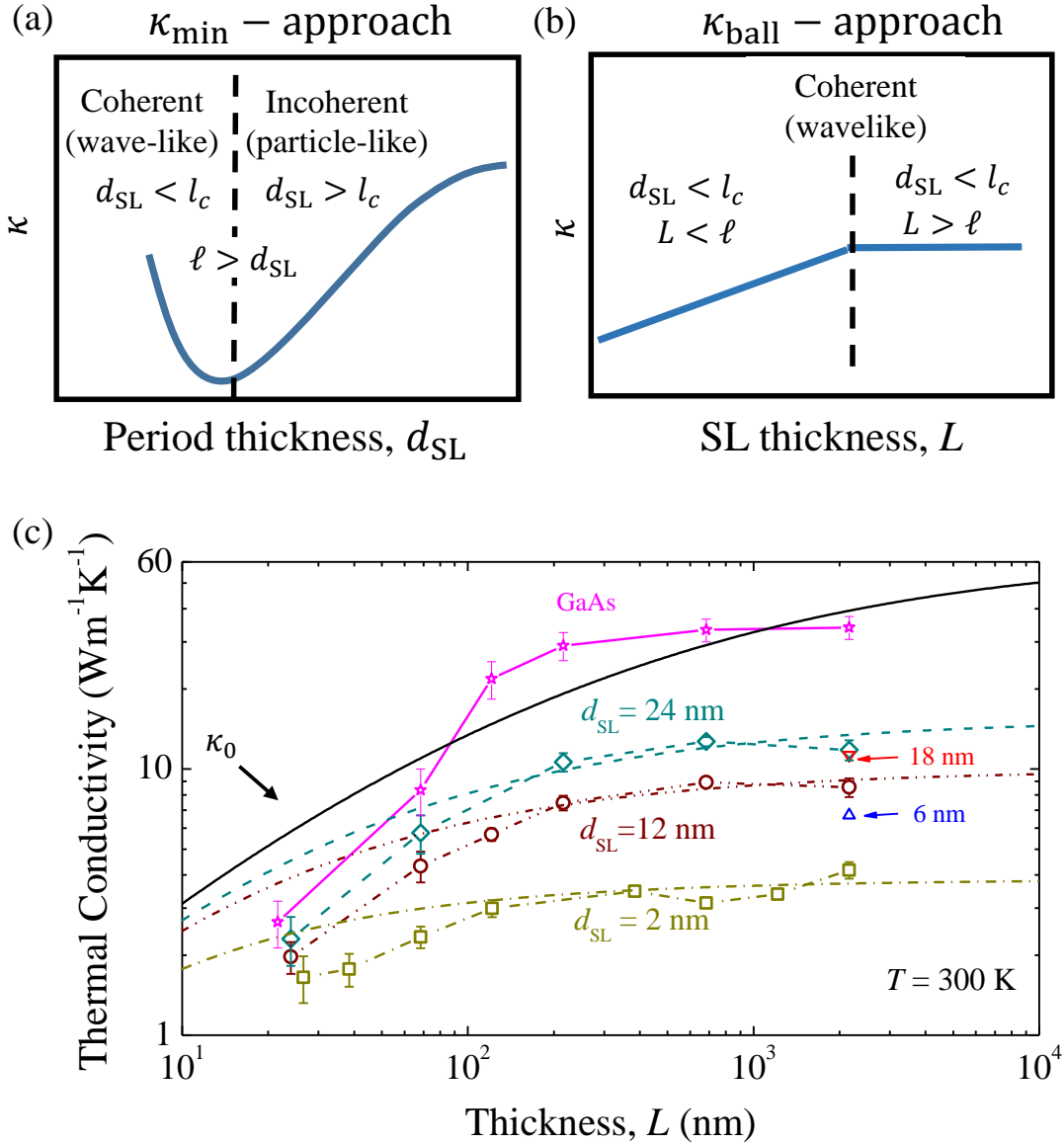


Figure 6.3: (a) κ_{\min} -approach and (b) κ_{ball} -approach for demonstrating phonon coherence in SLs. (c) Thermal conductivity measurements on three sets of AlAs-GaAs SLs of 2, 12, and 24 nm period thicknesses plotted versus the SL thickness at room temperature. Additionally, the plot shows data on two samples with 6 and 18 nm period thicknesses and 2,160 nm thickness and data on a set of six GaAs thin films. The lines represent the model calculation given by equation 6.1. The error bars include contributions from the uncertainty in the aluminum thickness and the standard deviation of the TDTR measurement. The solid line shows the thermal conductivity without the resistance from the interfaces, κ_0 , according to equation 6.1.

for $L > 200$ nm suggests that the dominant phonon mean free path (mfp) is less than L and phonons are scattering within the SL instead of the SL-substrate interface. With respect to d_{SL} , the thermal conductivity increase monotonically with the increase in period thickness. This increase is due to the diminished effects of short range boundary scattering at lower interface densities similar to the trend observed in the Chapter 5 in the incoherent regime of thermal transport across SrTiO₃-CaTiO₃ SLs.

While our results for each period thickness support the κ_{ball} -approach for phonon coherence, the increase in κ_{SL} with d_{SL} places our data in the incoherent regime of the κ_{min} -approach. This reveals a fundamental disagreement between the two theories and suggests that the term “phonon coherence” has been used to describe two fundamentally different physical phenomena.

Attributing any wave-like behavior to phonons in AlAs-GaAs SLs to explain the data in Fig. 6.3(c) (and those in Ref. [22]) will require that κ_{SL} be dictated by the phonon dispersion curve. This will in turn require that κ_{SL} decreases with the increase in d_{SL} due to the formation of mini-bands (see Section 2.2.3), contrary to our data and several literature studies on SLs [34, 36–40, 43, 66, 110]. Moreover, the fact that the phonon coherence length in bulk GaAs is less than 2 nm (see Table 2.1 and Ref. [44]) suggests that it is unlikely for phonon waves to spatially extend over a single period length of our thinnest period samples (2 nm). In addition, it has been shown that for AlAs-GaAs SLs, the interfacial mixing layer is of the order of 1-2 nm [22]. This is enough to destroy any phonon coherence effects and eliminate the possibility of observing a minimum in thermal conductivity, as reported previously [37, 38, 41, 124, 127] and discussed in Chapter 5. Therefore, the linear trend observed in the data of Fig. 6.3 and in Ref. [22] is a result of the ballistic transport of incoherent phonons. These phonons do not display wave behavior and are not affected by the miniband formation in the dispersion curve.

The same trend is also observed in thin film GaAs thermal conductivity data shown in the same figure. This similarity between thin GaAs films and SLs of the same thickness suggests that long mean free path phonons are behaving in a similar way for $L < 200$ nm and the inclusion of interfaces via SLs impedes short mean free path phonons leading to a reduction in the magnitude of thermal conductivity.

6.4 Thermal Model: Series Resistor

The treatment of phonons as particles allows for a satisfying explanation that describes the current and previous results on the thermal conductivity of AlAs-GaAs SLs. Similar to the treatment in Chapter 4, phonons are a gas of particles of different energies and different mean free paths. I model the thermal conductivity of these superlattices as a series resistor model that accounts for short and long range boundary scattering. Hence, the thermal conductivity κ_{SL} is given by:

$$\frac{L}{\kappa_{\text{SL}}(L, d_{\text{SL}}, T)} = \frac{L}{\kappa_0(L, T)} + \frac{2L}{d_{\text{SL}} h_{\text{K}}(d_{\text{SL}}, T)} \quad (6.1)$$

where h_{K} is the thermal boundary conductance across the AlAs-GaAs interfaces and is adjusted to fit the data to the model for $L > 200$ nm and κ_0 is thermal conductivity of the SL of thickness L without the interfaces. κ_0 is modeled by Eq. 2.9 where average properties of GaAs and AlAs are used (lattice constant, dispersion curves, and scattering times). This is justified by the fact that incoherent long mfp phonons “see” the SL as a homogeneous material without discrete interfaces. The details of the calculation of κ_0 are given in Appendix B. The dependence of κ_{SL} on L is accounted for by including a boundary scattering term into the calculation of κ_0 ($\tau_L^{-1} = v(\omega)/L$, see Section 2.4.1). In this model, κ_0 and h_{K} account for the long range and short range boundary scattering, respectively.

Figure 6.3(c) shows reasonable agreement between our data and model calcula-

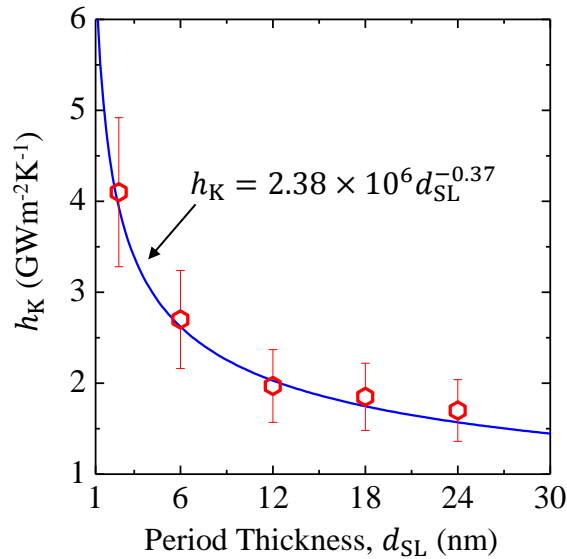


Figure 6.4: Values of thermal boundary conductance used to fit the model given by equation 6.1 to the data in Fig. 6.3 as a function of the period thickness. The solid line is an inverse power fit and is used to generate the thermal conductivity contour plot in Fig 6.6. The error bars were estimated based on the agreement between the model and data in Fig. 6.3.

tions given by Eq. 6.1. The disagreement between the model and the data for low values of L is discussed in Section 6.7. The values for h_K are plotted in Fig. 6.4 as a function of d_{SL} . The increase in h_K with the decrease in d_{SL} suggests that in shorter d_{SL} , a larger portion of the phonon spectrum ballistically traverses the AlAs-GaAs samples scattering less frequently at the internal interfaces defining the SL periodicity. This trend has been previously shown in Si-Ge, AlN-GaN, as well as AlAs-GaAs SLs [128]. However, the large interface density in SLs with shorter d_{SL} leads to a higher thermal resistance that suppresses the thermal conductivity of the 2 nm period thickness samples well below that of the 12 and 24 nm samples. Even with the high values of h_K ($1.7 - 4.1 \text{ GW m}^{-2} \text{ K}^{-1}$), the thermal conductivities of the SLs are significantly lower than that of κ_0 , demonstrating that although the trend in thermal conductivity is dictated by long range boundary scattering for $L < 200 \text{ nm}$, scattering of short mfp phonons from internal interfaces can significantly impact the magnitude

of thermal conductivity of SLs. The data in Fig. 6.4 starts to level off at the 12 nm period and one may expect that h_K for a single interface will be extremely high¹. A value higher than $\sim 200 \text{ MW m}^{-2} \text{ K}^{-1}$ for the interface conductance between the SL film (where the bottom layer of the SL film is AlAs, see Fig. 6.2.) and the GaAs smoothing layer is enough to make the TDTR measurement completely insensitive to this parameter. The trend in Fig. 6.4 suggests that this value is appreciably higher than $\sim 200 \text{ MW m}^{-2} \text{ K}^{-1}$.

6.5 Spectral Contribution to Thermal Conductivity

In this section, I discuss the phononic spectral contribution to the thermal conductivity by calculating the mean free path (mfp) distribution, $\ell_j(\omega, L, T)$ and the thermal conductivity accumulation functions, $\alpha(\ell, L, T)$ and $\alpha(\omega, L, T)$, over phonon mfps and frequencies, respectively. In doing so, we are analyzing a hypothetical SL (without the effects from the internal interfaces). The thermal conductivity of this hypothetical SL is κ_0 .

For bulk and thin film SLs of thicknesses 24, 100, and 1,000 nm, Fig. 6.5(a) shows the mfp $\ell_j(\omega, L, T) = v_j(\omega)\tau_j(\omega, L, T)$ for the longitudinal (LA) and transverse (TA) acoustic branches at room temperature where v_j and τ_j are the phonon group velocity and scattering times. The film boundary scattering term limits the maximum mfp in the SL to the thickness L . In other words, phonons with $\ell > L$ do not exist in the phonon spectrum of the SL. The mfp in a bulk SL shows a strong spectral dependence where phonons of different frequencies have significantly different values of ℓ_j . As the film thickness decreases, ℓ_j flattens and a larger portion of phonon frequencies take mfp values closer to the film thickness (i.e., closer to the maximum mfp).

The effect of film thickness on thermal conductivity can be better seen in

¹In fact, based on the trend in Fig. 6.4, the value of h_K for a single AlAs-GaAs interface might be a record for the highest interface conductance ever reported in phononic systems.

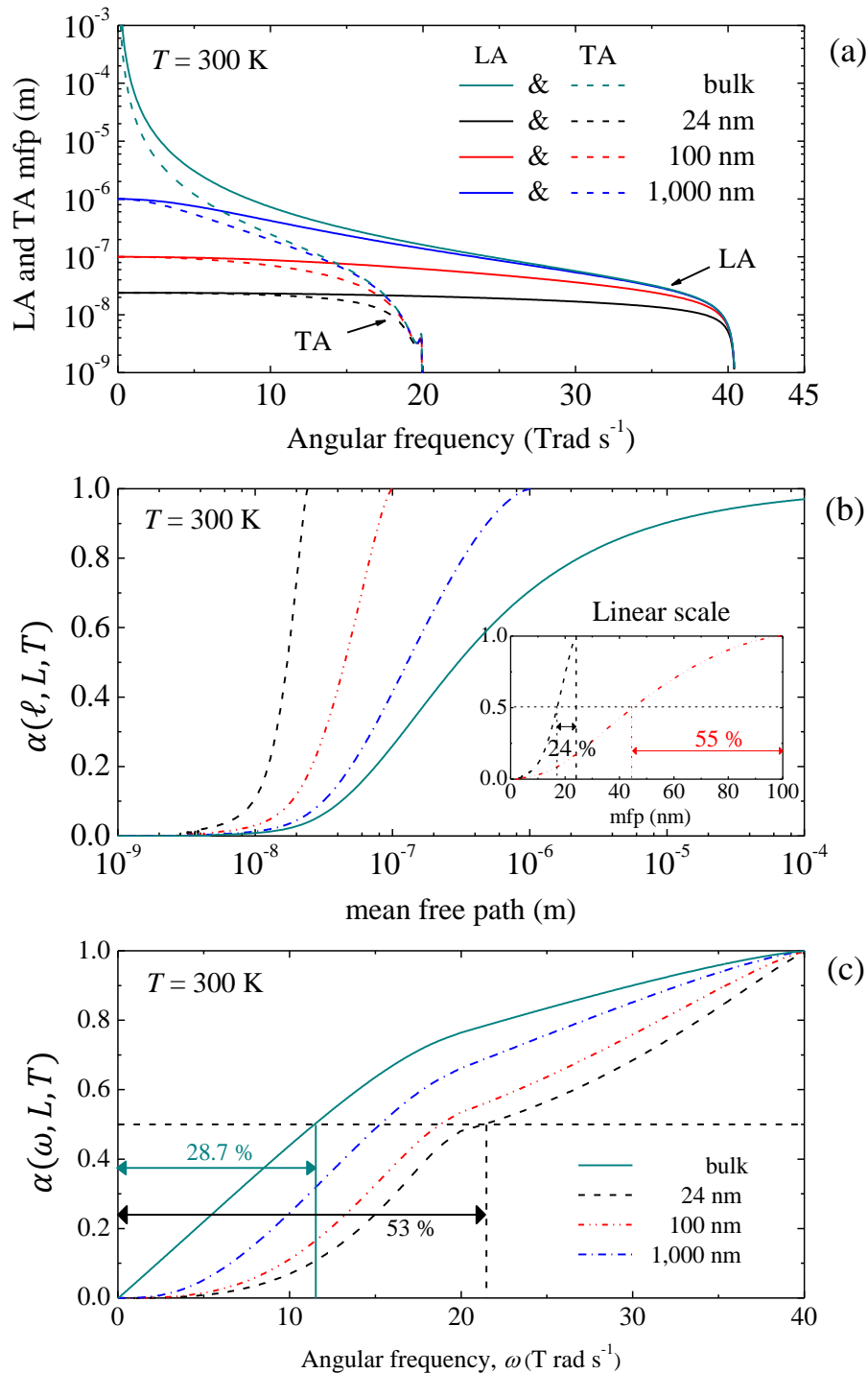


Figure 6.5: (a) mean free path distribution function in the longitudinal acoustic (LA) and transverse acoustic (TA) branches plotted versus phonon angular frequency. (b) The mean free path dependent thermal conductivity accumulation function, $\alpha(\ell, L, T)$, plotted versus mean free path. (c) The frequency dependent thermal conductivity accumulation function, $\alpha(\omega, L, T)$, plotted versus ω . All plots are at room temperature.

Fig. 6.5(b) where $\alpha(\ell, L, T)$ is plotted. The accumulation function is defined by [129]:

$$\alpha(\ell, L, T) = \frac{1}{3} \sum_j \int_0^{\ell_{\max}} C_j(\omega) v_j(\omega) \ell(\omega) d\ell / \kappa_0(L, T) \quad (6.2)$$

where $\ell_{\max} = L$ and ℓ in each branch is given in Fig 6.5(a). In the above equation, the mean free path, ℓ , is the independent variable and the function is normalized by the value of κ_0 for the corresponding film thickness sample analyzed. The accumulation function can quantify the spectral contribution to the thermal conductivity from phonons of different mean free paths. As the thickness increases, this mean free path-dependent accumulation function spreads over a larger portion of the mfp spectrum and becomes more evenly distributed. To better visualize this, $\alpha(\ell, L, T)$ for 24 and 100 nm is plotted on a linear scale in the inset of Fig. 6.5(b). The horizontal and vertical lines in the inset show that 50% of thermal conductivity is carried by the upper 28% (17 - 24 nm) and upper 55% (45 - 100 nm) of the phonon spectrum for the 24 and 100 nm films, respectively. In other words, a smaller portion of the spectrum (28%) in the 24 nm film contributes as much as more than half the portion of the mfp spectrum (55%) in the 100 nm film. This demonstrates how long mfp phonons are more dominant in thinner films.

The same can be observed in Fig. 6.5(c) which plots the frequency-dependent thermal conductivity accumulation. Similar to Eq. 6.2, the frequency-dependent thermal conductivity accumulation is defined:

$$\alpha(\omega, L, T) = \frac{1}{3} \sum_j \int_0^{\omega_{c,j}} C_j(\omega) v_j(\omega) \ell(\omega) d\omega / \kappa_0(L, T) \quad (6.3)$$

where ω is less than the cutoff frequency $\omega_{c,j}$. Figure 6.5(c) shows that as the thickness decreases, the percentile contribution from low frequency phonons (i.e., long mfp) becomes more substantial. The horizontal and vertical lines show that 50% of thermal conductivity is dictated by the lower 28.7% and 54% of the phonon spectrum

Table 6.2: Fraction of thermal conductivity carried by phonons with mfp larger than $L/2$ or frequency lower than $\omega_{\max}/2$

Thickness, L (nm)	24	100	1,000	bulk
$1 - \alpha(\ell, L/2, T)$ (%)	82	43	9.4	-
$\alpha(\omega_{\max}/2, L, T)$ (%)	48	54	66	76.7

in bulk and 24 nm samples, respectively.

The analysis presented in Fig. 6.5 clearly explains the ballistic behavior of phonons observed in AlAs-GaAs SLs. In fact, this result can be generalized to all thin film structures. As the thickness decreases, the spectral contribution to thermal conductivity becomes more dependent on long mfp (low frequency phonons). This is also supported by the similarity between the thermal conductivity trend of GaAs thin films and SLs shown in Fig. 6.3(c). Table 6.2 lists the values for the fraction of thermal conductivity carried by phonons with mfps longer than $L/2$ or with frequencies lower than $\omega_{\max}/2$, where ω_{\max} is the maximum cutoff frequency. For instance, for $L = 24$ nm, 82% of the thermal conductivity is carried by phonons with mfp between 12 and 24 nm. This percentage decreases to only 9.4% for $L = 1,000$ nm. These results show the strong influence of large mfp phonons on the thermal conductivity of thin films. The increased effect of short mfp phonons for larger thicknesses causes the plateau (leveling off) of the thermal conductivity at higher thicknesses shown in Fig. 6.3(c). It is also important to note that the thermal conductivity values of films with $L < 200$ nm for the different period thicknesses are closer in value to each other than those among the thicker films. This stems directly from the dominance of long mfp phonons in thinner films that reduces the portion of phonons available for short range boundary scattering. As the thickness increases, short mfp phonons dominate the spectrum and κ_{SL} becomes solely dependent on d_{SL} .

The use of a thin film accumulation function is more direct for comparing to ther-

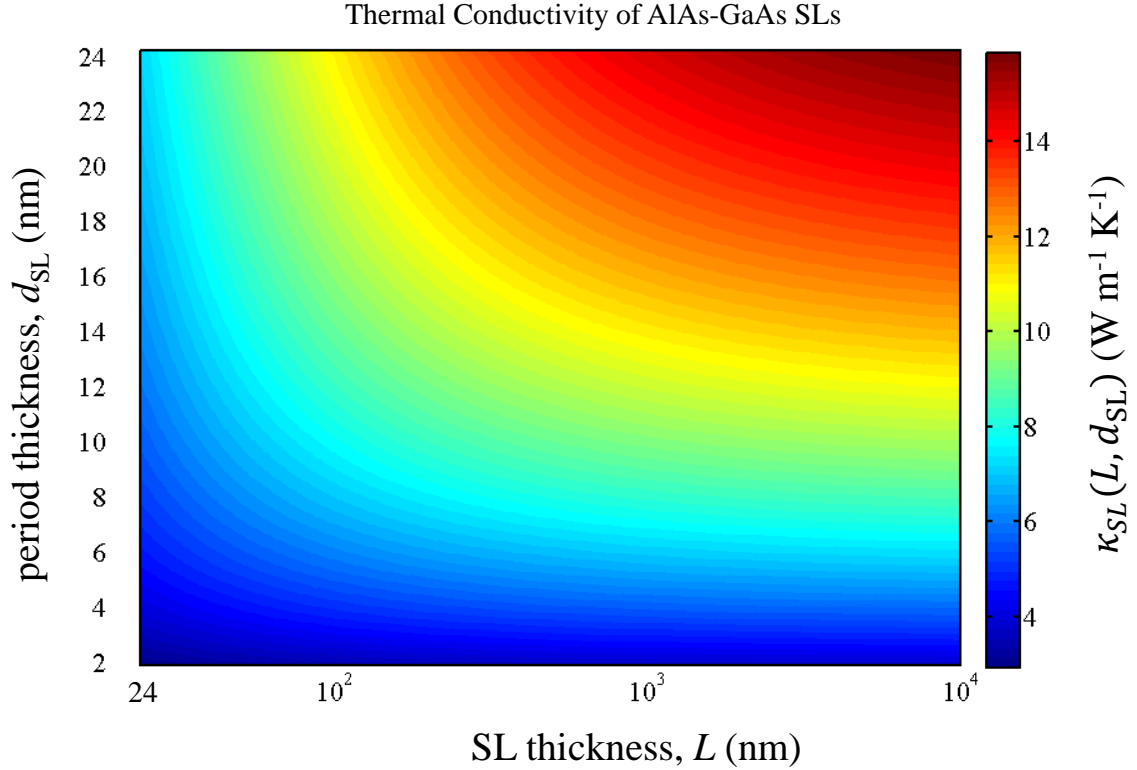


Figure 6.6: Thermal conductivity color map for AlAs-GaAs using Eqs. 6.1 and 6.4 at room temperature. Such map allows for engineering thermal conductivity by selecting the film and period thicknesses.

mal conductivity measurements than the typically used ratio of film to bulk thermal conductivity ($\kappa_{\text{film}}/\kappa_{\text{bulk}}$) accumulation function (e.g., Ref. [129]) or the bulk accumulation [22], as it illustrates the relative importance of the different portions of the mfp spectrum in the thin film structure. While $\kappa_{\text{film}}/\kappa_{\text{bulk}}$ can interpret how a thin film thermal conductivity is affected by the film thickness as compared to bulk, it does not provide direct insight into the spectral dependence of thermal conductivity in a film of a specific thickness.

6.6 Thermal Conductivity Engineering

A major result of the data shown in Figs 6.3(c) and 6.4 is the ability to engineer the thermal conductivity by selecting L and d_{SL} . The ability to precisely prescribe

the thermal conductivity is tied to both film boundary scattering and the thermal boundary conductance across the AlAs-GaAs interfaces. The values used for h_K plotted in Fig. 6.4 are fitted to an inverse law that gives:

$$h_K = 2.38 \times 10^6 d_{\text{SL}}^{-0.37} \quad (6.4)$$

When substituted in Eq. 6.1, this expression allows for evaluating κ_{SL} at any point of coordinates (L, d_{SL}) in the $L - d_{\text{SL}}$ plane. Figure 6.6 shows a thermal conductivity contour plot of AlAs-GaAs SLs at room temperature plotted over the $L - d_{\text{SL}}$ plane. By prescribing L and d_{SL} of a superlattice, an engineering level control of the thermal conductivity is achieved based on the relative contributions of the hierarchical boundary scattering processes. This possibility of precisely prescribing thermal conductivity of a certain material structure is immensely important for a wide range on engineering applications. Technologies in which a SL of finite thickness is integrated onto thermoelectric devices for on-chip cooling or microrefrigerators [14, 15] can utilize such thermal maps to select the superlattice that gives the lowest thermal conductivity for the highest value of d_{SL} (lowest interface density) and the value of L most convenient for the stack of materials forming the device.

6.7 Disagreement between Model and Data

The disagreement between the data and model in Fig. 6.3(c) suggests that the model underestimates the strength of long range boundary scattering for films with thicknesses less than 200 nm. The model only required one adjustable parameter (h_K) which affects the agreement with the data mostly at large values of L . We could in addition use a boundary scattering term with an adjustable parameter to yield a better fit between the data and model for low values of L . Such boundary scattering

term would take the form:

$$\tau_L^{-1} = \frac{bv(\omega)}{L} \quad (6.5)$$

where b is an adjustable parameter. While this approach might lead to a better model-data agreement, there is no solid physical reasoning behind it.

Another possibility for the disagreement could arise from the use of a simplified dispersion curve given by the average of dispersions of GaAs and AlAs (see Appendix B). As shown in Section 2.2.3, the formation of mini-bands can significantly alter the phonon group velocity and the use of an average dispersion can be an over-simplification. I caution that this statement does not contradict the argument on phonon coherence presented in this chapter. It was discussed in Section 6.3 that because of the increase in thermal conductivity with period thickness, the dispersion curve is not what dictates thermal transport. However, the actual form of the dispersion curve does indeed affect the magnitude of the computed thermal conductivity but not the observed trend.

6.8 Summary

In this chapter, I showed that the two approaches to demonstrating phonon coherence in the literature are describing two fundamentally different physical phenomena. The term coherence is better used to express wave-like behavior of phonons (κ_{\min} -approach), which is absent in AlAs-GaAs SLs as illustrated throughout the chapter. The ballistic behavior of phonons in thin SLs is explained in terms of the increased importance of long mfp phonons in thinner films. These are incoherent phonons that do not display wave behavior and are not affected by the variations in the dispersion curve as the period thickness of a superlattice is changed. In addition, using a simple series resistor model, a thermal conductivity map was generated, which allows for engineering the thermal conductivity by carefully selecting both, the period thickness

and total sample thickness of a superlattice.

The results in this chapter line up well with the results of Chapter 4 on the thermal conductivity of thin SiGe films. Long range boundary scattering in thin films alloy as well as superlattices dominates thermal transport causing a reduction in thermal conductivity. This is further supported by the similarity in the thermal conductivity trend when comparing thin film alloys to SLs presented in Chapter 4. The systematic study conducted in this chapter allowed for understanding the interplay between short and long range boundary scattering.

Chapter 7

Electron Transport across Metallic Interfaces

“If we insist on a particulate, electronic theory of electricity, the high conductivity of metals such as copper and silver is exceedingly difficult to explain. The electrons must penetrate through the closely packed arrays of atoms as though these scarcely existed. It is as if one can play cricket in the jungle.”

–J. M. Ziman, *Electrons and Phonons*, Oxford University Press (1969)

7.1 Motivation and Background

Compared to its phonon counterpart, the physics of electron thermal conductance across solid interfaces has received far less attention, even though metal-metal interfaces provide the foundation for a wide array of technical advances. For example, in nuclear applications, interfaces can act as sinks to store radiation induced damage and metallic multilayers¹ have been developed to serve as radiation tolerant shields

¹It is common to use the term multilayers to describe alternating layers of metallic materials rather than superlattice. The term superlattice was originally used to describe semiconductor structures. This terminology is field dependent and the term metallic superlattice is not very uncommon. In this chapter, multilayer is used.

in advanced nuclear systems [73, 130, 131]. In magnetic applications, thermal transport across metallic interfaces can provide a better understanding to the mechanisms driving the giant magnetoresistance (GMR) phenomenon [132, 133]. Despite these important applications, research in the domain of electron thermal transport across metallic interfaces has been very limited and focused on electrical properties [134], validation of the Wiedmann-Franz law [135, 136] or the contribution of electrons to the Kapitza conductance across metallic-nonmetallic interfaces [76, 137–139]. Very few studies have focused on the Kapitza conductance between different metals [136, 140–142].

When considering thermal transport and electron Kapitza conductance, electrons are generally treated as non-spectral heat carriers with a single electron energy and mean free path being sufficient to describe the dominant modes of transport [54]. An examination of different metallic multilayer systems in which electrons have appreciably different mean free paths may provide an insight into the effect of electron characteristic lengths on Kapitza conductance. Gundrum *et al.* [140] reported an interface conductance of $\sim 3.7 \text{ GW m}^{-2} \text{ K}^{-1}$ across aluminum-copper interfaces at room temperature. Wilson and Cahill [136] measured the highest ever reported interface conductance between two solids, $12.1 \text{ GW m}^{-2} \text{ K}^{-1}$, across palladium-iridium interfaces at room temperature. These results are surprising in light of the large difference in electron mean free paths and thermophysical properties of these two systems. While aluminum and copper are both free electron metals with mean free paths of ≈ 15 and 25 nm (see Fig. 7.4), respectively, palladium and iridium are both transition metals and have corresponding electron mean free paths of ≈ 2 and 4 nm , respectively. The fact that a free electron metallic system shows the lower interface conductance is counter intuitive when comparing to phonon mediated systems. It has been shown that the interface conductance between individual layers in phonon mediated multilayers depends on the period thickness of these multilayers [87, 101,

128, 143]. This dependence has been observed in AlAs/GaAs [87] as in Chapter 6, W/Al₂O₃ [143] and AlN/GaN [128] interfaces. In Chapter 6, it was demonstrated that interfaces tend to scatter short mean free path phonons more efficiently than the long mean free path phonons that can ballistically propagate across a SL structure. This suggests that electrons contribution to thermal transport across interfaces is fundamentally different from that of phonons and requires a better understanding of the interplay between materials' intrinsic properties and electrons scattering mechanisms at interfaces.

7.2 Copper Niobium Multilayer Samples

The phase diagram of binary Cu-Nb shows that this system is immiscible and no intermixing should occur in the equilibrium state [144]. This is due to the difference in crystal structure, fcc for Cu and bcc for Nb, and the large atomic radii mismatch between the constituent atoms. Interfaces in sputter deposited Cu-Nb multilayers form along the close packed planes of the {111} Cu and {110} Nb and predominately exhibit a Kurdjumov-Sachs orientation relationship where $\langle 111 \rangle_{\text{Nb}} \parallel \langle 110 \rangle_{\text{Cu}}$. Given these properties, recent molecular dynamics calculations suggest that the Cu-Nb interface remains unmixed up to temperatures as high as 873 K [145]. Moreover, experimental investigations demonstrate that the $\langle 111 \rangle_{\text{Nb}} \parallel \langle 110 \rangle_{\text{Cu}}$ texture is retained after annealing at temperatures as high as 973 K [146]. As a result, Cu-Nb is a well suited system to study the effect of length scale on electron transport across chemically abrupt interfaces.

Seven samples of Cu-Nb multilayer films were synthesized via DC magnetron sputtering by our collaborators at Los Alamos National Laboratories in Dr. Amit Misra's Laboratory. Sample details are given in Table 7.1. The films were grown on intrinsic (100) Si substrates. The deposition was performed at room temperature with 4 mTorr argon partial pressure at a deposition rate of ~ 0.6 nm/s. The copper and niobium

Table 7.1: Layer, d_{Nb} or d_{Cu} , period, d , and total thickness, L , of the seven Cu-Nb samples

Sample	d_{Nb} (nm)	d_{Cu} (nm)	d (nm)	L (nm)
1 (Fig. 7.1A)	2.3	3.1	5.4 ± 0.5	2,677.0
2	2.1	4.4	6.5 ± 1.0	1,614.6
3 (Fig. 7.1B)	2.8	5.6	8.4 ± 1.1	1,396.3
4	2.5	6.0	8.5 ± 0.9	1,069.5
5 (Fig. 7.1C)	5.7	6.8	12.5 ± 1.4	1,252.1
6 (Fig. 7.1D)	11.0	10.4	21.4 ± 2.0	1,069.5
7	48.0	48.2	96.2 ± 4.1	962.0

targets were 100 mm in diameter and were held at powers of 100 W and 200 W, respectively. Layer thicknesses were verified by cross sectional TEM. Figure 7.1 shows high-angle annular dark-field transmission electron microscopy (HAADF STEM) images for samples 1, 3, 5, and 6. TEM images show large waviness at the interfaces. Since Cu and Nb are completely immiscible, this waviness is merely a morphological roughness. The corresponding selected area diffraction pattern (SADP) in the inset of Fig. 7.1 shows a broad Bragg peak corresponding to $\{110\}$ bcc Nb and $\{111\}$ fcc Cu and further demonstrate that there is no chemical intermixing at the interface. The waviness leads to large variations in the measured period thicknesses. The uncertainties in period thickness measurements arising from waviness are listed in Table 7.1 and are taken into consideration in the calculation of Kapitza conductance. All the samples were coated with 70 nm of aluminum which acts as a temperature transducer for our thermal measurements.

7.3 Thermal Conductivity and Kapitza Conductance Results

The cross-plane thermal conductivities of the Cu-Nb multilayers were measured by TDTR. The modulation frequency was 11.4 MHz and the pump and probe radii are 25 μm and 6 μm , respectively. In the analysis, literature values for the heat capacity

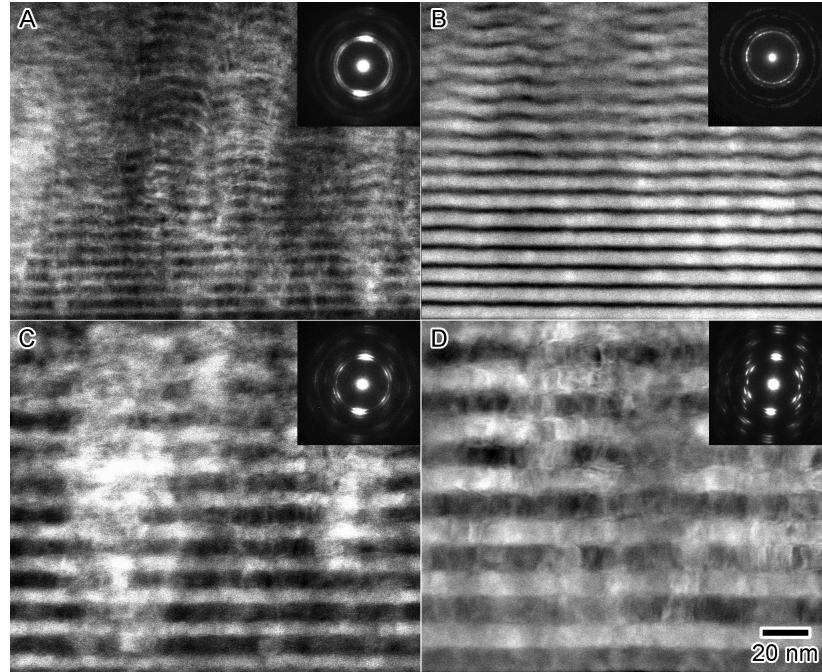


Figure 7.1: HAADF STEM images for Cu-Nb multilayers in (A) sample 1, (B) sample 3, (C) sample 5, (D) sample 6. The insets show the corresponding selected area diffraction pattern (SADP)

of the Al film and the heat capacity and thermal conductivity of the silicon substrate are used. The Cu-Nb multilayers is treated as one layer and a weighted average of the bulk heat capacity values of Cu and Nb based on their volume fraction in each sample is used. The interface resistance between the Cu-Nb multilayer sample and the silicon substrate is assumed to be negligible. Subsequently, the only unknowns in our thermal model are the Al/Cu-Nb Kapitza conductance and the thermal conductivity of the Cu-Nb film. A total of five measurements were taken on each sample over the temperature range from 78 to 500 K in a cryostat with optical access that is kept under vacuum ($<10^{-6}$ Torr). Thermal conductivity results are shown in Fig. 7.2 plotted as a function of period thickness for four different temperatures.

The Cu-Nb Kapitza conductance is calculated using the series thermal resistor

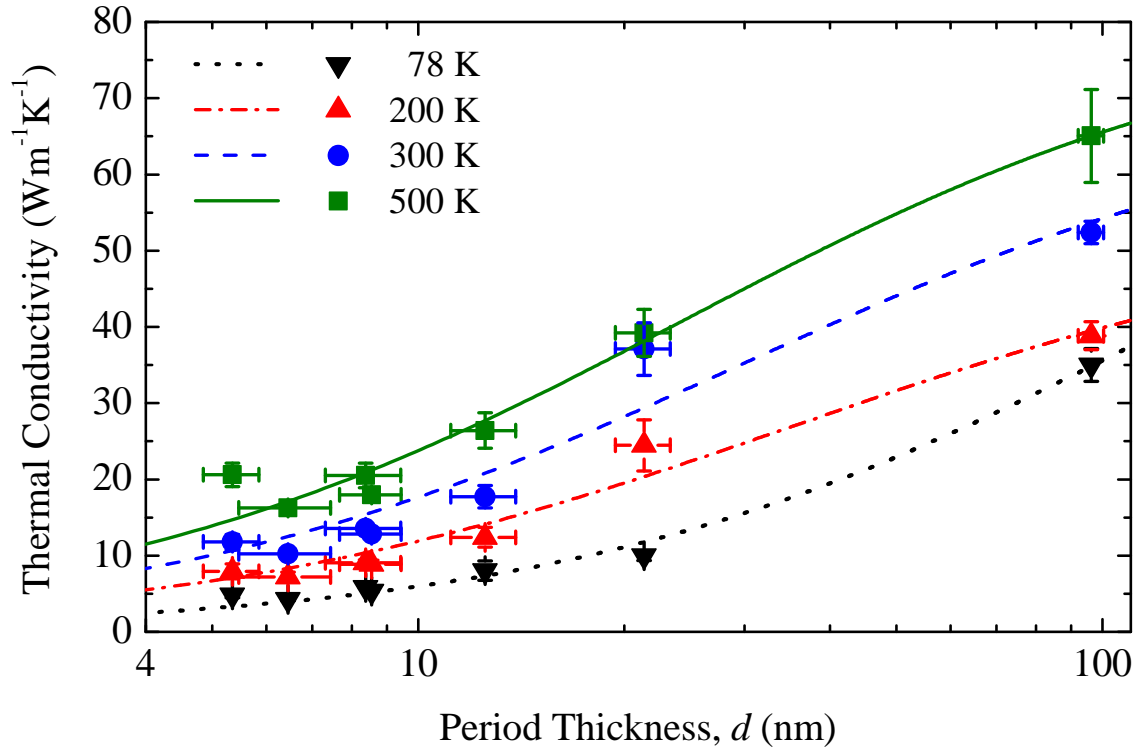


Figure 7.2: Thermal conductivity results from TDTR measurements for the seven Cu-Nb samples plotted versus period thickness over the temperature range 78 - 500 K. The horizontal error bars are the uncertainty in period thickness listed in Table 7.1. Solid lines are the best fit curves for Eq. 7.2 treating r_0/L and $h_{\text{Cu-Nb}}$ as free parameters [147].

model previously used in Chapter 6:

$$R_{\text{tot}} = \frac{L}{\kappa_{\text{measured}}} = R_0 + \frac{n}{h_{\text{Cu-Nb}}} \quad (7.1)$$

where R_{tot} is the total resistance of the Cu-Nb film, L is the sample thickness, R_0 is the thermal resistance due to the Cu-Nb layers without the interfaces, n is the number of interfaces, κ_{measured} is the thermal conductivity of the Cu-Nb film measured by TDTR, and $h_{\text{Cu-Nb}}$ is the Kapitza conductance across Cu-Nb interface.

Contrary to AlAs-GaAs, and given the fact that a single mean free path can describe the entire electron population, $h_{\text{Cu-Nb}}$ is assumed to be independent of the period thickness. In other words, for a constant heat flux, the temperature drops

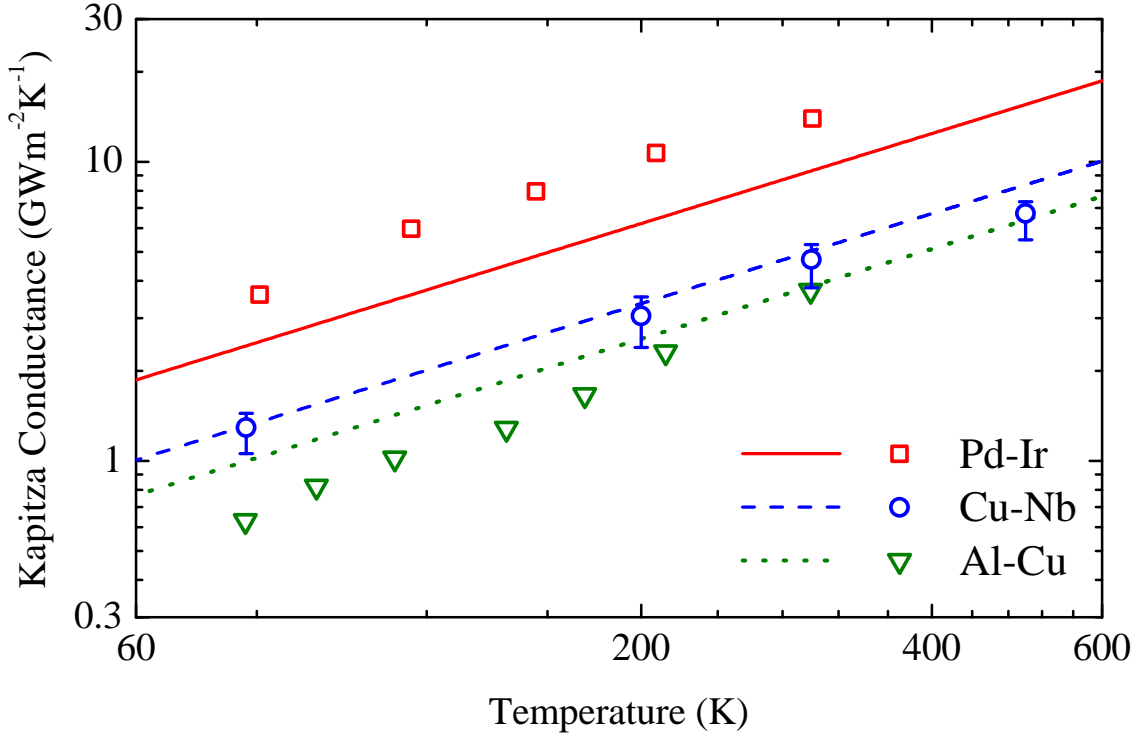


Figure 7.3: Kapitza conductance data and EDMM calculations given by Eq. 7.3 for Cu-Nb (this work), Al-Cu (Ref. [140]) and Pd-Ir (Ref. [136]) versus temperature. Error bars in $h_{\text{Cu-Nb}}$ represent the error in TDTR measurement and the uncertainty in the period thickness measurement listed in Table 7.1. Density of states and Fermi velocities used in the calculation of EDMM are given in Table 7.2.

within each layer and across each interface are independent of the thickness of the layer. The deviation from this assumption is discussed in Section 7.5. Equation 7.1 can be rewritten to express the measured thermal conductivity in terms of the period thickness. Substituting $L = dn/2$ and rearranging:

$$\frac{1}{\kappa_{\text{measured}}} = \frac{r_0}{L} + \frac{2}{dh_{\text{Cu-Nb}}} \quad (7.2)$$

where d is the period thickness. The solid lines in Fig. 7.2 are the best fit curves for Eq. 7.2 treating r_0/L and $h_{\text{Cu-Nb}}$ as free parameters.

7.4 The Electronic Diffuse Mismatch Model (EDMM)

The EDMM is the electronic version of the DMM originally proposed by Swartz and Pohl [148] in 1987. The best fit values for $h_{\text{Cu-Nb}}$ are shown in Fig. 7.3 along with the EDMM. Data and EDMM for Al-Cu [140] and Pd-Ir [136] are also shown for comparison.

The EDMM is given by:

$$h_{1 \rightarrow 2} = \frac{1}{4} \zeta_{1 \rightarrow 2} C_{e,1} \nu_{F,1} = \zeta_{1 \rightarrow 2} \frac{\partial q_1}{\partial T} \quad (7.3)$$

where $C_{e,1}$ is the electronic heat capacity of the metal on side 1 given by [33]: $C_e = (\pi^2/3)D(\varepsilon_F)k_B^2 T$, where k_B is Boltzmann's constant, q_1 is the electrons' energy flux in side 1, T is the temperature, and $\zeta_{1 \rightarrow 2}$ is the transmission coefficient given by:

$$\zeta_{1 \rightarrow 2} = \frac{D(\varepsilon_{F,2})\nu_{F,2}}{D(\varepsilon_{F,2})\nu_{F,2} + D(\varepsilon_{F,1})\nu_{F,1}} \quad (7.4)$$

where $D(\varepsilon_F)$ is the density of states at the Fermi level and ν_F is the Fermi velocity. $1 \rightarrow 2$ denotes that transport is from side 1 to side 2. Values for $D(\varepsilon_F)$ and ν_F are given in Table 7.2. The derivation of the EDMM is given in Ref. [140] and is not repeated here. Note that in the calculations of the EDMM, I use literature values for the density of states at the Fermi level instead of the low temperature values for γ used in Refs. [136, 140] where the electronic heat capacity is given by $C_e = \gamma T$. Thus the EDMM for Pd-Ir and Al-Cu shown in Fig. 7.3 are slightly different from the model calculations in Refs. [136, 140].

Table 7.2: Parameters used in the calculation of the EDMM

Metal	$D(\varepsilon_F) (\times 10^{47} \text{ m}^{-3})$	$\nu_F (\times 10^6 \text{ m s}^{-1})$
Cu	1.41 [149]	1.12 [140]
Nb	5.31 [150]	0.62 [151]
Ir	4.57 [152]	8.25 [152]
Pd	9.69 [153]	4.32 [136]
Al	1.26 [154]	1.33 [140]
Pt	7.05 [155]	0.33 [155]

7.5 Analysis

The results on $h_{\text{Cu-Nb}}$ shown in Fig. 7.3 are in reasonable agreement with the EDMM and further demonstrates the usefulness of this simple model. The surprising result in Fig. 7.3 is that $h_{\text{Al-Cu}}$ is less than $h_{\text{Pd-Ir}}$ and $h_{\text{Cu-Nb}}$. Given the higher thermal conductivities and longer electron mean free paths in Cu and Al, one might expect Al-Cu to show the highest interface conductance. This expectation is based on similar mean free path assertions in previous work of phonon Kapitza conductance [57, 128] as discussed in more detail below.

To gain further insight, we consider the right hand side of Eq. 7.3 where Kapitza conductance is written as the product of the transmission coefficient and the temperature derivative of the electrons energy flux in side 1. The values for $\zeta_{1 \rightarrow 2}$ are

Table 7.3: Transmission coefficient for the Cu-Nb, Al-Cu and Pd-Ir and the temperature derivative of electrons energy flux in the metal on side 1.

Side 1	Side 2	$\zeta_{1 \rightarrow 2}$	$\partial q_1 / \partial T$ ($\text{GWm}^{-2}\text{K}^{-1}$)
Cu	Nb	0.67	$0.025T$
Nb	Cu	0.33	$0.051T$
Al	Cu	0.48	$0.026T$
Cu	Al	0.52	$0.024T$
Pd	Ir	0.47	$0.066T$
Ir	Pd	0.53	$0.059T$

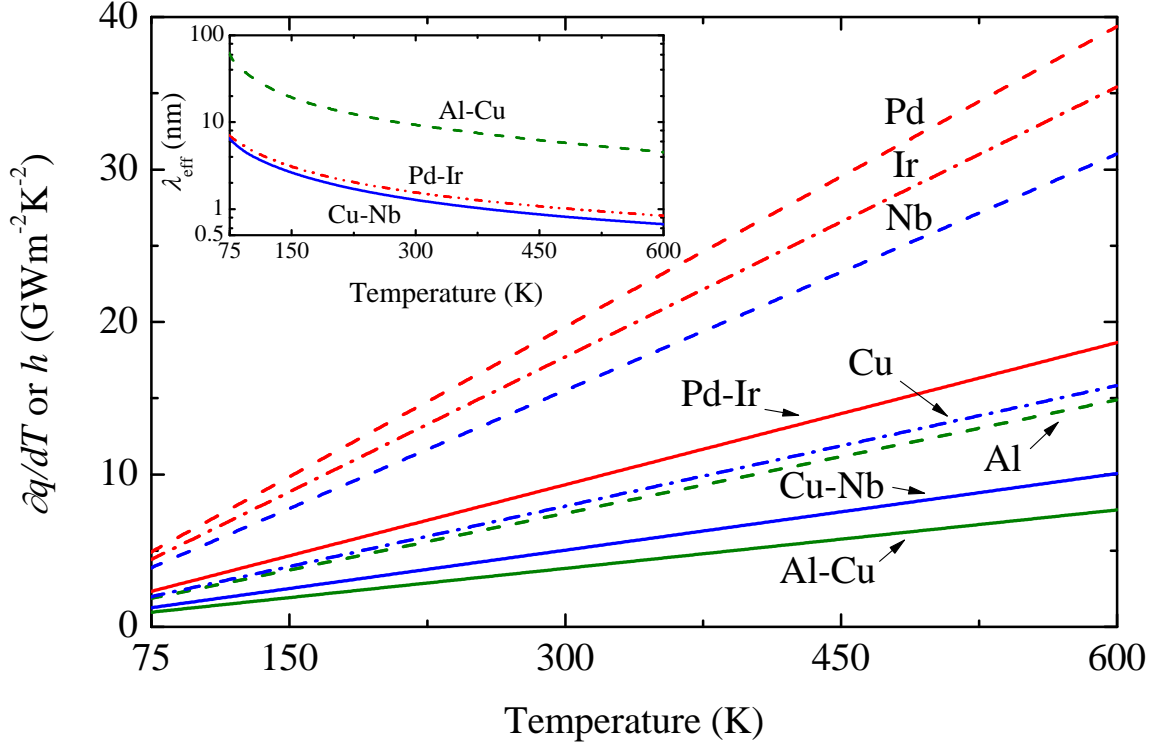


Figure 7.4: Temperature derivative of the electrons energy flux in each of the metallic layers constituting the 3 multilayer systems considered in this study (dash-dot and dotted lines) and Kapitza conductance of Cu-Nb, Al-Cu, and Pd-Ir calculated by the EDMM given in Eq. 7.3 (solid lines). The inset shows the effective mean free path of electrons in each system. Despite Al-Cu displaying the largest mean free path compared to Pd-Ir and Cu-Nb, it has the lowest Kapitza conductance of all three systems.

listed in Table 7.3 along with the values of $\partial q_1/\partial T$ for the three discussed systems. Figure 7.4 also plots $\partial q_1/\partial T$ as a function of temperature for all the metallic layers forming the three metallic systems along with the Kapitza conductance predictions from the EDMM. A comparison between Al-Cu and Pd-Ir shows that both systems have almost identical transmission coefficients, and thus electron fluxes in the Pd and Ir layers cause $h_{\text{Pd-Ir}}$ to be a factor of ~ 2.5 higher than that of $h_{\text{Al-Cu}}$. A similar comparison can be made for Cu-Nb and Al-Cu. Although Cu-Nb has a lower transmission coefficient than Al-Cu (setting Nb and Al to side 1), the fact that $\partial q_{\text{Nb}}/\partial T$ is twice that in aluminum produces the higher Kapitza conductance in Cu-Nb. This brings us to the conclusion that the magnitudes of thermal boundary conductances

across metallic interfaces are not necessarily dictated by the mismatch in electronic properties (density of states and Fermi velocity) given by the transmission coefficient, but are directly correlated to the temperature derivative of the electrons' energy flux incident on the interface. This conclusion can be further examined by considering the dominant electron length scale in the metallic systems. The effective electron mean free path in the multilayers is given by Matthiessen's rule [54]:

$$\frac{1}{\ell_{eff}} = \frac{1}{\ell_1} + \frac{1}{\ell_2}. \quad (7.5)$$

where ℓ_1 and ℓ_2 are the electron mean free paths in layers 1 and 2, respectively. ℓ inside each layer can be estimated by [156]:

$$\ell = \frac{6\kappa}{\pi^2 k_B^2 D(\varepsilon_F) \nu_F T} \quad (7.6)$$

where κ is the metal thermal conductivity taken from literature [46]. Figure 7.4 shows that the calculated effective mean free path in a hypothetical Al-Cu multilayer is one order of magnitude higher than those of Pd-Ir and Cu-Nb. In Chapter 6, I discussed that interfaces in multilayers are more efficient in transmitting long mean free path phonons. In comparison to phonons, one would expect that Al-Cu would show the highest Kapitza conductance of the three metallic systems as interfaces would be more efficient in transmitting the long mean free path electrons. Nevertheless, Al-Cu shows the lowest Kapitza conductance of all three systems. This result demonstrates that electron transport and phonon transport are fundamentally different in multilayer systems. I attribute this difference to the spectral nature of phonons. Changing the period thickness in a phonon mediated multilayer system alters the portion of the spectrum dominating the transport. In electron dominated systems and at relatively low electron temperatures, spectral effects do not play a role (under the diffusive assumption) and electrons in these metals can always be described with a single mean

free path. It is hence the “availability” of heat carrying electrons represented by the electron energy flux ($\partial q/\partial T$) that dictates the magnitude of the interface conductance regardless of carriers’ characteristic lengths.

The electron flux inside the metallic layers is an intrinsic property of the material and can be relatively well predicted from accurate considerations of material’s electronic heat capacity without any assumptions of the interfacial scattering mechanisms. Such assumptions often rely on the nature of electron scattering and energy transfer across interfaces which can complicate analyses. This conclusion means that we can predict Kapitza conductance by the simple considerations of the EDMM. As an example, consider a palladium-platinum interface. Following the EDMM we find that $\zeta_{\text{Pt}\rightarrow\text{Pd}} = 0.64$, $\partial q_{\text{Pt}}/\partial T = 0.036T$, $h_{\text{Pd}\rightarrow\text{Pt}} = 0.023T$ in units of $\text{GW m}^{-2} \text{K}^{-1}$. The Pd-Pt systems falls between Pd-Ir and Cu-Nb where $h_{\text{Pd}\rightarrow\text{Ir}} = 0.031T$ and $h_{\text{Cu}\rightarrow\text{Nb}} = 0.017T \text{ GW m}^{-2} \text{K}^{-1}$. This demonstrates the possibility of using the EDMM in engineering interfaces with specific Kapitza conductances.

I note that in the treatment, ballistic contributions to the transport across interfaces was ignored. The effective mean free path in a hypothetical Cu-Nb layer is ~ 1.6 nm which is less than the shortest period thickness in our Cu-Nb samples. While this does not refute the possibility of the existence of ballistic electrons contributing to the measured Kapitza conductance, I argue that it would be extremely difficult to detect this in Cu-Nb multilayer over the temperature range of interest in this study. A multilayer grown from free electron metals (e.g., Al-Cu) would be ideal to test for ballistic transport in the case where electrons effective mean free path is larger than the period thickness.

7.6 Summary

In this chapter, I have shown that interfacial transport in electrons is fundamentally different from that of phonons. I demonstrated that Kapitza conductance is mostly

dictated by the electron energy flux in the metallic layers more so than the mismatch in electronic properties between layers or electron mean free paths in the system. The results were in good agreement with the EDMM and illustrate that this simple model can be used to engineer interfaces with specific Kapitza conductances.

Chapter 8

Summary, Impact, and Future

Projects

“The scientific man does not aim at an immediate result. He does not expect that his advanced ideas will be readily taken up. His work is like that of the planter – for the future. His duty is to lay the foundation for those who are to come, and point the way. He lives and labors and hopes.”

–Nikola Tesla

The ongoing miniaturization of electronic devices continues to pose challenges in nanoscale thermal management. Understanding the fundamentals of the behavior of heat carriers in thin film nanostructures is vital for the advancements of a wide array of modern technologies. As the dimensions of materials shrink to few hundreds of nanometers, thermal transport in these materials becomes limited by size effects and interface densities. This work represents a thorough study on the role of size effects and the behavior of phonons and electrons at solid-solid interfaces in thin film alloys and superlattices. Thermal measurements on four different material systems with thicknesses spanning three orders of magnitude have been presented.

8.1 Summary

In Chapter 2, some of the basic concepts for the analysis of topics discussed in Chapters 4 - 7 were introduced and the two approaches (κ_{\min} and κ_{ball}) for demonstrating phonon coherence were discussed. The formation of minibands in the dispersion curve was presented to explain the crossover from coherent to incoherent transport in the κ_{\min} -approach. The formation of minibands was later used in Chapter 6 to demonstrate how the two approaches are describing two fundamentally different physical phenomena.

Chapter 3 provided the details of time-domain thermoreflectance (TDTR), the measurement technique that was built and utilized for the thermal characterization of all the samples studied in this work. The main optical components of the two-tint and double-color arrangements were presented and a discussion on the pros and cons of each arrangement was given. A step-by-step derivation of the thermal and lock-in amplifier responses was given in a generic mathematical representation. This representation allows for easily deriving the electronics response for similar pump-probe apparatuses.

Results in Chapter 4 demonstrated significant reductions in the thermal conductivities of the thin films SiGe as compared to their bulk counterparts. This reduction is attributed to long range boundary scattering of the long mean free path phonons, which serve as the primary thermal carriers. This result illuminated the substantial role of size effects on phonon transport in non-dilute alloys and superlattices while diminishing the often-thought dominance of alloy scattering in thin-film alloys. The conclusions in Chapter 4 raised questions on the interplay between short range and long range boundary scattering in superlattices, which was explored in depth in the later chapters.

In Chapter 5, the first unambiguous experimental evidence for the crossover from

coherent (wave-like) to incoherent (particle-like) transport in SLs was presented. This crossover manifests itself as a minimum in thermal conductivity as a function of period thickness. In the coherent regime, the superlattice is seen as a new homogeneous material in which phonon wavepackets propagate without losing their phase information at the internal interfaces. In the incoherent regime, phonons act as particles and interfaces add to the overall thermal resistance of the superlattice.

In Chapter 6, results of thermal conductivity measurements on AlAs-GaAs SLs lead to the reinterpretation of the concepts of phonon coherence presented in the literature and suggest that the behavior of phonons in AlAs-GaAs SLs is not dictated by the phonon dispersion curves but is best explained in terms of the ballistic transport of incoherent phonons in thin film SLs. The major result of this chapter is demonstrating the possibility to tailor thermal conductivity by carefully selecting the period thickness and sample thickness. This result is capable of advancing research in technologies in which thermal management is a challenge.

In Chapter 7, thermal transport across metallic interfaces was studied, a topic that has not received substantial attention in the literature, especially in comparison to thermal transport across semiconductor-based interfaces. Thermal measurements on Cu-Nb multilayers demonstrate that the interface conductance in metallic systems is dictated by the temperature derivative of the electron energy flux in the metallic layers rather than electron mean free path or scattering processes at the interface.

8.2 Impact

The major impact of this work is in rectifying some of the concepts in literature and “filling in the blanks” on missing pieces of evidence necessary for understanding aspects of thermal transport at the nanoscale. The results of Chapter 4 (Ref. [20]) emphasized that if a comparison is to be made between the thermal conductivities of superlattices and alloys, the total sample thicknesses of each must be considered.

Based on this result, the thin film alloy limit was introduced for comparing thin film alloy thermal conductivities to other structures. The minimum in thermal conductivity of SLs has been theoretically and computationally studied over the past 15 years. The work in Chapter 5 (Ref. [21]) is the first clear experimental evidence of the existence of this minimum. The work in Chapter 6 provided a comprehensive study on the interplay between short and long range boundary scattering and rectified the concept and definition of phonon coherence in SLs. The work in Chapter 7 (Ref. [147]) touched on a topic that is not well addressed in the literature. The comparison between phonons and electrons presented in this chapter, showed how their behavior is fundamentally different.

8.3 Future Projects

Several ideas and topics can follow from the results in this dissertation. The thermal conductivity contour plot given in Chapter 6 would be much more powerful if coupled with an electrical conductivity contour plot for thermoelectric applications. While lower thermal conductivities can be achieved by increasing the interface density, interfaces also impede electrical conductivity which causes a reduction in the thermoelectric figure of merit. Having a contour plot of both electrical and thermal conductivities will allow us to find a combination of d_{SL} and L that maximizes the figure of merit for thermoelectric devices. The values of the Kapitza conductance for AlAs-GaAs interfaces (Fig. 6.4) in the SL samples suggest that the value of h_{K} for a single interface could be higher than the current record for phononic system ($800 \text{ MW m}^{-2} \text{ K}^{-1}$ for $\text{SrRuO}_3/\text{SrTiO}_3$ [157]). This idea is worth pursuing. A study on metallic multilayers made up of free electron metals allows for assessing ballistic electron transport in these structures. A repetition of the STO-CTO study with thinner or thicker films allows for studying the effect of long range boundary scattering on phonon coherence.

Appendices

Appendix A

Proof of Equation 3.28

Here the details for obtaining Eq. 3.28 are given. We wish to prove the following:

$$\int_0^{\infty} \mathcal{L}_0(r, \omega) L_1(r) 2\pi r dr = \frac{1}{2\pi} \int_0^{\infty} \chi \left(\frac{-\tilde{\mathcal{D}}}{\tilde{\mathcal{C}}} \right) \exp\left(\frac{-\chi^2 (r_0^2 + r_1^2)}{8}\right) d\chi \quad (\text{A.1})$$

We start by regrouping the terms in the integral in the following way:

$$\begin{aligned} \int_0^{\infty} \mathcal{L}_0(r, \omega) L_1(r) 2\pi r dr = \\ \int_0^{\infty} \int_0^{\infty} \left[\frac{1}{2\pi} \chi J_0(\chi r) \left(\frac{-\tilde{\mathcal{D}}}{\tilde{\mathcal{C}}} \right) \exp\left(\frac{-\chi^2 r_0^2}{8}\right) \right] \left[\frac{2}{\pi r_1^2} \exp\left(\frac{-2r^2}{r_1^2}\right) 2\pi r \right] dr d\chi = \\ \int_0^{\infty} \left[\int_0^{\infty} r J_0(\chi r) \frac{2}{\pi r_1^2} \exp\left(\frac{-2r^2}{r_1^2}\right) dr \right] \left(\frac{-\tilde{\mathcal{D}}}{\tilde{\mathcal{C}}} \right) \exp\left(\frac{-\chi^2}{r_0^2}\right) \chi d\chi \quad (\text{A.2}) \end{aligned}$$

The term between brackets in the right hand side of the equation is simply the Hankel transform of the probe intensity profile given by:

$$\int_0^{\infty} r J_0(\chi r) \frac{2}{\pi r_1^2} \exp\left(\frac{-2r^2}{r_1^2}\right) dr = \frac{2}{\pi r_1} \exp\left(\frac{-\chi^2 r_1^2}{8}\right) \quad (\text{A.3})$$

substituting into Eq. A.2 and regrouping we get Eq. A.1.

Appendix B

Thermal Conductivity of AlAs-GaAs Superlattices

B.1 Dispersion Curves for AlAs-GaAs SLs

Dispersion curves for GaAs and AlAs were obtained by fitting the dispersion curves in the [100] direction from literature [158, 159] to a 4th order polynomial. Optical modes are ignored and the model accounts only for the longitudinal acoustic (LA) and transverse acoustic (TA) branches in the calculation of thermal conductivity. Figure B.1 shows the dispersion curves for GaAs and AlAs. For the AlAs-GaAs superlattices, we take the average of the dispersion curves of GaAs and AlAs on each branch, where these dispersion curves are defined over a Brillouin zone with a lattice constant $a = (a_{\text{GaAs}} + a_{\text{AlAs}})/2$ where $a_{\text{GaAs(AlAs)}}$ is the lattice constant of GaAs (AlAs). The wavevector k in the first Brillouin zone is defined over $[0, 2\pi/a]$. The dispersion curves corresponding to the AlAs-GaAs SLs used for the calculation of the model given by Eq. 6.1 are plotted in Fig. B.1.

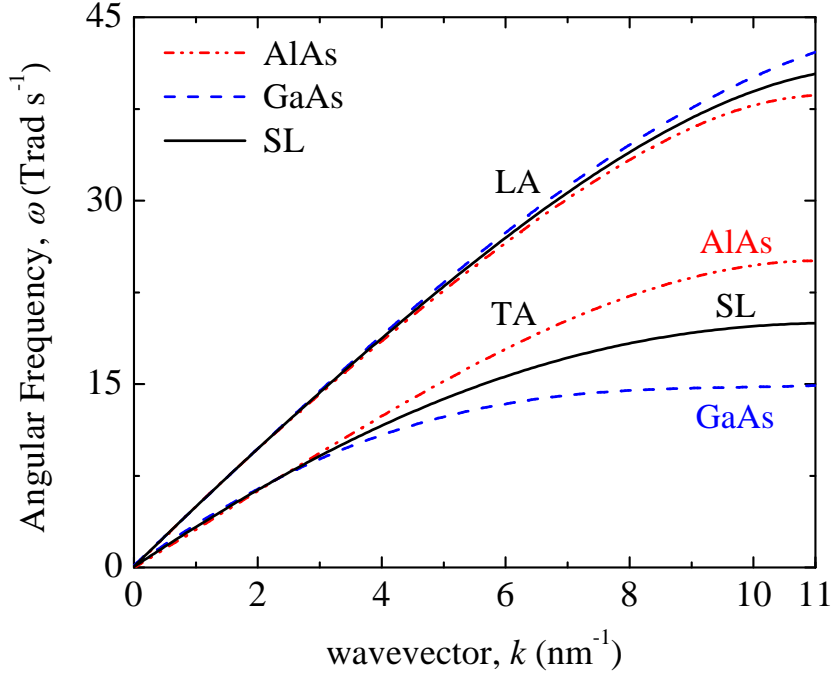


Figure B.1: Dispersion curves of AlAs (Ref. [158]), GaAs (Ref. [159]), and the average dispersion used in the calculation of κ_0 in Eq. 6.1

B.2 Thermal Conductivity Calculations

The thermal conductivity, κ_0 , is given by Eq. 2.9:

$$\kappa_0(L, T) = \frac{1}{3} \sum_j \int_0^{\omega_{c,SL,j}} \hbar \omega D_j(\omega) \frac{\partial f}{\partial T} v_{SL,j}^2(\omega) \tau_{SL,j}(\omega, L, T) d\omega \quad (\text{B.1})$$

where j is the phonon branch and accounts for the LA and TA branches shown in Fig. B.1, and $v_{SL,j}$ is the slope of the average dispersion curve shown in Fig. B.1. The integration is carried over the frequencies given by the SL dispersion and $\omega_{c,SL,j}$ is cutoff frequency in this dispersion. The relaxation time for a given frequency, temperature, thickness, and branch, $\tau_{SL,j}(\omega, L, T)$, is related to the individual processes via Matthiessen's rule, $\tau_j = (\tau_{U,j}^{-1} + \tau_{I,j}^{-1} + \tau_{L,j}^{-1})^{-1}$, where τ_U , τ_I , and τ_L are the Umklapp,

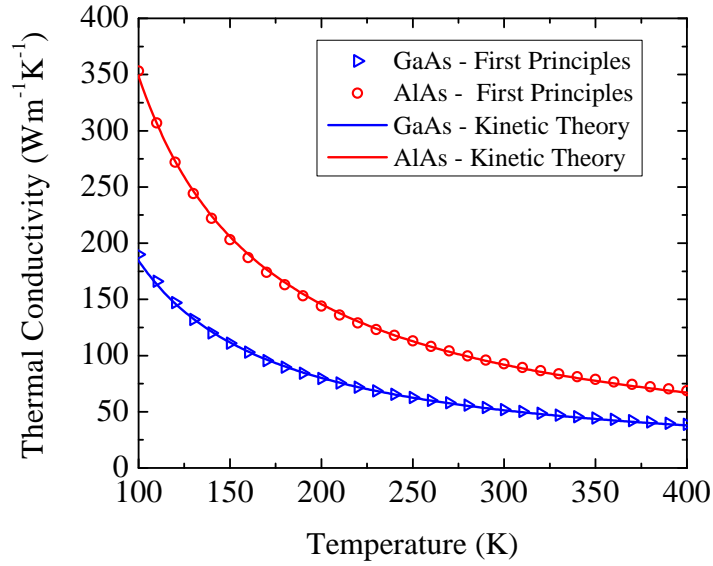


Figure B.2: The agreement between the Kinetic Theory thermal conductivity model given by Eq. 2.9 and the first principles calculations for thermal conductivity of AlAs and GaAs using the parameters listed in Table B.1.

impurity, and boundary scattering times, respectively. These are given by:

$$\tau_{U,j}^{-1}(\omega, T) = \frac{1}{2}\tau_{U,j,\text{AlAs}}^{-1}(\omega, T) + \frac{1}{2}\tau_{U,j,\text{GaAs}}^{-1}(\omega, T) \quad (\text{B.2})$$

$$\tau_{I,j}^{-1}(\omega) = \frac{1}{2}\tau_{I,j,\text{AlAs}}^{-1}(\omega) + \frac{1}{2}\tau_{I,j,\text{GaAs}}^{-1}(\omega) \quad (\text{B.3})$$

and

$$\tau_{j,L}^{-1}(\omega, L) = \frac{v_{\text{SL},j}(\omega)}{L} \quad (\text{B.4})$$

where

$$\tau_{U,j,\text{AlAs}}^{-1} = B_{\text{AlAs}}\omega^2 T \exp(-C_{\text{AlAs}}/T) \quad (\text{B.5})$$

$$\tau_{U,j,\text{GaAs}}^{-1} = B_{\text{GaAs}}\omega^2 T \exp(-C_{\text{GaAs}}/T) \quad (\text{B.6})$$

$$\tau_{I,j,\text{AlAs}}^{-1} = A_{\text{AlAs}}\omega^4 \quad (\text{B.7})$$

and

$$\tau_{I,j,\text{GaAs}}^{-1} = A_{\text{GaAs}}\omega^4 \tag{B.8}$$

Usually, constants A , B , and C are obtained by fitting data of bulk GaAs and AlAs thermal conductivity over temperature to the model given by Eq. 2.9. However, no temperature dependent data on AlAs exist in the literature. In addition, there exist a huge disagreement in literature data on the thermal conductivity of GaAs. For instance, the room temperature value is anywhere between 37 - 54.5 W m⁻¹ K⁻¹ (See page 47 in Ref. [160], also compare values between Refs. [161] and [47]). As a result, and to avoid this discrepancy and lack of data, we use the thermal conductivity of AlAs and GaAs from first principle calculations performed by collaborators from the Department of Electrical and Computer Engineering at the University of Virginia, group of Professor Avik Gosh. To obtain, A , B , and C we fit the kinetic theory model given by Eq. 2.9 to the “data” obtained from first principles. Fig. B.2 shows the agreement between Eq. 2.9 and first principles calculations for the values of A , B , and C listed in Table B.1.

For the first principle calculations, the thermal conductivity of GaAs and AlAs is given by [162]:

$$\kappa^{\alpha\beta} = \frac{1}{k_B T^2 \Omega N} \sum_{\lambda} f_0(f_0 + 1) (\hbar\omega_{\lambda})^2 v_{\lambda}^{\alpha} F_{\lambda}^{\beta}. \tag{B.9}$$

where k_B is Boltzmann’s constant, \hbar is Plank’s constant, Ω is the volume of the simulation unit cell, N is the number of wavevectors q used in the simulation, f_0 is the

Table B.1: Relaxation time parameters for AlAs and GaAs obtained by fitting the kinetic theory model for thermal conductivity given by Eq. 2.9 and the first principle calculations.

Material	A (rad ⁻⁴ s ³)	B (rad ⁻² s K ⁻¹)	C (K)
AlAs	7.8×10^{-44}	2.00×10^{-19}	130
GaAs	9.0×10^{-44}	2.32×10^{-19}	90

equilibrium phonon distribution function, ω_λ is the angular frequency of phonon mode λ , v is the group velocity of phonon mode λ and polarization α , and F_λ^β is a function obtained by solving the Boltzmann transport equation (BTE) self-consistently [162–166]. The solution process is iterative and is done using an open source self-consistent BTE solver ShengBTE [162] with a dense $24 \times 24 \times 24$ q-mesh.

Bibliography

- [1] M. Trigo, A. Bruchhausen, A. Fainstein, B. Jusserand, and V. Thierry-Mieg. [Confinement of Acoustical Vibrations in a Semiconductor Planar Phonon Cavity](#). *Physical Review Letters* **89**, 227402 (2002).
- [2] Donald F. Hornig. [The Vibrational Spectra of Molecules and Complex Ions in Crystals. I. General Theory](#). *The Journal of Chemical Physics* **16**, 1063 (1948).
- [3] A. J. Sievers and S. Takeno. [Intrinsic Localized Modes in Anharmonic Crystals](#). *Physical Review Letters* **61**, 970 (1988).
- [4] G. Shirane, J.D. Axe, and R.J. Birgeneau. [Neutron scattering study of the lattice dynamical phase transition in \$V_3Si\$](#) . *Solid State Communications* **9**, 397 (1971).
- [5] J. D. Axe and G. Shirane. [Inelastic-Neutron-Scattering Study of Acoustic Phonons in \$Nb_3Sn\$](#) . *Physical Review B* **8**, 1965 (1973).
- [6] J. A. Kash, J. C. Tsang, and J. M. Hvam. [Subpicosecond Time-Resolved Raman Spectroscopy of LO Phonons in GaAs](#). *Physical Review Letters* **54**, 2151 (1985).
- [7] C. Thomsen, J. Strait, Z. Vardeny, H. J. Maris, J. Tauc, and J. J. Hauser. [Coherent Phonon Generation and Detection by Picosecond Light Pulses](#). *Physical Review Letters* **53**, 989 (1984).

- [8] C. Thomsen, H. T. Grahn, H. J. Maris, and J. Tauc. [Surface generation and detection of phonons by picosecond light pulses](#). *Physical Review B* **34**, 4129 (1986).
- [9] W.J. de Haas and Th. Biermasz. [The thermal conductivity of quartz at low temperatures](#). *Physica* **2**, 673 (1935).
- [10] W.J. De Haas and Th. Biermasz. [The thermal conductivity of KBr, KCl and SiO₂ at low temperatures](#). *Physica* **4**, 752 (1937).
- [11] H.B.G. Casimir. [Note on the conduction of heat in crystals](#). *Physica* **5**, 495 (1938).
- [12] David G. Cahill, Wayne K. Ford, Kenneth E. Goodson, Gerald D. Mahan, Arun Majumdar, Humphrey J. Maris, Roberto Merlin, and Simon R. Phillpot. [Nanoscale thermal transport](#). *Journal of Applied Physics* **93**, 793 (2003).
- [13] Rama Venkatasubramanian, Edward Siivola, Thomas Colpitts, and Brooks O'quinn. [Thin-film thermoelectric devices with high room-temperature figures of merit](#). *Nature* **413**, 597 (2001).
- [14] Ali Shakouri. [Nanoscale thermal transport and microrefrigerators on a chip](#). *Proceedings of the IEEE* **94**, 1613 (2006).
- [15] Ihtesham Chowdhury, Ravi Prasher, Kelly Lofgreen, Gregory Chrysler, Sridhar Narasimhan, Ravi Mahajan, David Koester, Randall Alley, and Rama Venkatasubramanian. [On-chip cooling by superlattice-based thin-film thermoelectrics](#). *Nature Nanotechnology* **4**, 235 (2009).
- [16] Pernell Dongmo, Yujun Zhong, Peter Attia, Cory Bomberger, Ramez Cheaito, Jon F. Ihlefeld, Patrick E. Hopkins, and Joshua Zide. [Enhanced room temperature electronic and thermoelectric properties of the dilute bismuthide InGaBiAs](#). *Journal of Applied Physics* **112**, 093710 (2012).

-
- [17] Cheng Zhu, Yong-gang Zhang, Ai-zhen Li, and Zhao-bing Tian. [Analysis of key parameters affecting the thermal behavior and performance of quantum cascade lasers](#). *Journal of Applied Physics* **100**, 053105 (2006).
- [18] G. Chen, C. L. Tien, X. Wu, and J. S. Smith. [Thermal Diffusivity Measurement of GaAs/AlGaAs Thin-Film Structures](#). *Journal of Heat Transfer* **116**, 325 (1994).
- [19] T. C. Chong, L. P. Shi, R. Zhao, P. K. Tan, J. M. Li, H. K. Lee, X. S. Miao, A. Y. Du, and C. H. Tung. [Phase change random access memory cell with superlattice-like structure](#). *Applied Physics Letters* **88**, 122114 (2006).
- [20] Ramez Cheaito, John C Duda, Thomas E Beechem, Khalid Hattar, Jon F Ihlefeld, Douglas L Medlin, Mark A Rodriguez, Michael J Campion, Edward S Piekos, and Patrick E Hopkins. [Experimental Investigation of Size Effects on the Thermal Conductivity of Silicon-Germanium Alloy Thin Films](#). *Physical Review Letters* **109**, 195901 (2012).
- [21] Jayakanth Ravichandran, Ajay K Yadav, Ramez Cheaito, Pim B Rossen, Arsen Soukiassian, SJ Suresha, John C Duda, Brian M Foley, Che-Hui Lee, Ye Zhu, et al. [Crossover from incoherent to coherent phonon scattering in epitaxial oxide superlattices](#). *Nature Materials* **13**, 168 (2014).
- [22] Maria N Luckyanova, Jivtesh Garg, Keivan Esfarjani, Adam Jandl, Mayank T Bulsara, Aaron J Schmidt, Austin J Minnich, Shuo Chen, Mildred S Dresselhaus, Zhifeng Ren, Eugene A. Fitzgerald, and Gang Chen. [Coherent phonon heat conduction in superlattices](#). *Science* **338**, 936 (2012).
- [23] B. Abeles, D. S. Beers, G. D. Cody, and J. P. Dismukes. [Thermal Conductivity of Ge-Si Alloys at High Temperatures](#). *Physical Review* **125**, 44 (1962).
- [24] B. Abeles. [Lattice Thermal Conductivity of Disordered Semiconductor Alloys at High Temperatures](#). *Physical Review* **131**, 1906 (1963).

- [25] Moinuddin K Qureshi, Vijayalakshmi Srinivasan, and Jude A Rivers. [Scalable high performance main memory system using phase-change memory technology](#). *ACM SIGARCH Computer Architecture News* **37**, 24 (2009).
- [26] Moinuddin K Qureshi, Sudhanva Gurumurthi, and Bipin Rajendran. [Phase change memory: From devices to systems](#). *Synthesis Lectures on Computer Architecture* **6**, 1 (2011).
- [27] RE Simpson, P Fons, AV Kolobov, T Fukaya, M Krbal, T Yagi, and J Tomimaga. [Interfacial phase-change memory](#). *Nature nanotechnology* **6**, 501 (2011).
- [28] Benjamin S Williams. [Terahertz quantum-cascade lasers](#). *Nature photonics* **1**, 517 (2007).
- [29] Gaetano Scamarcio, Miriam S Vitiello, Vincenzo Spagnolo, Sushil Kumar, Benjamin Williams, and Qing Hu. [Nanoscale heat transfer in quantum cascade lasers](#). *Physica E: Low-dimensional Systems and Nanostructures* **40**, 1780 (2008).
- [30] H Li, JC Cao, YJ Han, ZY Tan, and XG Guo. [Temperature profile modelling and experimental investigation of thermal resistance of terahertz quantum-cascade lasers](#). *Journal of Physics D: Applied Physics* **42**, 205102 (2009).
- [31] N. Mingo. [Calculation of Si nanowire thermal conductivity using complete phonon dispersion relations](#). *Physical Review B* **68**, 113308 (2003).
- [32] Brian M. Foley, Harlan J. Brown-Shaklee, John C. Duda, Ramez Cheaito, Brady J. Gibbons, Doug Medlin, Jon F. Ihlefeld, and Patrick E. Hopkins. [Thermal conductivity of nano-grained SrTiO₃ thin films](#). *Applied Physics Letters* **101**, 231908 (2012).
- [33] C. Kittel. *Introduction to Solid State Physics*. 8th edition. John Wiley and Sons Inc, 2004.
- [34] MV Simkin and GD Mahan. [Minimum thermal conductivity of superlattices](#). *Physical Review Letters* **84**, 927 (2000).

-
- [35] Gang Chen. *Nanoscale energy transport and conversion: a parallel treatment of electrons, molecules, phonons, and photons*. Oxford University Press, USA, 2005.
- [36] Rama Venkatasubramanian. [Lattice thermal conductivity reduction and phonon localizationlike behavior in superlattice structures](#). *Physical Review B* **61**, 3091 (2000).
- [37] Brian C. Daly, Humphrey J. Maris, K. Imamura, and S. Tamura. [Molecular dynamics calculation of the thermal conductivity of superlattices](#). *Physical Review B* **66**, 024301 (2002).
- [38] K Imamura, Y Tanaka, N Nishiguchi, S Tamura, and HJ Maris. [Lattice thermal conductivity in superlattices: molecular dynamics calculations with a heat reservoir method](#). *Journal of Physics: Condensed Matter* **15**, 8679 (2003).
- [39] Yunfei Chen, Deyu Li, Jennifer R. Lukes, Zhonghua Ni, and Minhua Chen. [Minimum superlattice thermal conductivity from molecular dynamics](#). *Physical Review B* **72**, 174302 (2005).
- [40] Keng-Hua Lin and Alejandro Strachan. [Thermal transport in SiGe superlattice thin films and nanowires: Effects of specimen and periodic lengths](#). *Physical Review B* **87**, 115302 (2013).
- [41] Jivtesh Garg and Gang Chen. [Minimum thermal conductivity in superlattices: A first-principles formalism](#). *Physical Review B* **87**, 140302 (2013).
- [42] B. Latour, S. Volz, and Y. Chalopin. [Microscopic description of thermal-phonon coherence: From coherent transport to diffuse interface scattering in superlattices](#). *Physical Review B* **90**, 014307 (2014).
- [43] Xin Mu, Teng Zhang, David B. Go, and Tengfei Luo. [Coherent and incoherent phonon thermal transport in isotopically modified graphene superlattices](#). *Carbon* **83**, 208 (2015).

- [44] Gang Chen. [Size and interface effects on thermal conductivity of superlattices and periodic thin-film structures](#). *Journal of Heat Transfer* **119**, 220 (1997).
- [45] C.L. Mehta. [Coherence-time and effective bandwidth of blackbody radiation](#). *Il Nuovo Cimento (1955-1965)* **28**, 401 (1963).
- [46] C. Y. Ho, R. W. Powell, and P. E. Liley. [Thermal Conductivity of the Elements](#). *Journal of Physical and Chemical Reference Data* **1**, 279 (1972).
- [47] R. O. Carlson, G. A. Slack, and S. J. Silverman. [Thermal Conductivity of GaAs and GaAs_{1-x}P_x Laser Semiconductors](#). *Journal of Applied Physics* **36**, 505 (1965).
- [48] Choongho Yu, Matthew L. Scullin, Mark Huijben, Ramamoorthy Ramesh, and Arun Majumdar. [Thermal conductivity reduction in oxygen-deficient strontium titanates](#). *Applied Physics Letters* **92**, 191911 (2008).
- [49] Joseph Callaway. [Model for lattice thermal conductivity at low temperatures](#). *Physical Review* **113**, 1046 (1959).
- [50] M. Asen-Palmer, K. Bartkowski, E. Gmelin, M. Cardona, A. P. Zhernov, A. V. Inyushkin, A. Taldenkov, V. I. Ozhogin, K. M. Itoh, and E. E. Haller. [Thermal conductivity of germanium crystals with different isotopic compositions](#). *Physical Review B* **56**, 9431 (1997).
- [51] Lanhua Wei, P. K. Kuo, R. L. Thomas, T. R. Anthony, and W. F. Banholzer. [Thermal conductivity of isotopically modified single crystal diamond](#). *Physical Review Letters* **70**, 3764 (1993).
- [52] Zhao Wang and Natalio Mingo. [Diameter dependence of SiGe nanowire thermal conductivity](#). *Applied Physics Letters* **97**, 101903 (2010).
- [53] PG Klemens. [The scattering of low-frequency lattice waves by static imperfections](#). *Proceedings of the Physical Society. Section A* **68**, 1113 (1955).
- [54] J. M. Ziman. *Electrons and Phonons: The Theory of Transport Phenomena in Solids*. Oxford University Press, 2001.

-
- [55] Pamela M Norris, Nam Q Le, and Christopher H Baker. [Tuning phonon transport: from interfaces to nanostructures](#). *Journal of Heat Transfer* **135**, 061604 (2013).
- [56] P. E. Hopkins. [Thermal Transport across Solid Interfaces with Nanoscale Imperfections: Effects of Roughness, Disorder, Dislocations, and Bonding on Thermal Boundary Conductance](#). *ISRN Mechanical Engineering* **2013**, Article ID 682586 (2013).
- [57] Ramez Cheaito, John T. Gaskins, Matthew E. Caplan, Brian F. Donovan, Brian M. Foley, Ashutosh Giri, John C. Duda, Chester J. Szwejkowski, Costel Constantin, Harlan J. Brown-Shaklee, Jon F. Ihlefeld, and Patrick E. Hopkins. [Thermal boundary conductance accumulation and interfacial phonon transmission: Measurements and theory](#). *Physical Review B* **91**, 035432 (2015).
- [58] J. C. Duda, C.-Y. P. Yang, B. M. Foley, R. Cheaito, D. L. Medlin, R. E. Jones, and P. E. Hopkins. [Influence of interfacial properties on thermal transport at gold:silicon contacts](#). *Applied Physics Letters* **102**, 081902 (2013).
- [59] Brian F. Donovan, Chester J. Szwejkowski, John C. Duda, Ramez Cheaito, John T. Gaskins, C.-Y. Peter Yang, Costel Constantin, Reese E. Jones, and Patrick E. Hopkins. [Thermal boundary conductance across metal-gallium nitride interfaces from 80 to 450K](#). *Applied Physics Letters* **105**, 203502 (2014).
- [60] Carolyn A Paddock and Gary L Eesley. [Transient thermorefectance from thin metal films](#). *Journal of Applied Physics* **60**, 285 (1986).
- [61] Carolyn A Paddock and Gary L Eesley. [Transient thermorefectance from metal films](#). *Optics Letters* **11**, 273 (1986).
- [62] Aaron J. Schmidt, Ramez Cheaito, and Matteo Chiesa. [A frequency-domain thermorefectance method for the characterization of thermal properties](#). *Review of Scientific Instruments* **80**, 094901 (2009).

- [63] Aaron J. Schmidt, Ramez Cheaito, and Matteo Chiesa. [Characterization of thin metal films via frequency-domain thermoreflectance](#). *Journal of Applied Physics* **107**, 24908 (2010).
- [64] Jonathan A Malen, Kanhayalal Baheti, Tao Tong, Yang Zhao, Janice A Hudgings, and Arun Majumdar. [Optical measurement of thermal conductivity using fiber aligned frequency domain thermoreflectance](#). *Journal of Heat Transfer* **133**, 081601 (2011).
- [65] Jon Opsal, Allan Rosencwaig, and David L. Willenborg. [Thermal-wave detection and thin-film thickness measurements with laser beam deflection](#). *Applied Optics* **22**, 3169 (1983).
- [66] William S Capinski and Humphrey J Maris. [Thermal conductivity of GaAs/AlAs superlattices](#). *Physica B: Condensed Matter* **219**, 699 (1996).
- [67] Pamela M. Norris, Andrew P. Caffrey, Robert J. Stevens, J. Michael Klopff, James T. McLeskey, and Andrew N. Smith. [Femtosecond pumpprobe nondestructive examination of materials \(invited\)](#). *Review of Scientific Instruments* **74**, 400 (2003).
- [68] David G. Cahill. [Analysis of heat flow in layered structures for time-domain thermoreflectance](#). *Review of Scientific Instruments* **75**, 5119 (2004).
- [69] Kwangu Kang, Yee Kan Koh, Catalin Chiritescu, Xuan Zheng, and David G. Cahill. [Two-tint pump-probe measurements using a femtosecond laser oscillator and sharp-edged optical filters](#). *Review of Scientific Instruments* **79**, 114901 (2008).
- [70] Aaron J Schmidt, Xiaoyuan Chen, and Gang Chen. [Pulse accumulation, radial heat conduction, and anisotropic thermal conductivity in pump-probe transient thermoreflectance](#). *Review of Scientific Instruments* **79**, 114902 (2008).

- [71] Yuxin Wang, Ji Yong Park, Yee Kan Koh, and David G. Cahill. [Thermoreflectance of metal transducers for time-domain thermoreflectance](#). *Journal of Applied Physics* **108**, 043507 (2010).
- [72] M Ghotbi, M Ebrahim-Zadeh, A Majchrowski, E Michalski, and IV Kityk. [High-average-power femtosecond pulse generation in the blue using BiB₃O₆](#). *Optics Letters* **29**, 2530 (2004).
- [73] Ramez Cheaito, Caroline S. Gorham, Amit Misra, Khalid Hattar, and Patrick E. Hopkins. [Thermal conductivity measurements via time-domain thermoreflectance for the characterization of radiation induced damage](#). *Journal of Materials Research* **30**, 1403 (2015).
- [74] G. L. Eesley. [Generation of nonequilibrium electron and lattice temperatures in copper by picosecond laser pulses](#). *Physical Review B* **33**, 2144 (1986).
- [75] H. E. Elsayed-Ali, T. B. Norris, M. A. Pessot, and G. A. Mourou. [Time-resolved observation of electron-phonon relaxation in copper](#). *Physical Review Letters* **58**, 1212 (1987).
- [76] Ashutosh Giri, John T. Gaskins, Brian M. Foley, Ramez Cheaito, and Patrick E. Hopkins. [Experimental evidence of excited electron number density and temperature effects on electron-phonon coupling in gold films](#). *Journal of Applied Physics* **117**, 044305 (2015).
- [77] G. Tas, J. J. Loomis, H. J. Maris, A. A. Bailes, and L. E. Seiberling. [Picosecond ultrasonics study of the modification of interfacial bonding by ion implantation](#). *Applied Physics Letters* **72**, 2235 (1998).
- [78] Mark D Losego, Martha E Grady, Nancy R Sottos, David G Cahill, and Paul V Braun. [Effects of chemical bonding on heat transport across interfaces](#). *Nature Materials* **11**, 502 (2012).
- [79] Caroline S. Gorham, Khalid Hattar, Ramez Cheaito, John C. Duda, John T. Gaskins, Thomas E. Beechem, Jon F. Ihlefeld, Laura B. Biedermann, Edward

- S. Piekos, Douglas L. Medlin, and Patrick E. Hopkins. [Ion irradiation of the native oxide/silicon surface increases the thermal boundary conductance across aluminum/silicon interfaces](#). *Physical Review B* **90**, 024301 (2014).
- [80] H.T. Grahn, Humphrey J. Maris, and J. Tauc. [Picosecond ultrasonics](#). *Quantum Electronics, IEEE Journal of* **25**, 2562 (1989).
- [81] T. C. Zhu, H. J. Maris, and J. Tauc. [Attenuation of longitudinal-acoustic phonons in amorphous SiO₂ at frequencies up to 440 GHz](#). *Physical Review B* **44**, 4281 (1991).
- [82] C.J. Morath, G. Tas, T.C.-D. Zhu, and H.J. Maris. [Phonon attenuation in glasses studied by picosecond ultrasonics](#). *Physica B: Condensed Matter* **219**, 296 (1996).
- [83] B. C. Daly, K. Kang, Y. Wang, and David G. Cahill. [Picosecond ultrasonic measurements of attenuation of longitudinal acoustic phonons in silicon](#). *Physical Review B* **80**, 174112 (2009).
- [84] Scott Huxtable, David G Cahill, Vincent Fauconnier, Jeffrey O White, and Ji-Cheng Zhao. [Thermal conductivity imaging at micrometre-scale resolution for combinatorial studies of materials](#). *Nature Materials* **3**, 298 (2004).
- [85] Xuan Zheng, David G Cahill, and J-C Zhao. [Thermal conductivity imaging of thermal barrier coatings](#). *Advanced Engineering Materials* **7**, 622 (2005).
- [86] Horatio Scott Carslaw and John Conrad Jaeger. *Conduction of heat in solids*. Vol. 2. Clarendon Press Oxford, 1959.
- [87] W. S. Capinski, H. J. Maris, T. Ruf, M. Cardona, K. Ploog, and D. S. Katzer. [Thermal-conductivity measurements of GaAs/AlAs superlattices using a picosecond optical pump-and-probe technique](#). *Physical Review B* **59**, 8105 (1999).
- [88] Ruye Wang. *Introduction to orthogonal transforms: with applications in data processing and analysis*. Cambridge University Press, 2012, p. 8.

- [89] Ruxandra M. Costescu, Marcel A. Wall, and David G. Cahill. [Thermal conductance of epitaxial interfaces](#). *Physical Review B* **67**, 054302 (2003).
- [90] Robert G. Morris and Jerome G. Hust. [Thermal Conductivity Measurements of Silicon from 30° to 425 °C](#). *Physical Review* **124**, 1426 (1961).
- [91] Robert C Weast, Melvin J Astle, and William H Beyer. *CRC handbook of chemistry and physics*. Vol. 69. CRC press Boca Raton, FL, 1988.
- [92] David G. Cahill, S.-M. Lee, and Torbjørn I. Selinder. [Thermal conductivity of \$\kappa\$ -Al₂O₃ and \$\alpha\$ -Al₂O₃ wear-resistant coatings](#). *Journal of Applied Physics* **83**, 5783 (1998).
- [93] John H. Lienhard IV and John H. Lienhard V. *A Heat Transfer Textbook*. 4th edition. Courier Dover Publications, 2012.
- [94] F. Incropera and D. P. DeWitt. *Fundamentals of Heat and Mass Transfer*. 4th edition. New York: Wiley and Sons, Inc., 1996.
- [95] G. Jeffrey Snyder and Eric S. Toberer. [Complex thermoelectric materials](#). *Nature Materials* **7**, 105 (2008).
- [96] S.-M. Lee, David G. Cahill, and Rama Venkatasubramanian. [Thermal conductivity of SiGe superlattices](#). *Applied Physics Letters* **70**, 2957 (1997).
- [97] R Venkatasubramanian, E Siivola, and TS Colpitts. [In-plane thermoelectric properties of freestanding Si/Ge superlattice structures](#). *International Conference on Thermoelectrics, 1998. Proceedings ICT 98. XVII*, 191 (1998).
- [98] T. Borca-Tasciuc, Weili Liu, Jianlin Liu, Taofang Zeng, D.W. Song, C.D. Moore, Gang Chen, K.L. Wang, M.S. Goorsky, T. Radetic, R. Gronsky, Xi-angzhong Sun, and Mildred S. Dresselhaus. [Thermal conductivity of Si/Ge superlattices](#). *Proceedings of the Eighteenth International Conference on Thermoelectrics*, 201 (1999).
- [99] Theodorian Borca-Tasciuc, Weili Liu, Jianlin Liu, Taofang Zeng, David W. Song, Caroline D. Moore, Gang Chen, Kang L. Wang, Mark S. Goorsky,

- Tamara Radetic, Ronald Gronsky, Takaaki Koga, and Mildred S. Dresselhaus. [Thermal conductivity of symmetrically strained Si/Ge superlattices](#). *Superlattices and Microstructures* **28**, 199 (2000).
- [100] S. Chakraborty, C. A. Kleint, A. Heinrich, C. M. Schneider, J. Schumann, M. Falke, and S. Teichert. [Thermal conductivity in strain symmetrized Si/Ge superlattices on Si\(111\)](#). *Applied Physics Letters* **83**, 4184 (2003).
- [101] Scott T. Huxtable, Alexis R. Abramson, Chang-Lin Tien, Arun Majumdar, Chris LaBounty, Xiaofeng Fan, Gehong Zeng, John E. Bowers, Ali Shakouri, and Edward T. Croke. [Thermal conductivity of Si/SiGe and SiGe/SiGe superlattices](#). *Applied Physics Letters* **80**, 1737 (2002).
- [102] G. Chen, S.Q. Zhou, D.-Y. Yao, C.J. Kim, X.Y. Zheng, Z.L. Liu, and K.L. Wang. [Heat conduction in alloy-based superlattices](#). *Proceedings of the Seventeenth International Conference on Thermoelectrics (IEEE, New York)*, 202 (1998).
- [103] Deyu Li, Yiying Wu, Rong Fan, Peidong Yang, and Arun Majumdar. [Thermal conductivity of Si/SiGe superlattice nanowires](#). *Applied Physics Letters* **83**, 3186 (2003).
- [104] Cronin B. Vining. [A model for the high-temperature transport properties of heavily doped n-type silicon-germanium alloys](#). *Journal of Applied Physics* **69**, 331 (1991).
- [105] Giri Joshi, Hohyun Lee, Yucheng Lan, Xiaowei Wang, Gaohua Zhu, Dezhi Wang, Ryan W. Gould, Diana C. Cuff, Ming Y. Tang, Mildred S. Dresselhaus, Gang Chen, and Zhifeng Ren. [Enhanced Thermoelectric Figure-of-Merit in Nanostructured p-type Silicon Germanium Bulk Alloys](#). *Nano Letters* **8**, 4670 (2008).
- [106] X. W. Wang, H. Lee, Y. C. Lan, G. H. Zhu, G. Joshi, D. Z. Wang, J. Yang, A. J. Muto, M. Y. Tang, J. Klatsky, S. Song, M. S. Dresselhaus, G. Chen, and

- Z. F. Ren. [Enhanced thermoelectric figure of merit in nanostructured n-type silicon germanium bulk alloy](#). *Applied Physics Letters* **93**, 193121 (2008).
- [107] Glen A. Slack and Moayyed A. Hussain. [The maximum possible conversion efficiency of silicon-germanium thermoelectric generators](#). *Journal of Applied Physics* **70**, 2694 (1991).
- [108] G. Chen and M. Neagu. [Thermal conductivity and heat transfer in superlattices](#). *Applied Physics Letters* **71**, 2761 (1997).
- [109] A. A. Kiselev, K. W. Kim, and M. A. Stroscio. [Thermal conductivity of Si/Ge superlattices: A realistic model with a diatomic unit cell](#). *Physical Review B* **62**, 6896 (2000).
- [110] S. Volz, J. B. Saulnier, G. Chen, and P. Beauchamp. [Computation of thermal conductivity of Si/Ge superlattices by molecular dynamics techniques](#). *Microelectronics Journal* **31**, 815 (2000).
- [111] E. S. Landry and A. J. H. McGaughey. [Effect of interfacial species mixing on phonon transport in semiconductor superlattices](#). *Physical Review B* **79**, 075316 (2009).
- [112] D. P. Sellan, E. S. Landry, J. E. Turney, A. J. H. McGaughey, and C. H. Amon. [Size effects in molecular dynamics thermal conductivity predictions](#). *Physical Review B* **81**, 214305 (2010).
- [113] Jie Chen, Gang Zhang, and Baowen Li. [Tunable thermal conductivity of \$\text{Si}_{1-x}\text{Ge}_x\$ nanowires](#). *Applied Physics Letters* **95**, 073117 (2009).
- [114] Ashton Skye and Patrick K. Schelling. [Thermal resistivity of SiGe alloys by molecular-dynamics simulation](#). *Journal of Applied Physics* **103**, 113524 (2008).
- [115] Jivtesh Garg, Nicola Bonini, Boris Kozinsky, and Nicola Marzari. [Role of Disorder and Anharmonicity in the Thermal Conductivity of Silicon-Germanium Alloys: A First-Principles Study](#). *Physical Review Letters* **106**, 045901 (2011).

- [116] D. G. Cahill, A. Bullen, and S.-M. Lee. [Interface thermal conductance and the thermal conductivity of multilayer thin films.](#) *High Temperatures-High Pressures* **32**, 135 (2000).
- [117] Yee Kan Koh and David G. Cahill. [Frequency dependence of the thermal conductivity of semiconductor alloys.](#) *Physical Review B* **76**, 075207 (2007).
- [118] H.-Matsuo Kagaya, Y. Kitani, and T. Soma. [Theoretical study of thermal properties for Si-Ge system.](#) *Solid State Communications* **58**, 399 (1986).
- [119] David G. Cahill, Fumiya Watanabe, Angus Rockett, and Cronin B. Vining. [Thermal conductivity of epitaxial layers of dilute SiGe alloys.](#) *Physical Review B* **71**, 235202 (2005).
- [120] Peixuan Chen, NA Katcho, JP Feser, Wu Li, M Glaser, OG Schmidt, David G Cahill, N Mingo, and A Rastelli. [Role of surface-segregation-driven intermixing on the thermal transport through planar Si/Ge superlattices.](#) *Physical Review Letters* **111**, 115901 (2013).
- [121] W Schnelle, R Fischer, and E Gmelin. [Specific heat capacity and thermal conductivity of NdGaO₃ and LaAlO₃ single crystals at low temperatures.](#) *Journal of Physics D: Applied Physics* **34**, 846 (2001).
- [122] Brian F Woodfield, Jennifer L Shapiro, Rebecca Stevens, Juliana Boerio-Goates, Robert L Putnam, Katheryn B Helean, and Alexandra Navrotsky. [Molar heat capacity and thermodynamic functions for CaTiO₃.](#) *The Journal of Chemical Thermodynamics* **31**, 1573 (1999).
- [123] SS Todd and RE Lorensen. [Heat capacities at low temperatures and entropies at 298.16 K. of metatitanates of barium and strontium.](#) *Journal of the American Chemical Society* **74**, 2043 (1952).
- [124] Taishan Zhu and Elif Ertekin. [Phonon transport on two-dimensional graphene/boron nitride superlattices.](#) *Physical Review B* **90**, 195209 (2014).

-
- [125] X. Y. Yu, G. Chen, A. Verma, and J. S. Smith. [Temperature dependence of thermophysical properties of GaAs/AlAs periodic structure](#). *Applied Physics Letters* **67**, 3554 (1995).
- [126] Takafumi Yao. [Thermal properties of AlAs/GaAs superlattices](#). *Applied Physics Letters* **51**, 1798 (1987).
- [127] Samuel C Huberman, Jason M Larkin, Alan JH McGaughey, and Cristina H Amon. [Disruption of superlattice phonons by interfacial mixing](#). *Physical Review B* **88**, 155311 (2013).
- [128] Yee Kan Koh, Yu Cao, David G. Cahill, and Debdeep Jena. [Heat-Transport Mechanisms in Superlattices](#). *Advanced Functional Materials* **19**, 610 (2009).
- [129] Fan Yang and Chris Dames. [Mean free path spectra as a tool to understand thermal conductivity in bulk and nanostructures](#). *Physical Review B* **87**, 035437 (2013).
- [130] Mikhail Zhernenkov, Simerjeet Gill, Vesna Stanic, Elaine DiMasi, Kim Kisslinger, J. Kevin Baldwin, Amit Misra, M. J. Demkowicz, and Lynne Ecker. [Design of radiation resistant metallic multilayers for advanced nuclear systems](#). *Applied Physics Letters* **104**, 241906 (2014).
- [131] X. Zhang, E. G. Fu, Nan Li, A. Misra, Y.-Q. Wang, L. Shao, and H. Wang. [Design of Radiation Tolerant Nanostructured Metallic Multilayers](#). *Journal of Engineering Materials and Technology* **134**, 041010 (2012).
- [132] Jing Shi, Kevin Pettit, E. Kita, S. S. P. Parkin, R. Nakatani, and M. B. Salamon. [Field-dependent thermoelectric power and thermal conductivity in multilayered and granular giant magnetoresistive systems](#). *Physical Review B* **54**, 15273 (1996).
- [133] Y. Yang, J.-G. Zhu, R. M. White, and M. Asheghi. [Field-dependent thermal and electrical transports in Cu/CoFe multilayer](#). *Journal of Applied Physics* **99**, 063703 (2006).

- [134] W.P. Pratt and J. Bass. [Perpendicular-current studies of electron transport across metal/metal interfaces](#). *Applied Surface Science* **256**, 399 (2009).
- [135] W.-H. Soe, T. Kaizuka, R. Yamamoto, and T. Matsushashi. [Measurements of transport properties of Ag/Al and Ag/Cu multilayered films](#). *Journal of Magnetism and Magnetic Materials* **126**, 457 (1993).
- [136] R. B. Wilson and David G. Cahill. [Experimental Validation of the Interfacial Form of the Wiedemann-Franz Law](#). *Physical Review Letters* **108**, 255901 (2012).
- [137] A. Majumdar and P. Reddy. [Role of electron-phonon coupling in thermal conductance of metal/nonmetal interfaces](#). *Applied Physics Letters* **84**, 4768 (2004).
- [138] A. V. Sergeev. [Electronic Kapitza conductance due to inelastic electron-boundary scattering](#). *Physical Review B* **58**, R10199 (1998).
- [139] Patrick E. Hopkins, Jared L. Kassebaum, and Pamela M. Norris. [Effects of electron scattering at metal-nonmetal interfaces on electron-phonon equilibration in gold films](#). *Journal of Applied Physics* **105**, 023710 (2009).
- [140] Bryan C. Gundrum, David G. Cahill, and Robert S. Averback. [Thermal conductance of metal-metal interfaces](#). *Physical Review B* **72**, 245426 (2005).
- [141] Patrick E. Hopkins, Thomas E. Beechem, John C. Duda, Justin L. Smoyer, and Pamela M. Norris. [Effects of subconduction band excitations on thermal conductance at metal-metal interfaces](#). *Applied Physics Letters* **96**, 011907 (2010).
- [142] Bruce M. Clemens, Gary L. Eesley, and Carolyn A. Paddock. [Time-resolved thermal transport in compositionally modulated metal films](#). *Physical Review B* **37**, 1085 (1988).

-
- [143] R M Costescu, D G Cahill, F H Fabreguette, Z A Sechrist, and S M George. [Ultra-low thermal conductivity in W/Al₂O₃ nanolaminates.](#) *Science* **303**, 989 (2004).
- [144] M. Hamalainen, K. Jaaskelainen, R. Luoma, M. Nuotio, P. Taskinen, and O. Teppo. [A thermodynamic analysis of the binary alloy systems Cu-Cr, Cu-Nb and Cu-V.](#) *Calphad* **14**, 125 (1990).
- [145] H. R. Gong and B. X. Liu. [Unusual alloying behavior at the equilibrium immiscible Cu-Nb interfaces.](#) *Journal of Applied Physics* **96**, 3020 (2004).
- [146] A. Misra, R.G. Hoagland, and H. Kung. [Thermal stability of self-supported nanolayered Cu/Nb films.](#) *Philosophical Magazine* **84**, 1021 (2004).
- [147] Ramez Cheaito, Khalid Hattar, John T. Gaskins, Ajay K. Yadav, John C. Duda, Thomas E. Beechem, Jon F. Ihlefeld, Edward S. Piekos, Jon K. Baldwin, Amit Misra, and Patrick E. Hopkins. [Thermal flux limited electron Kapitza conductance in copper-niobium multilayers.](#) *Applied Physics Letters* **106**, 093114 (2015).
- [148] E. Swartz and R. Pohl. [Thermal boundary resistance.](#) *Reviews of Modern Physics* **61**, 605 (1989).
- [149] Fritsche L. Eckardt H. and J. Noffke. [Self-consistent relativistic band structure of the noble metals.](#) *Journal of Physics F: Metal Physics* **14**, 97 (1984).
- [150] A. R. Jani, N. E. Brener, and J. Callaway. [Band structure and related properties of bcc niobium.](#) *Physical Review B* **38**, 9425 (1988).
- [151] L. F. Mattheiss. [Electronic Structure of Niobium and Tantalum.](#) *Physical Review B* **1**, 373 (1970).
- [152] J. Noffke and L. Fritsche. [Band structure calculation and photoemission analysis of iridium.](#) *Journal of Physics F: Metal Physics* **12**, 921 (1982).
- [153] F. M. Mueller, A. J. Freeman, J. O. Dimmock, and A. M. Furdyna. [Electronic Structure of Palladium.](#) *Physical Review B* **1**, 4617 (1970).

- [154] Zhibin Lin, Leonid V. Zhigilei, and Vittorio Celli. [Electron-phonon coupling and electron heat capacity of metals under conditions of strong electron-phonon nonequilibrium](#). *Physical Review B* **77**, 075133 (2008).
- [155] O. Krogh Andersen. [Electronic Structure of the fcc Transition Metals Ir, Rh, Pt, and Pd](#). *Physical Review B* **2**, 883 (1970).
- [156] A. Belmiloudi. *Heat Transfer - Mathematical Modelling, Numerical Methods and Information Technology*. InTech, 2011.
- [157] R. B. Wilson, Brent A. Apgar, Wen-Pin Hsieh, Lane W. Martin, and David G. Cahill. [Thermal conductance of strongly bonded metal-oxide interfaces](#). *Physical Review B* **91**, 115414 (2015).
- [158] T. Tsuchiya, H. Akera, and T. Ando. [Phonons in GaAs/AlAs superlattices](#). *Physical Review B* **39**, 6025 (1989).
- [159] J. L. T. Waugh and G. Dolling. [Crystal Dynamics of Gallium Arsenide](#). *Physical Review* **132**, 2410 (1963).
- [160] Sadao Adachi. *Properties of aluminium gallium arsenide*. The Institution of Engineering and Technology, 1993.
- [161] M.S. Abrahams, R. Braunstein, and F.D. Rosi. [Thermal, electrical and optical properties of \(In,Ga\)As alloys](#). *Journal of Physics and Chemistry of Solids* **10**, 204 (1959).
- [162] Wu Li, Jess Carrete, Nebil A. Katcho, and Natalio Mingo. [ShengBTE: A solver of the Boltzmann transport equation for phonons](#). *Computer Physics Communications* **185**, 1747 (2014).
- [163] A. Ward, D. A. Broido, Derek A. Stewart, and G. Deinzer. [Ab initio theory of the lattice thermal conductivity in diamond](#). *Physical Review B* **80**, 125203 (2009).

- [164] A. Ward and D. A. Broido. [Intrinsic phonon relaxation times from first-principles studies of the thermal conductivities of Si and Ge.](#) *Physical Review B* **81**, 085205 (2010).
- [165] M Omini and A Sparavigna. [An iterative approach to the phonon Boltzmann equation in the theory of thermal conductivity.](#) *Physica B: Condensed Matter* **212**, 101 (1995).
- [166] M. Omini and A. Sparavigna. [Beyond the isotropic-model approximation in the theory of thermal conductivity.](#) *Physical Review B* **53**, 9064 (1996).